Investigating the Kinematics and Dynamics of Strain Localization in the Northern Western Branch of the East African Rift System

Asenath Kwagalakwe

Dissertation submitted to the faculty of the Virginia Polytechnic Institute and State University in partial fulfillment of the requirements for the degree of

Doctor of Philosophy
in
Geosciences

D. Sarah Stamps, Chair
Manoochehr Shirzaei
Ying Zhou
Estella Atekwana
Emmanuel Njinju

May 2, 2025
Blacksburg, Virginia

Keywords: Magma-poor continental rifting, GNSS geodesy, Kinematic modeling, Geodynamic modeling

Investigating the Kinematics and Dynamics of Strain Localization in the Northern Western Branch of the East African Rift System

Asenath Kwagalakwe

ABSTRACT

Continental rifts are thought to be formed by repeated episodes of magmatism, reactivation of pre-existing structures, or a combination of both. Continental rifts are evidence of a divergent plate boundary, where tectonic plates are breaking apart. The northern Western Branch of the East African Rift System (EARS) is an active continental rift that forms part of the divergent plate boundary between the Nubian plate and Victoria microplate, comprising magma-rich Lakes George-Edward graben in southwestern Uganda and the magma-poor Albertine and Rhino grabens in northwestern Uganda. The physics of strain localization in the northern Western Branch is not well understood. This PhD study investigated the kinematics and dynamics of strain localization in the northern Western Branch through two projects: 1) investigating the contribution of deep melt to rifting generated from two small-scale convection mechanisms beneath the northern Western Branch using the finite element software Advanced Solver for Planetary Evolution, Convection, and Tectonics (ASPECT); and 2) calculating the present-day Victoria microplate motion, strain rates, and geodetic fault slip rates to assess deformation zones using Global Navigation Satellite System (GNSS) data from within the Victoria microplate and geodetic inversion modeling with TDEFNODE software. Modeling results from project 1 indicate that rifting in the northern Western Branch is likely influenced by deep melt that migrates northward from the Kivu Rift and deep melt that migrates westward along the Aswa shear zone from the Kenyan Rift. Regarding project 2, we find that the Victoria microplate is rotating counterclockwise at 0.0623±0.0293 deg/My, consistent with previous studies, but with the Euler pole ~376 km northwest of earlier work. Calculated strain rates along the Victoria microplate boundaries range from 7.6×10^{-8} to 1.36×10^{-7} y^{-1}, while calculated fault slip rates along the eastern NWB faults range between 1.93 and 2.34 mm/y. Consistent with geologic observations of slip directions, our kinematic model indicates that Victoria Plate rotation is accommodated, in part, by oblique-slip on northern Western Branch border faults.

Investigating the Kinematics and Dynamics of Strain Localization in the Northern Western Branch of the East African Rift System

Asenath Kwagalakwe

GENERAL AUDIENCE ABSTRACT

Some areas of the Earth's outer shell can become significantly thin leading to rupture known as a continental rift. The Earth's outer shell, called the lithosphere, is made up of numerous tectonic plates, microplates, or blocks that are in constant motion. A continental rift is visible evidence of two tectonic plates breaking away from each other, what is called divergent plate boundary. Continental rifts may arise from repeated periods of hot molten rock intrusions (magmatism) sourced from kilometers below the Earth's surface, or from the reactivation of ancient geological structures like faults, folds, and joints, collectively referred to as pre-existing structures. Alternatively, continental rifts may evolve due to a combination of magmatism and reactivation of pre-existing structures. This study investigates the role of deeply sourced magmatism along the northern Western Branch of the East African Rift System, a continental rift in East Africa. In addition, this work also investigates how the Victoria microplate moves relative to the Nubian plate and their interactions along the northern Western Branch plate boundary. This PhD dissertation comprises two distinct projects: 1) investigating the presence of magmatism at depths of 90-660 km beneath the northern Western Branch by solving mathematical equations that describe the physical conditions (numerical models) under two initial temperature conditions; and 2) calculating the present-day motion of the Victoria microplate relative to the Nubian plate and their interactions along the northern Western Branch plate boundary. This PhD research suggests that rifting in the northern Western Branch is likely influenced by deeply sourced magmatism that is transported from distant regions. We find that the Victoria microplate is rotating counterclockwise at 0.0623 ± 0.0293 deg/My, consistent with previous studies, but with the Euler pole ~376 km northwest of earlier work and also provide constraints on strain rates and fault slip rates. Our kinematic model indicates that Victoria microplate rotation is accommodated, in part, by oblique-slip on border faults of the northern Western Branch.

Dedication

I dedicate this to my parents, siblings, nieces, and nephews for your constant love and support.

Acknowledgements

This PhD research was funded by US National Science Foundation Frontier Research in Earth Sciences Awards NSF-2021633, 2021356, 2021692, 2021724, and 2021660. The finite element code entitled Advanced Solver for Planetary Evolution, Convection, and Tectonics (ASPECT), and Geodynamic World Builder is hosted by the Computational Infrastructure for Geodynamics (CIG) which is supported by the National Science Foundation awards NSF-0949446, NSF-1550901, and NSF-21491256. GAMIT and GLOBK software is hosted by the Department of Earth, Atmospheric and Planetary Sciences, MIT while TDEFNODE software is hosted by Professor Rob McCaffrey. The figures in this dissertation have been generated with the Generic Mapping Tools V6.5.0 (Wessel et al., 2019), VisIT software V3.3.3 (Childs et al., 2012), ParaView software V5.12.0 (Henderson, 2007), and Adobe Illustrator V28.4.1 (Adobe Inc., 2024).

Table of contents

Attribution

Chapter one of this dissertation was co-authored by **D. Sarah Stamps** (PhD Advisor) at Department of Geosciences, Virginia Tech, Blacksburg, VA, USA; **Emmanuel A. Njinju** previously at Department of Earth and Planetary Sciences, University of California, Davis, Davis, CA, USA but is currently at Department of Geosciences, Baylor University, Waco, TX, USA; **Tahiry Rajaonarison** at Department of Earth and Environmental Science, New Mexico Tech, Socorro, NM, USA; **Rob L. Evans** at Department of Geology and Geophysics, Woods Hole Oceanographic Institution, Woods Hole, MA, USA; **Estella A. Atekwana** at Department of Earth and Planetary Sciences, University of California, Davis, Davis, CA, USA; **Michael Taylor** at Department of Geology, University of Kansas, Lawrence, KS, USA; **Andrew B. Katumwehe** who was previously at Kimbell School of Geosciences, Midwestern State University, Wichita Falls, TX, USA, but is currently at Boone Pickens School of Geology, Oklahoma State University, Stillwater, OK, USA; **Peter H. Barry** at the Department of Marine Chemistry and Geochemistry, Woods Hole Oceanographic Institution, Woods Hole, MA, USA; **Hillary Mwongyera** at the Department of Geology, University of Kansas, Lawrence, KS, USA; **John Mary Kiberu** at the Department of Geology and Petroleum Studies, Makerere University, Kampala, Uganda; **Fred Tugume** at Directorate of Geological Survey and Mines, Ministry of Energy and Mineral Resources, Kampala, Uganda; **Suzan van der Lee**; and **Albert Kabanda**, both at the Department of Earth and Planetary Sciences, Northwestern University, Evanston, IL, USA; **Joan Nakajigo** at the Department of Geology and Petroleum Studies, Makerere University, Kampala, Uganda, and **Eliot A. Atekwana** at the Department of Earth and Planetary Sciences, University of California, Davis, Davis, CA, USA.

Chapter two of this dissertation was co-authored by **D. Sarah Stamps** (PhD Advisor) at Department of Geosciences, Virginia Tech, Blacksburg, VA, USA; **Folarin Kolawole** at Department of Earth and Environmental Sciences, Columbia University, New York City, NY, USA; **Estella A. Atekwana** at Department of Earth and Planetary Sciences, University of California, Davis, Davis, CA, USA; **Michael Taylor** at Department of Geology, University of Kansas, Lawrence, KS, USA; **Eliot A. Atekwana** at the Department of Earth and Planetary Sciences, University of California, Davis, Davis, CA, USA. **Andrew B. Katumwehe** who was previously at Kimbell School of Geosciences, Midwestern State University, Wichita Falls, TX, USA, but is currently at Boone Pickens School of Geology, Oklahoma State University, Stillwater, OK, USA; **Peter H. Barry** at the Department of Marine Chemistry and Geochemistry, Woods Hole Oceanographic Institution, Woods Hole, MA, USA; **Emmanuel A. Njinju** at Department of Geosciences, Baylor University, Waco, TX, USA; **Fred Tugume** at Directorate of Geological Survey and Mines, Ministry of Energy and Mineral Resources, Kampala, Uganda; **John Mary Kiberu**; and **Joan Nakajigo**, both at the Department of

Geology and Petroleum Studies, Makerere University, Kampala, Uganda; and **Albert Kabanda** at the Department of Earth and Planetary Sciences, Northwestern University, Evanston, IL, USA.

INTRODUCTION

Understanding continental rifts requires a deep understanding of the mechanisms of lithospheric extension. The majority of continental rifts form as a result of the ascent of a heat source from the mantle that causes lithospheric thinning and eventually rifting, for example, the Rio Grande Rift (e.g., Abbey & Niemi, 2020) and the Kenya Rift (e.g., Macdonald, 2002). These continental rifts are commonly known as magma-rich rifts. However, some continental rifts known as magma-poor rifts can form without evidence of magmatism, mainly following pre-existing zones of weakness like mobile belts and avoiding stronger ones like cratons (e.g., Dunbar & Sawyer, 1988; Naliboff et al., 2020).

The northern Western Branch of the East African Rift System (EARS) consists of both the magma-rich Lakes George-Edward graben segment and the magma-poor Albertine and Rhino grabens segments (Fig. 1). The northern Western Branch forms part of the plate boundary between the Nubian plate and the Victoria microplate/block in an extensional setting (Fig. 1).

This PhD research is motivated by the need to advance our scientific knowledge on magma-poor vs. magma-rich continental rifts. This research seeks to answer two main research questions: 1) What are the weakening mechanisms facilitating rifting of the northern Western Branch? and 2) What are the present-day kinematics of the northern Western Branch and the Victoria microplate relative to the fixed Nubian plate? To answer these questions, we carry out two distinct research projects: 1) investigating the presence of deep melt in the northern Western Branch using geodynamic modeling of melt generation from two small-scale convection in the upper mantle (Lithospheric Modulated Convection and Tomography-Based Convection) and 2) constraining the kinematics (motion) of the northern Western Branch and the Victoria microplate relative to the fixed Nubian plate using Global Navigation Satellite System (GNSS) positioning and block inverse modeling. Project one is described in detail in Chapter one, while Project two is in Chapter two of this dissertation.

Through this PhD research, we now have new geodynamic models that advance our understanding of the strain localization in the northern Western Branch. We have also developed a revised kinematic model of the Victoria microplate that is supported by geologic observations of oblique slip in the northern Western Branch.

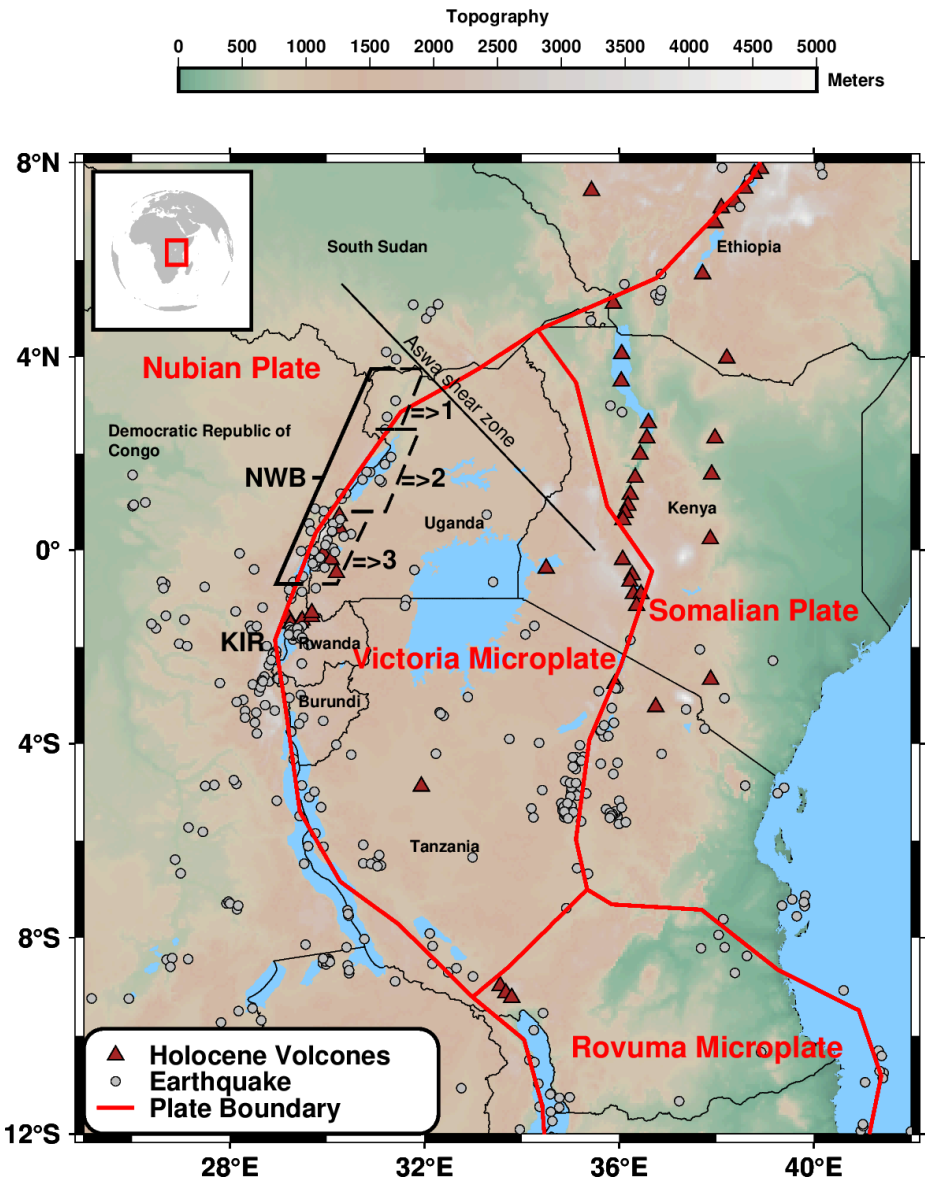

Fig. 1: Map showing our study region, including the Victoria microplate, part of the Rovuma microplate, part of the Somalia plate, and part of the Nubian plate (Saria et al., 2014; Stamps et al., 2021). The plate/microplate boundaries are shown as red lines; Holocene volcanoes in the region are brown triangles (Global Volcanism Program, 2013); and earthquakes from 2014 to 2025 from the National Earthquake Information Center catalog (Masse and Needham, 1989) are plotted as gray circles. The northern Western Branch is denoted by NWB while the Kivu Rift as KIR. The Rhino, Albertine, and Lakes George-Edward Grabens are denoted by 1, 2, and 3, respectively. The inset map shows the relative location of the study region (red color) on Earth.

CHAPTER ONE

Investigating the Presence of Deep Melt in the Northern Western Branch of the East African Rift System

The original version of the work is currently under second review with the Journal of Geophysical Research: Solid Earth as:

Kwagalakwe, A., Stamps, D.S., Njinju, E.A., Evans R.L., Atekwana, E.A., Taylor, M., Katumwehe, A.B., Barry, P.H., Mwongyera, H., Kiberu, J.M., Kabanda, A., Nakajigo, J. (in second review). Investigating Melt Generation Beneath the Northern Western Branch of the East African Rift System Using 3D Geodynamic Modeling with ASPECT, *Journal of Geophysical Research: Solid Earth*

Abstract

Continental rifts often develop through repeated episodes of magmatism that often follow pre-existing structures. The dominant mechanism for strain accommodation in the northern Western Branch of the East African Rift System (EARS), which hosts both magma-rich and magma-poor continental rifting, is not fully understood. Using two types of small-scale convection in the upper mantle, this study investigates the presence of deep melt (i.e., melt between the Lithosphere-Asthenosphere Boundary (LAB) and 660 *km*) beneath the northern Western Branch. The first type, Lithospheric Modulated Convection, produces sublithospheric melt due to mantle convection influenced by variations in the LAB beneath the northern Western Branch. The second type, Tomography-Based Convection, produces sublithospheric melt due to mantle convection constrained by thermal anomalies resulting from plume materials and LAB variations. For both Lithospheric Modulated Convection and Tomography-Based Convection, we calculate melt fractions below the lithosphere using an established melt parameterization scheme. The Lithospheric Modulated Convection models generate melt fractions ranging from 0.007-0.046, while the results from Tomography-Based Convection models range from 0.023-0.409. Our study suggests that deep melt transported from the Kivu rift and north of Aswa shear zone in Kenyan Rift likely contributes to rifting in the northern Western Branch through thermal weakening of the lithosphere.

1. Introduction

Continental rifts represent the initial stages of continental breakup, playing a crucial role in the evolution of the continental lithosphere, the formation of ocean basins, and landscape evolution. Continental rifts can be categorized into two end-member types: magma-poor and magma-rich (e.g., Grant et al., 2024; Koptev et al., 2016). We define a magma-poor continental rift as one formed when extension is characterized by limited or no magmatism and with no volcanoes present. In contrast, we define a magma-rich rift as being formed when the extension

is characterized by a significant amount of magmatism including surface volcanism. Both magma-poor and magma-rich rifting occur in response to lithospheric extension, but the mechanisms facilitating rifting may be different. Strain accommodation in magma-rich rifts is assumed to be associated with magmatic activity during rifting (e.g., Buck, 2006; Corti, 2009; Koptev et al., 2016; Wilson, 1992), while lithospheric stretching in magma-poor rifts occurs without significant decompression melting (e.g., Dunbar & Sawyer, 1988; Naliboff & Buiter, 2015; Njinju et al., 2021; 2023; Tugend et al., 2020).

Lithospheric stretching in continental rift zones occurs as a result of far-field tectonic forces, such as slab pull forces, lithospheric buoyancy forces, and/or mantle tractions at the Lithosphere-Asthenosphere Boundary (LAB; Artyushkov, 1973; Brune et al., 2023; Forsyth *&* Uyeda, 1975; Ghosh *&* Holt, 2012; Schellart, 2004; Rajaonarison et al., 2020; Stamps et al., 2014). During extension, the crust is typically thinned by normal faulting with a lithospheric mantle that is stretched, thinned, and affected by thermal erosion (Buck, 1991; Lavier *&* Manatschal, 2006; Masek et al., 1994; Ring, 2014). The tectonic force required to induce rifting is usually insufficient to overcome the strength of the lithosphere, which is called the "tectonic force paradox" (Buck, 2006), thus lithospheric weakening mechanisms are required. Several studies have found that continental rifts form in regions weakened by heat associated with magmatism (e.g., Buck, 2006; Jones et al., 2019; Muirhead et al., 2016), pre-existing structures (e.g., Dunbar *&* Sawyer, 1988; Katumwehe et al., 2016; Peace et al., 2018; Weinstein et al., 2017), or fluids (e.g., Leseane et al., 2015; Muirhead et al., 2016).

The northern Western Branch of the East African Rift System (EARS), which is the focus of our study, comprises the magma-rich Lakes George-Edward graben in the south and the magma-poor Albertine and Rhino grabens at its northern termination (Figures 1 and 2). The dominant rift initiation paradigm in regions that lack far-field slab-pull forces suggests that magma-assisted rifting is necessary to weaken strong lithospheres, requiring only small tectonic stresses for rupture (Buck, 2004). However, the northern Western Branch consists of both the magma-rich and magma-poor segments, challenging the magma-assisted model. Recent studies of magma-poor segments of the EARS have provided new images of crustal and upper mantle structure beneath magma-poor rifts (e.g., Evans et al., 2019; Hodgson et al., 2017; Leseane et al., 2015; Yu et al., 2017; 2020). For example, the high heat flow beneath the magma-poor incipient Okavango rift zone in Botswana, measured from boreholes (Ballard et al., 1987) and calculated using aeromagnetic data (Leseane et al., 2015), is believed to be due to the upward movement of hot mantle fluids through the lithospheric column, with Precambrian lithospheric shear zones serving as pathways (Leseane et al., 2015). Seismic imaging beneath the magma-poor incipient Okavango rift zone revealed a low velocity anomaly in the upper asthenosphere, suggested to result from decompression melting due to lithospheric thinning (Yu et al., 2017; 2020; Fadel et. al., 2020). A magnetotelluric survey in the Barotse Basin of western Zambia revealed thinned lithosphere beneath an orogenic belt, with the uppermost asthenosphere, at 60-70 km depth, being highly conductive, suggesting partial melt despite no surface volcanism in the region (Evans et al., 2019). In addition, seismic imaging in the magma-poor rifting in the Tanganyika

rift found a thinner crust and low velocity anomaly with higher Vp/Vs ratios at its southern end, interpreted as blind magmatism (magmatism at depth yet to breach the surface; Hodgson et al., 2017; Ajala et al., 2024). Therefore, there is mounting evidence to suggest that magma might be present at depth but yet to breach the surface beneath some magma-poor rifts (blind magmatism). The northern Western Branch comprises both magma-poor and magma-rich segments and therefore provides an ideal location for addressing long standing questions related to lithospheric weakening mechanisms facilitating rifting. In this study, we investigate the presence of deep melt generated from small-scale convection, which may contribute to rifting processes in the northern Western Branch.

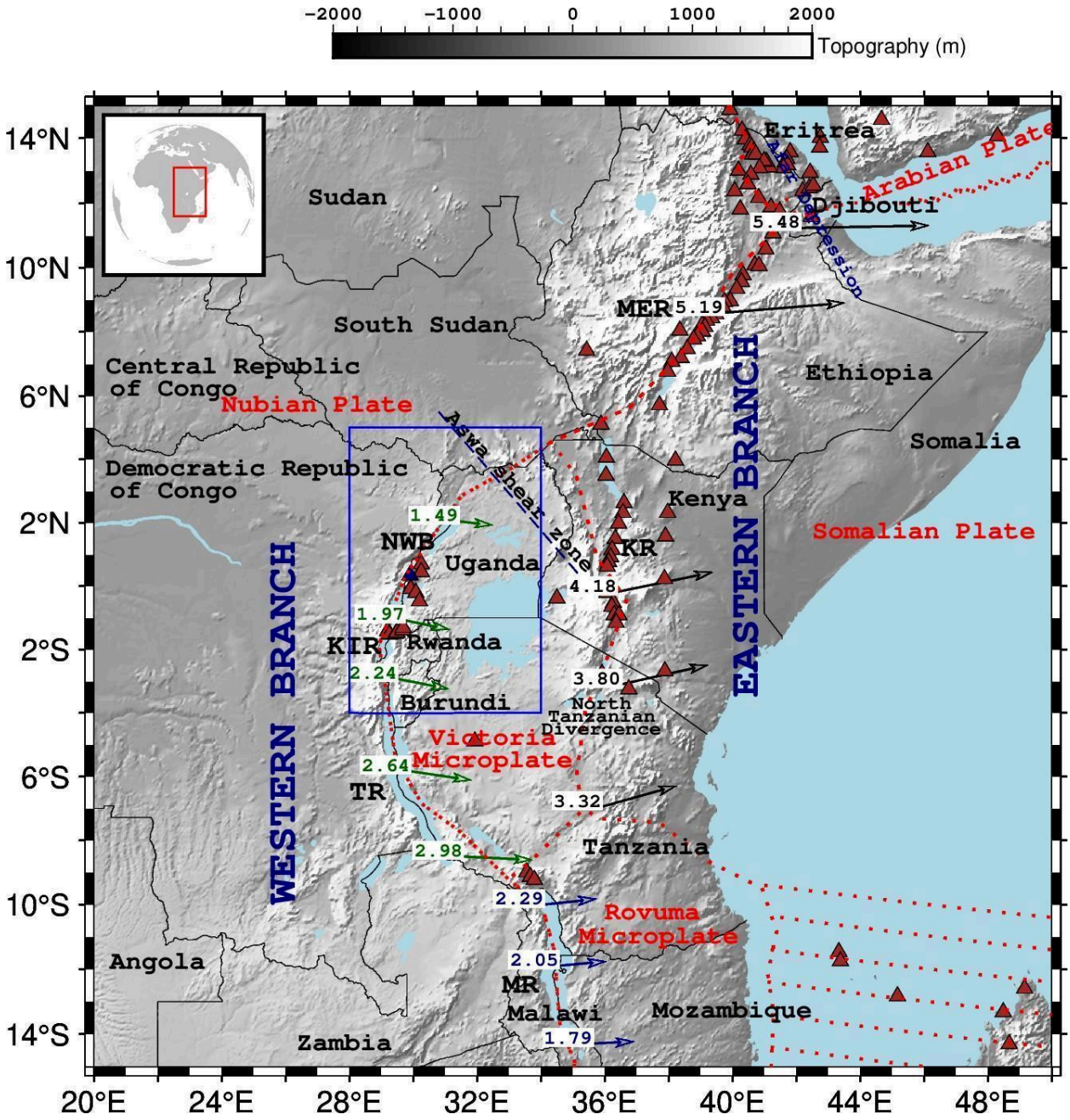

Figure 1: The map shows the continental EARS, displaying the Eastern and Western Branches, with red dotted lines indicating plate boundaries and deforming zones (Stamps et al., 2021). Vectors are predicted surface motions in mm/y (the values are indicated next to vectors) from the kinematic model (Stamps et al., 2021), with black vectors representing the Somalian plate relative to the Nubian plate, green vectors representing the Victoria microplate relative to the Nubian plate, and blue vectors representing the Rovuma microplate relative to the Nubian plate. Brown triangles represent Holocene volcanoes (Global Volcanism Program, 2013) in the region, while navy blue triangles represent a peak in the Rwenzori Mountains. The study area is denoted by a solid blue rectangle (shown in Figure 2), while the inset map shows the relative location of

part of the continental EARS (red color) on Earth. NWB = Northern Western Branch; MER = Main Ethiopian Rift; KIR = Kivu Rift; TR = Tanganyika Rift; KR = Kenya Rift; and MR = Malawi Rift.

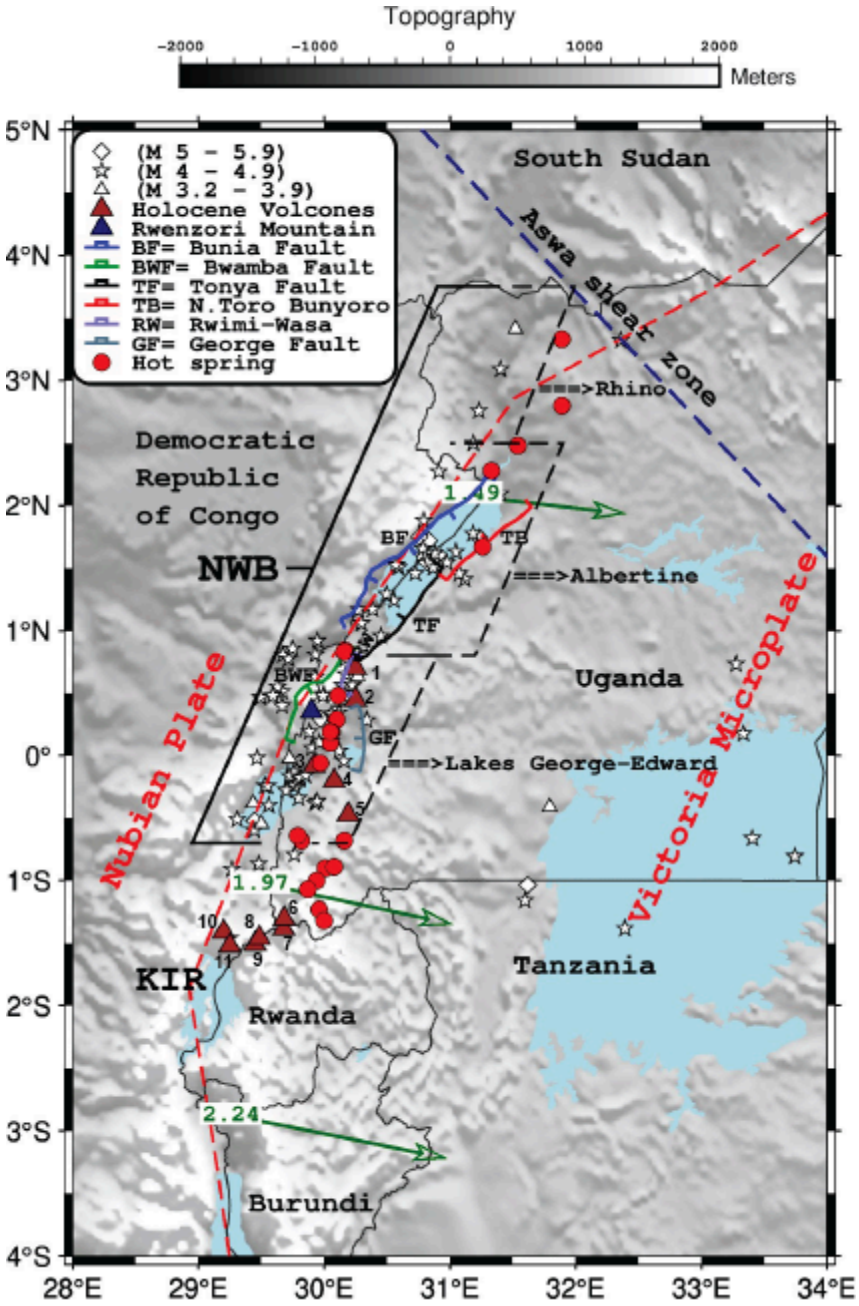

Figure 2: The map shows the study region, including the plate boundary shown as dashed red lines (Stamps et al., 2021), earthquakes from the National Earthquake Information Center catalog (Masse & Needham, 1989) from 2000 to 2024 represented as small white stars, triangles, and diamonds. Green vectors representing predicted surface motions in mm/y of the Victoria microplate relative to the Nubian plate (Stamps et al., 2021). Holocene volcanoes are brown triangles (Global Volcanism Program, 2013); 1 = Fort Portal Field; 2 = Kyatwa; 3 =

Katwe-Kikorongo Field; 4 = Bunyaruguru Field; 5 = Mount Katunga; 6 = Bufumbira; 7 = Muhavura; 8 = Gahinga; 9 = Sabinyo; 10 = Bisoke ; and 11 = Karisimbi. The navy blue triangle represents a peak of the Rwenzori Mountains. Hot springs are red circles. Major faults in the region are represented by blue, green, black, red, slate blue, and sky blue lines. BF = Bunia Fault; BWF = Bwamba Fault; TF = Tonya Fault; TBF = North Toro Bunyoro Fault; RWF = Rwimi- Wasa Fault; GF = George Fault.

2. Geological Background and Tectonic Setting

The lithospheric structure of Africa consists of several major Archaean cratons between 3.6 and 2.5 Ga (Begg et al., 2009), such as the West African craton in west-northwest Africa; the Congo Craton in western central Africa; the Tanzania Craton in eastern central Africa; and the Kalahari in southern Africa (e.g., Begg et al., 2009; Emry et al., 2019). The African cratons are bordered by mobile belts where previous collisional and extensional events occurred during the Late Neoproterozoic to earliest Paleozoic Pan-African orogenic events (e.g., Begg et al., 2009; Ennih *&* Liégeois, 2008; Jessell et al., 2016; Link et al., 2010).

The Eastern Branch of EARS was initiated between 45-37 Ma ago, while the Western Branch was initiated between 25-20 Ma (Roberts et al., 2012). The continental portion of the EARS comprises largely of the magma-rich Eastern Branch and the mostly magma-poor Western Branch that bound the Archaean Tanzania Craton (Figure 1). The Eastern Branch is about 2,300 *km* long and extends from the Afar depression in the north to the basins of the North-Tanzanian divergence zone in the south passing through the Main Ethiopian Rift and the Kenyan Rift (Figure 1). The Western Branch of the EARS is approximately 2,800 *km* long stretching from the Rhino and Albertine grabens in the north through the Kivu Rift and Malawi Rift to the Urema graben in Mozambique to the south.

The Albertine and Rhino Grabens extend about 330 km northeast of the Rwenzori Mountains, with widths ranging from 60–80 km but narrowing to 10–40 km within the Rhino Graben. The Lakes George-Edward Graben extends approximately 250 km southwest of the Rwenzori Mountains, with widths between 45–65 km.

The northern Western Branch forms part of the plate boundary between the Nubian Plate and the Victoria Microplate (Figures 1 and 2). The EARS includes at least four microplates: Lwandle, Rovuma, San, and Victoria (Hartnady, 2002; Saria et al., 2014; Stamps et al., 2008; Wedmore et al., 2021). Predicted extension rates from GPS-constrained kinematic models range from about 1.5 mm/y around the Albertine and Rhino Grabens to 2 mm/y around the Lakes George-Edward Graben (Saria et al., 2014; Stamps et al., 2021).

The Albertine Graben is an asymmetrical full graben bordered by the Bunia Fault to the west and the North Toro Bunyoro and Tonya Faults to the east (Figure 2; Bwambale et al., 2015). Similarly, the Lakes George-Edward Graben is asymmetrical, bordered by the Bwamba Fault on the west and the Rwimi-Wasa, George, and Tonya Faults on the east (Figure 2; Bwambale et al., 2015). The Rhino Graben terminates to the north along the northwest-striking Aswa Shear Zone (Figure 2; Katumwehe et al., 2015; 2016).

The Rwenzori Mountains are a peculiar high topographic feature in the Western Branch (Figures 1 and 2). This horst mountain made up of Precambrian basement rocks rises more than 5 *km* above sea level. The Rwenzori Mountains, which border Uganda and the Democratic Republic of the Congo, are located within the rift interaction zone between the Lakes George-Edward graben and the southern Albertine graben (Bauer et al., 2010; Bauer et al., 2013; Pickford et al., 1993; Ring, 2008; Ring, 2014).

Magmatism along the Western Branch is of limited extent and confined to four volcanic fields, namely the Toro-Ankole, Virunga, South Kivu, and Rungwe volcanic fields, which extend from north to south (Ebinger et al., 1993; Pasteels et al., 1989; Ring, 2014). Holocene volcanoes (Fort Portal, Kyatwa, Katwe-Kikorongo, Bunyaruguru, Katunga, Bufumbira, and Muhavura) in the magma-rich Lakes George-Edward graben (Figure 2) are collectively known as the Toro-Ankole Volcanic province and are the only ones located within our study area (Combe & Holmes, 1947; Pasteels et al., 1989). The types of volcanoes that comprise the Toro-Ankole province are consistent with phreatic eruptions, which include tuff cones and maar craters, some of which contain lakes and hot springs (Combe & Holmes, 1947; Sigurdsson et al., 2015). The geochemistry of the volcanoes in Toro-Ankole province is carbonatitic, silica-depleted, and potassium-rich (e.g., Barker & Nixon, 1989; Combe & Holmes, 1947; Ennih and Liégeois, 2008; Rogers, 2006; Rosenthal et al., 2009). In addition, helium and neon isotopes suggest a strong plume contribution to the Toro-Ankole volcanoes (Barry et al., 2013; Halldorsson et al., 2014; Hilton et al., 2011; Pik et al., 2008). In addition to volcanic centers, hot springs have been observed along the northern Western Branch, including both the magma-rich Lakes George-Edward graben and the magma-poor Albertine and Rhino grabens (Figure 2).

3. Previous Geophysical Studies

A sequence of earthquakes in South Sudan from 1990 to 1991 was initially interpreted as evidence of the Western Branch of the East African Rift System (EARS) extending northeast beyond the Rhino Graben (Girdler & McConnell, 1994). However, analysis of airborne magnetic data by Katumwehe et al. (2015) revealed that the Rhino Graben does not extend beyond the Aswa Shear Zone. Katumwehe et al. (2015) further proposed that the heterogeneous and thinning lithosphere of the Saharan Metacraton, lacking a well-developed pre-existing lithospheric fabric, may have hindered strain localization during the onset of rifting. This likely caused the Western Branch to terminate against the Aswa Shear Zone. The existence of small-scale active faults propagating northward remains uncertain.

Earthquakes with magnitudes ranging from 3.2 to 5.9 have been observed in the northern Western Branch from 2000 to 2024 (Figure 2; Masse & Needham, 1989). As part of the RiftLink project, approximately 800 microseismicity events per month with local magnitudes (M_L) ranging from -0.5 to 5.1 with a focal depth ranging from 10 to 59.5 *km* were recorded within the fault zones to the east, west and north of the Rwenzori mountains area for a period of 19 months from April 2006 to October 2007 (Lindenfeld et al., 2012; Lindenfeld & Rümpker, 2011). In areas where magmatism is widespread and the lithosphere has thinned along the rift, earthquakes

do not tend to occur at deep depths; rather, they are confined to the upper 15 *km* of the crust. However, in magma poor areas, the focal depth has been found to extend to depths of 35 ± 5 *km* (Craig et al., 2011; Yang and Chen, 2010). Lower crustal earthquakes have been observed along both the Western and Eastern Branches of the EARS, in contrast to most intracontinental rifts where seismicity is confined to the upper crust (Albaric et al., 2014; Craig et al., 2011; Ebinger et al., 2019; Jackson & White 1989; Lavayssière et al., 2019; Lindenfeld et al., 2012; Nyblade & Langston 1995; O'Donnell et al., 2016; Yang & Chen, 2010).

Previous studies including gravity (Ebinger et al., 1989), petrological (Aulbach et al., 2008), geochemical (Halldórson et al., 2014), seismic (Mulibo & Nyblade, 2013; Bastow et al., 2008), and geodynamic (Koptev et al., 2015) support active rifting models in which one or more mantle plumes play a role in the development of the EARS. In contrast, there are also several geodynamic studies that propose forces from gravitational potential energy gradients from high topography maintain present-day rifting along weakened plate boundaries (Coblentz & Sandiford, 1994; Rajaonarison et al., 2021; 2023; Stamps et al., 2010; 2014; 2015). Buoyancy from the mantle plumes beneath Africa have been identified as the driving force behind the abnormally high topography in southern and eastern Africa (Hansen & Nyblade, 2013; Moucha et al., 2011). According to new estimates of mantle potential temperatures (T_p), elevated mantle temperatures are a common feature of the upper mantle beneath East Africa, and the African superplume contributes to the markedly slow seismic velocities beneath East Africa (Rooney et al., 2020; 2012).

Gravity and seismic studies also show that beneath the Western and Eastern Branches of the EARS, there is relatively thin lithosphere underlain by anomalous low-density material compared to the thick lithosphere of the Tanzania craton sandwiched in between the two rift Branches (e.g., Fadaie & Ranalli,1990; Fairhead 1976; Savage & Long 1985). The crust associated with the Western Branch is approximately 40 *km* thick with the lithospheric mantle up to 150 *km* deep (Afonso et al., 2022; O'Donnell et al., 2016; Pasyanos et al., 2014). Seismic studies that were conducted as part of the RiftLink research project on the Tanzania craton and the adjacent Western Branch of the EARS indicated that the upper boundary of the lower lithosphere has been mineralogically altered due to metasomatism induced by infiltration of melts derived from the asthenosphere or by partially melting the base of the lithosphere (Wölbern & Rumpker, 2012). Using seismic data, Gummert et al. (2016) found high Vp/Vs ratios in the Albertine rift segment, the Edward rift segment, and the Rwenzori Mountains, which they associated with decompression melting or ascending dykes of asthenospheric material. Beneath the Lake Edward and Lake George basins, reduced S-wave velocities at 15 km depth were detected and attributed to the presence of partial melt beneath this region (Wölbern et al., 2010). However, these studies focused mainly on the Edward and southernmost Albertine rift segments and did not extend to the northernmost tip of the Western Branch, therefore remaining enigmatic.

4. Methods

We model 3D melt generation associated with Lithospheric Modulated Convection and Tomography-Based Convection in the upper mantle using the open-source and CIG-supported finite element code entitled Advanced Solver for Planetary Evolution, Convection, and Tectonics (ASPECT) version 2.2.0 (Bangerth et al., 2018; Dannberg & Heister, 2016; Kronbichler et al., 2012). The use of these two distinct mantle convection methods aims to explore two potential mechanisms for melt generation beneath the northern Western Branch. The Lithospheric Modulated Convection model posits that upper mantle convection is driven by temperature variations caused by lateral differences in lithospheric thickness, representing small-scale convection similar to edge-driven convection (Njinju et al., 2021; King & Anderson, 1998). In contrast, the Tomography-Based Convection model assumes that convection arises from temperature variations driven by both lateral lithospheric thickness variations and upper mantle temperature anomalies derived from a shear wave velocity model (Njinju et al., 2023). For the Lithospheric Modulated Convection model, lithospheric thickness data from Afonso et al. (2022) were used as inputs, while the Tomography-Based Convection model utilizes the shear wave velocity model based on ambient noise tomography from Emry et al. (2019), in addition to lithospheric thickness data from Afonso et al. (2022).

4.1. Modeling Approach

Geodynamic modeling is a powerful tool for investigating processes below the Earth's surface (van Zelst et al., 2022). In this work, we calculate forward models to solve equations that describe the physical processes of mantle convection and melt generation. We use ASPECT to solve the conservation of mass, momentum, and energy equations (see Section 4.2) according to the anelastic liquid approximation (Jarvis & McKenzie, 1980). The solutions to these three equations define how the material's velocity, pressure, and temperature (i.e., the dependent or unknown variables) change in space and how they evolve when one or more independent or known variables change, e.g., density. The anelastic liquid approximation assumes small lateral density variations relative to a reference density profile, which can be ignored in the mass (eq. 1) and energy conservation equations (eq. 3); only the buoyancy term in the momentum conservation equation (eq. 2) uses a temperature- and pressure-dependent density (Jarvis & McKenzie, 1980; van Zelst et al., 2022). The computation time for the Lithospheric Modulated Convection model is 20 million years to reach steady-state, whereas the Tomography-Based Convection model is instantaneous since it is constrained by present-day seismic tomography.

4.2. Governing Equations

We solve for velocity, pressure, and temperature using the compressible Stokes equations, i.e., the conservation of mass equation (eq. 1), the conservation of momentum equation (eq. 2), and the conservation of energy (eq. 3) according to anelastic liquid approximation. These equations are partial differential equations describing the relation between the unknowns (velocity, pressure, and temperature) and their partial derivatives concerning space and time.

$$\nabla \cdot (\rho_r \mathbf{v}) = 0 \qquad \text{(eq. 1)}$$

$$-\nabla \cdot \left[2\eta_{\text{eff}} \left(\dot{\varepsilon}(\mathbf{v}) - \frac{1}{3}(\nabla \cdot \mathbf{v})\mathbf{I} \right) \right] + \nabla P = \rho \mathbf{g} \qquad \text{(eq. 2)}$$

where **v** is the velocity vector, **I** is the identity matrix, η_{eff} is the effective viscosity which depends on temperature and pressure, ($\dot{\varepsilon}$(**v**) - ⅓($\nabla \cdot$ **v**)**I**) is the deviatoric strain rate tensor, P is the pressure, **g** is the gravitational acceleration, ρ is the density, and ρ_r is the depth-dependent reference density according to the anelastic liquid approximation (Jarvis & McKenzie, 1980). To obtain the reference density profile, we use the AK135 global average Earth Model (Kennett et al. 1995). The energy equation (eq. 3) is used to model the advection and diffusion of temperature (thermal evolution) without considering internal heat production.

$$\rho_r C_p \left(\frac{\partial T}{\partial t} + \mathbf{v} \cdot \nabla T \right) - \nabla \cdot (\kappa \nabla T) = \left[2\eta_{\text{eff}} \left(\dot{\varepsilon}(\mathbf{v}) - \frac{1}{3}(\nabla \cdot \mathbf{v})\mathbf{I} \right) \right] : \left(\dot{\varepsilon}(\mathbf{v}) - \frac{1}{3}(\nabla \cdot \mathbf{v})\mathbf{I} \right)$$

$$+ \alpha T(\mathbf{v} \cdot \nabla P) + \rho_r T \Delta S \left(\frac{\partial X}{\partial t} \right) + \mathbf{v} \cdot \nabla X \qquad \text{(eq. 3)}$$

where ρ_r is the depth-dependent reference density profile, C_p is the heat capacity, T is the temperature, t is the time, **v** is the velocity vector, κ is the thermal conductivity, [$2\eta_{\text{eff}}$ ($\dot{\varepsilon}$(**v**) - ⅓($\nabla \cdot$ **v**)**I**) : ($\dot{\varepsilon}$(**v**) - ⅓($\nabla \cdot$ **v**)**I**)] is the shear heating term, $\alpha T(\mathbf{v} \cdot \nabla P)$ is the adiabatic heating term where α is the thermal expansivity and P is the pressure, $\rho_r T \Delta S(\partial X / \partial t)$+ **v** $\cdot \nabla X$ is the latent heat term where ΔS is the change of entropy and X is the melt fraction (see section 4.4).

We characterize the changes in density, ρ, in eq. 2 with pressure (P) and temperature (T) in terms of compressibility and thermal expansivity, as shown in eq. 4:

$$\rho = (\rho_0 + \Delta\rho)\, \alpha(T - T_0)\, \exp\left[\beta(P - P_0)\right] \qquad \text{(eq. 4)}$$

where where ρ_0 is the reference solid density, Δρ is the depletion density change of the material (peridotite), P_0 is the reference pressure, T_0 is the reference temperature, exp is the natural exponential equal to 2.718, α is the thermal expansivity, and β is the compressibility coefficient. The values and units used in the mantle convection and melt generation simulation are shown in Table 1.

4.3. Rheology

Rheology describes how materials deform or flow when they are exposed to stresses. Our models use diffusion creep and dislocation creep (eq. 5; Karato & Wu, 1993; Karato, 2008) in the sub-lithospheric mantle. We create a composite rheology as shown in eq. 6, which is the harmonic average of diffusion creep and dislocation creep (Jadamec & Billen, 2010). In our model, we are only interested in modeling asthenospheric processes (i.e., lithospheric mantle flow and deep melt generation), therefore, we make the lithosphere rigid by imposing a high viscosity of 10^{24} Pa.*s* as shown in Figure 3.

$$\eta_{\text{diffusion, dislocation}} = \tfrac{1}{2}\, d^{m/n}\, A^{-1/n}\, \dot{\varepsilon}_e^{(1-n)/n}\, \exp\left(\frac{E_a + PV_a}{nRT}\right) \qquad \text{(eq. 5)}$$

$$\eta_{\text{eff}} = \left(\frac{\eta_{\text{diffusion}}\, \eta_{\text{dislocation}}}{\eta_{\text{diffusion}} + \eta_{\text{dislocation}}}\right) \qquad \text{(eq. 6)}$$

where η_{eff} is the effective viscosity, d is the grain size, m is the grain size exponent, n is the stress exponent, exp is the natural exponential equal to 2.718, A is the pre-exponential factor, $\dot{\varepsilon}_e$ is the effective deviatoric strain rate, P is the pressure, E_a is the activation energy, V_a is the activation volume, R is the gas constant, and T is the temperature. The values of the parameters are shown in Table 1. We note that we do not account for the effects of water on viscosity.

Table 1: Parameters used in the mantle convection and melt generation simulations based on several geodynamic studies that model similar tectonic settings.

Notation	Parameter	Value	Unit	Reference
β	Compressibility coefficient	5.124 x 10^{-12}	Pa^{-1}	Glerum et al. (2018)
ρ_c	Density of crust	2700	$kg.m^{-3}$	
ρ_m	Density of mantle lithosphere	3300	$kg.m^{-3}$	
g	Gravitational acceleration	Preliminary Reference Earth Model (PREM)	$m.s^{-2}$	Dziewonski & Anderson (1981)
T_p	Mantle potential temperature	1693, 1703, 1713, 1723	K	Rooney et al. (2012; 2020)

	Pressure normalization	surface	*Pa*	Rajaonarison et al. (2020)
P_o	Reference pressure	0	*Pa*	
ρ_o	Reference solid density	3300	$kg.m^{-3}$	Rajaonarison et al. (2020)
ρ_r	Reference density profile	AK135 model	$kg.m^{-3}$	Kennett et al. (1995)
$\mathbf{v}_r$	Reference shear wave velocity profile	AK135 model	$km.s^{-1}$	Kennett et al. (1995)
$\mathbf{v}_s$	Shear wave velocity	Seismic tomography model	$km.s^{-1}$	Emry et al. (2019)
C_p	Reference specific heat capacity	1250	$J.kg^{-1}.K^{-1}$	Rajaonarison et al. (2020)
$\dot{\varepsilon}(\mathbf{v})$	Reference strain rate for first time-step	1×10^{-15}	s^{-1}	Rajaonarison et al. (2020)
T_o	Reference temperature	293	K	Njinju et al. (2021; 2023)
κ	Thermal conductivity	4.0	$W.m^{-1}.K^{-1}$	Turcotte & Schubert (2002)
α	Thermal expansivity	5×10^{-5}	K^{-1}	
t (Lithospheric Modulated Convection)	Computational end time	20	My	Njinju et al. (2021; 2023)
E_{sdf}	Activation energy (Diffusion creep)	3.0×10^5	$J.mol^{-1}$	Karato & Wu (1993); Turcotte & Schubert (2002)
E_{sdl}	Activation energy (Dislocation creep)	5.4×10^5	$J.mol^{-1}$	Karato & Wu (1993); Turcotte & Schubert (2002)

V_{df}	Activation volume (Diffusion creep)	6×10^{-6}	$m^3.mol^{-1}$	Karato & Wu (1993); Turcotte & Schubert (2002)
V_{dl}	Activation volume (Dislocation creep)	2×10^{-5}	$m^3.mol^{-1}$	Karato & Wu (1993); Turcotte & Schubert (2002)
d_{df}	Grain size (Diffusion creep)	0.01	m	Rajaonarison et al. (2020); Glerum et al. (2018)
d_{dl}	Grain size (Dislocation creep)	0	m	Rajaonarison et al. (2020)
m_{dfz}	Grain size exponent (Diffusion creep)	2.5	none	Karato & Wu (1993); Turcotte & Schubert (2002)
m_{dl}	Grain size exponent (Dislocation creep)	0	none	Karato & Wu (1993); Turcotte & Schubert (2002)
A_{df}	Pre-exponential factor (Diffusion creep)	1.50×10^{-15}	$Pa^{(1/ndf)}.m^{(ndf/mdf)}.s^{-1}$	Rajaonarison et al. (2020)
A_{dl}	Pre-exponential factor (Dislocation creep)	6.52×10^{-16}	$Pa^{(1/ndl)}.m^{(ndl/mdl)}.s^{-1}$	Naliboff et al. (2020); Rajaonarison et al. (2020)
η_{r_bulk}	Reference bulk viscosity	1×10^{22}	$Pa.s$	
η_{r_shear}	Reference shear viscosity	5×10^{20}	$Pa.s$	
n_{df}	Stress exponent (Diffusion creep)	1.0	none	Karato & Wu (1993); Turcotte & Schubert (2002)

n_{dl}	Stress exponent (Dislocation creep)	3.5	none	Karato & Wu (1993); Turcotte & Schubert (2002)
η_{min}	Minimum viscosity	10^{19}	*Pa.s*	
η_{max}	Maximum viscosity	10^{24}	*Pa.s*	

4.4. Melt Parameterization

To enable the formation of melt in our model, we use the Katz et al. (2003) melt parameterization, which is applicable up to 13 GPa (~350 km depth). This approach uses batch (equilibrium) melting where a finite amount of melt forms in a closed system and chemical equilibrium is maintained between the phases, i.e., no melt erupts out of the system and there are no injections of fresh melt into the system. Melt and solids stay intermingled as a closed system until melting ceases, thus the amount of melt that would normally be extracted from the asthenosphere into the lithosphere (often called degree of melt) is combined with the volume of melt present at any given point in time in the asthenosphere. Therefore, our melt fraction values may be slightly higher than expected if one is only considering the volume of melt present at a point in time in the asthenosphere. Although melt is likely to escape upwards in a natural setting and seismic velocity wave-speeds can be impacted by the shape of melt pockets and aspect ratio of melt inclusions, we take a relatively simple approach with batch melting such that we provide an end-member estimate of the degree of melting. We used the simple polynomial relationships (eq. 7 and eq. 8) between temperature and pressure to parameterize the solidus and liquidus of a dry peridotite system (lherzolite), which we employ in our model (Katz et al., 2003):

$$T_{\text{Solidus}} = A_1 + A_2 P + A_3 P^2 \qquad \text{(eq. 7)}$$

$$T_{\text{Lherzolite Liquidus}} = B_1 + B_2 P + B_3 P^2 \qquad \text{(eq. 8)}$$

where P = pressure in GPa, A_1 = 1085.7 ℃, A_2= 132.7℃ GPa^{-1}, A_3= -5.1 ℃ GPa^{-2}, B_1= 1475.0 ℃, B_2= 8.0 ℃ GPa^{-1}, B_3= -3.2 ℃ GPa^{-2}. Given that there is no active subduction near our region of study introducing water into the sublithospheric mantle, we choose a dry peridotite system.

In order to quantify the amount of melt generated by the system, we incorporate latent heat (the last term in eq. 3), which is heat generated or consumed in the process of phase change of the material. The latent heat is proportional to the density, temperature, change of entropy (ΔS), and changes in the fraction of the material that has already undergone the phase transition (X) (also called phase function). In our case, this phase transition is associated with melting of the upper

mantle, thus X is the melt fraction. Melt fraction is calculated for temperatures (T) that are less than the lherzolite liquidus ($T_{\text{LherzoliteLiquidus}}$) but greater than the solidus (T_{Solidus}) using eq. 9 below that is based on Katz et al. (2003):

$$X = \left(\frac{T - T_{\text{Solidus}}}{T_{\text{Lherzolite Liquidus}} - T_{\text{Solidus}}} \right)^{\omega} \qquad \text{(eq. 9)}$$

where the exponent of melting temperature, denoted as $\boldsymbol{\omega}$, is equal to 1.5 following Katz et al. (2003).

4.5. Model Geometry

We use the 3D chunk geometry (Figure 3) in our Lithospheric Modulated Convection and Tomography-Based Convection models, which is defined by the ASPECT code as a chunk of a spherical shell bounded by minimum and maximum longitudes, minimum and maximum latitudes, and outer and inner radii or depth. The chunk geometry labels are "west" and "east" to represent minimum and maximum longitudes, "south" and "north" to represent minimum and maximum latitudes, and "outer" and "inner" to represent the minimum (surface) and the maximum depth. The minimum longitude in our model is 24°, the maximum longitude is 38°, the minimum latitude is -8°, the maximum latitude is 9°, the minimum depth is 0 *km*, and the maximum depth is 660 *km*, giving our model edge lengths of 1777.6 x 1555.4 x 660 *km* in the latitude, longitude, and depth directions (Figures 3). We make the model geometry larger than the study region shown in Figures 1 and 2 to avoid edge boundary effects following Njinju et al. (2021). The model domain comprises three compositional layers; uniform crustal thickness (30 km), mantle lithosphere (variable thickness), and sublithospheric mantle. For all experiments, we discretize the model with a global mesh refinement of 6, which implies that each finite element (or cell) has a dimension of 27.8 by 24.3 by 10.3 *km* in the latitude, longitude, and depth directions. The cell size is calculated by obtaining the edge length and dividing it by 2^n where n is the global mesh refinement, which is 6 in our case. We do not use adaptive mesh refinement throughout our model.

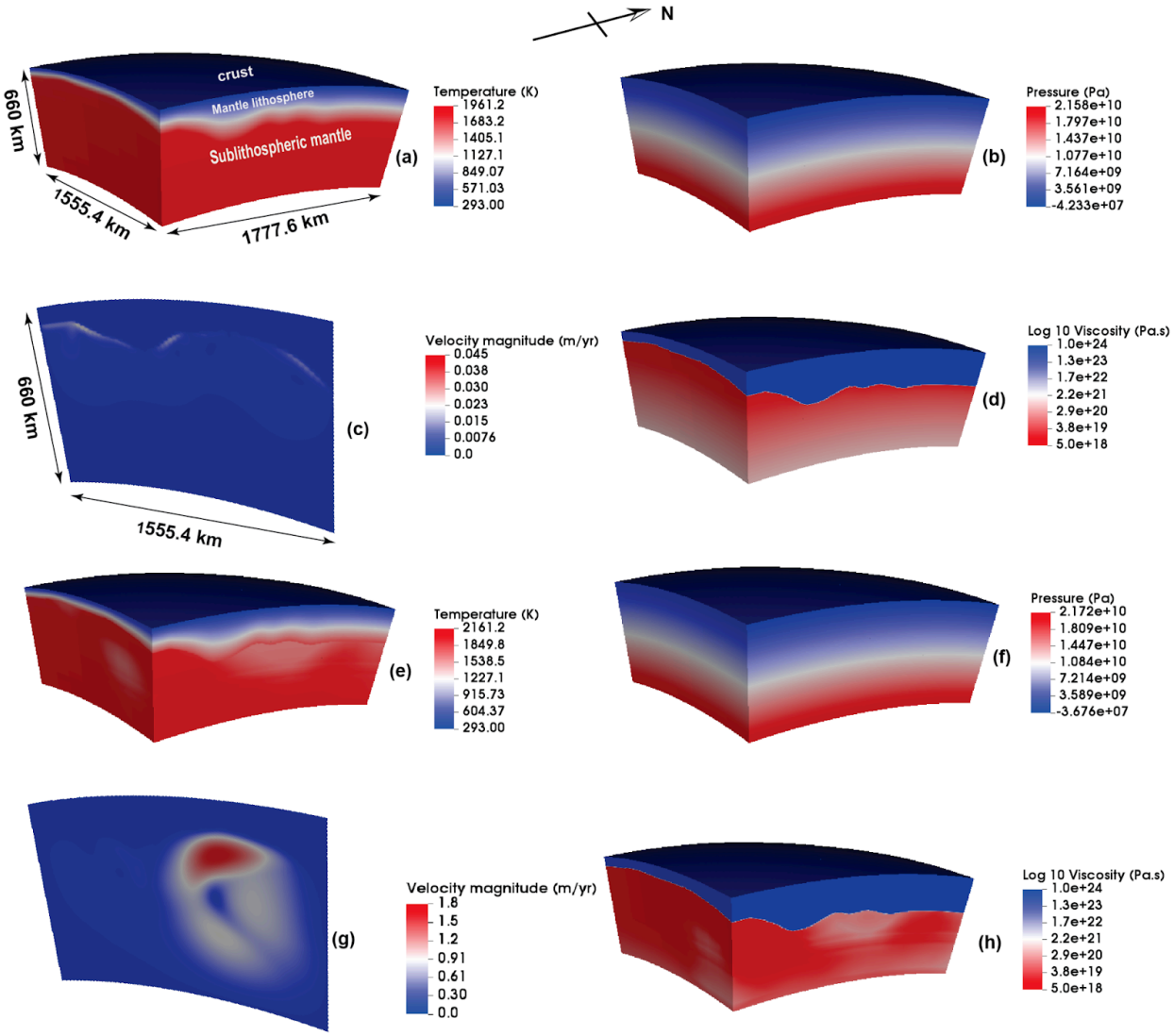

Figure 3. Model set up a) initial temperature for Lithospheric Modulated Convection model, b) initial pressure for Lithospheric Modulated Convection model, c) initial velocity magnitude for Lithospheric Modulated Convection model (cross-section at 0° latitude), and d) initial viscosity ($\log_{10}$) for Lithospheric Modulated Convection model, e) initial temperature for Tomography-Based Convection model, f) initial pressure for Tomography-Based Convection model, g) initial velocity magnitude for Tomography-Based Convection model (cross-section at 0° latitude), and h) initial viscosity ($\log_{10}$) for Tomography-Based Convection model.

4.6. Initial and Boundary Conditions

4.6.1. Lithospheric Modulated Convection

The Lithospheric Modulated Convection models have an initial temperature of 293 K at the outer side (minimum depth), which increases linearly up to the LAB (Figure 3a). At the LAB, the temperature is calculated based on the mantle potential temperature (T_p) we are

experimenting with (i.e. 1693, 1703, 1713 or 1723 K), the gravitational acceleration (g), thermal expansivity (α), the heat capacity (C_p) and the depth ($z_{LAB(i)}$) to the LAB at location *i*, as shown in eq.10 and Figure 4a. The mantle potential temperatures we are using (both in Lithospheric Modulated Convection and Tomography-Based Convection models) are based on the petrologically derived estimates of Rooney et al. (2020; 2012) around the northern Western Branch.

$$T_{(z_{\mathrm{LAB}(i)})} = T_p \exp\left(\frac{g\alpha z_{\mathrm{LAB}(i)}}{C_p}\right) \qquad \text{(eq. 10)}$$

where $T(z_{LAB(i)})$ is the temperature at the LAB for the Lithospheric Modulated Convection models (and Tomography-Based Convection models), T_p is the mantle potential temperature with which we are experimenting, exp is the natural exponential equal to 2.718, g is the gravitational acceleration, α is the thermal expansivity, $z_{LAB(i)}$ is depth at the LAB at location (*i*), and and C_p is the heat capacity following the formulation of McKenzie & Bickle (1988).

Below the LAB, the geothermal gradient is fully adiabatic, thus the temperature (eq.11) increases adiabatically until the model base (inner side) at 660 *km*, where the temperature remains constant but varies laterally across the model (McKenzie & Bickle, 1988).

$$T\left(z_{\mathrm{depth}>\mathrm{LAB}(i)\_\mathrm{lith}}\right) = T_p \exp\left(\frac{g\alpha z_{\mathrm{depth}>\mathrm{LAB}(i)\_\mathrm{lith}}}{C_p}\right) \qquad \text{(eq. 11)}$$

where $T(z_{depth>LAB(i)\_lith})$ is the temperature between the LAB and 660 *km* depth for the Lithospheric Modulated Convection models, T_p is the mantle potential temperature with which we are experimenting, exp is the natural exponential equal to 2.718, g is the gravitational acceleration, α is the thermal expansivity, $z_{depth > LAB(i)\_lith}$ is the depth below the LAB at location *i*, and C_p is the heat capacity.

The thermomechanical models used here require boundary conditions for solving mass, momentum, and energy conservation equations (e.g., van Zelst et al., 2022). For the temperature boundary conditions, the Lithospheric Modulated Convection models set no heat flux (insulating) on the west, east, south, and north sides of the chunk geometry, instead focusing on the heat flux in the inner and outer sides (bottom and top boundaries). We do not provide initial velocity or pressure conditions since the conservation equations for mass and momentum do not include time derivatives of velocity or pressure. However, we impose velocity boundary conditions that are free-slip (tangential) along the outer side of the chunk geometry, while the remaining sides are set with no-slip (zero fixed) velocity boundary conditions. The free-slip boundary condition, where the velocity normal to the boundary is zero and there are no parallel

stresses, allows material to flow freely along the boundary. The no-slip boundary condition is a prescribed velocity with zero velocity at the boundary.

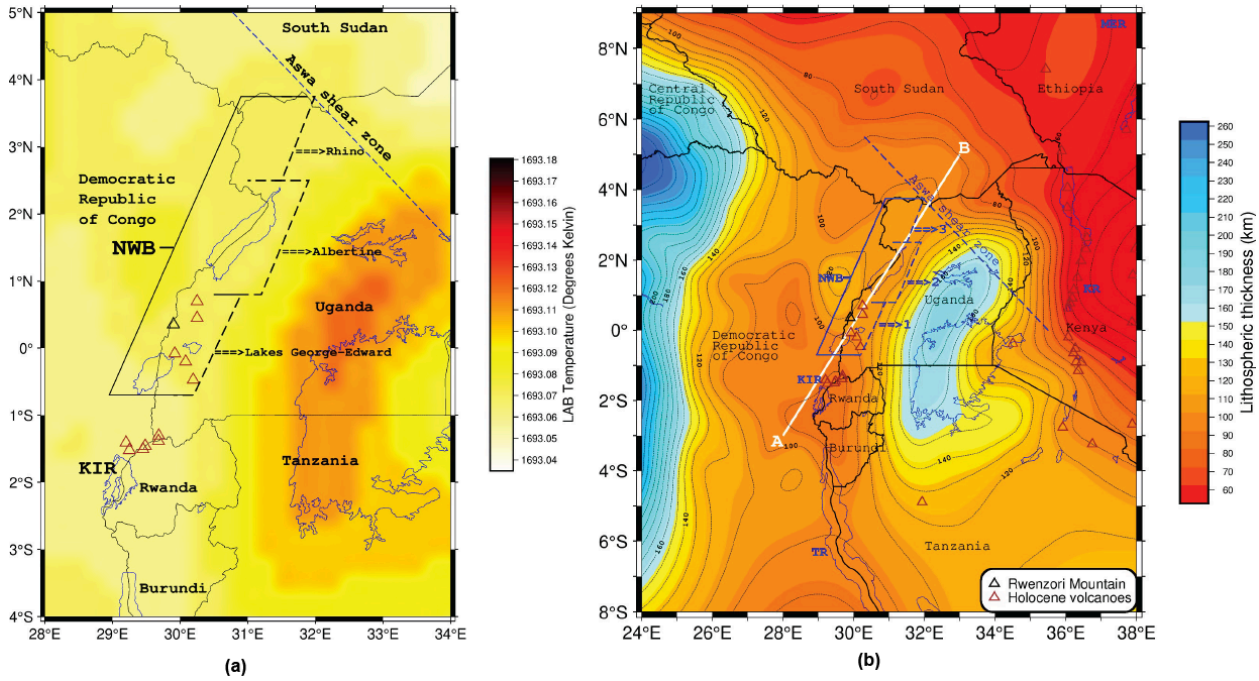

Figure 4 a): LAB temperatures beneath the study region for mantle potential temperature 1693 K. The LAB temperatures are calculated based on eq. 10. Note that the LAB temperatures are higher where the lithospheric thickness (Figure 4b) is higher, based on eq. 10. **b)** Lithospheric thickness map of the study area based on the Afonso model (Afonso et al., 2022). Lithospheric thickness beneath the northern Western Branch ranges from 94 beneath the Lake George graben to 120 *km* beneath the Albertine and Rhino grabens. A lithospheric thickness of ~160 *km* underlies the Tanzanian Craton while the Kenyan Rift has a lithospheric thickness of ~60 *km*. Black triangle represents a peak in the Rwenzori Mountains, red triangles represent Holocene volcanoes, and dashed lines show contour intervals of 10 *km* lithospheric thickness. NWB = Northern Western Branch; KIR = Kivu Rift; TR = Tanganyika Rift; MER = Main Ethiopian Rift; KR = Kenya Rift; 1 = Lakes George-Edward graben; 2 = Albertine graben; 3 = Rhino graben. White line is the profile AB defined in Figure 6.

4.6.2. Tomography-Based Convection

The Tomography-Based Convection models also have an initial temperature of 293 K at the outer side (minimum depth), which increases linearly up to the LAB. At the LAB, the temperature is also calculated in the same way as the LAB models as shown eq.10 and Figure 4a. Below the LAB, the geothermal gradient is also fully adiabatic, thus the temperature increases adiabatically until the model base (inner side) at 660 *km*, but in this style of convection we also add a temperature anomaly constrained by shear wave velocities (eq. 12).

Between the LAB and 660 *km* depth, we use shear wave velocities from the Emry et al. (2019) seismic tomography model and a depth-dependent scaling factor of 0.2 to convert shear wave velocities into density anomalies and later to temperature anomalies, following on Njinju et al. (2023) and ref. therein as shown in eq.12.

$$\delta T = \frac{\delta \rho}{\rho_r} \cdot \frac{1}{\alpha} \qquad \text{(eq. 12)}$$

where δT is the temperature anomaly, the density anomaly is $\delta\rho$ = ($^{v_s}/_{v_r}$ * 0.2), v_s is the shear wave velocity (Emry et al., 2019), v_r is the reference shear wave velocity (Kennett et al., 1995), ρ_r is the reference density (Kennett et al., 1995), and α is the thermal expansivity.

We add these temperature anomalies (δT) to the ambient temperature as shown in eq. 13. We note that a limit on the temperature anomalies of -200 to 200 K is implemented to avoid an excess increase in the reference temperature profile in the upper mantle (Turcotte & Schubert, 2002) following a similar approach implemented in Rajaonarison et al. (2023).

$$T\left(z_{\text{depth}>\text{LAB}(i)\_\text{tomo}}\right) = T_p \exp\left(\frac{g\alpha z_{\text{depth}>\text{LAB}(i)\_\text{tomo}}}{C_p}\right) + \delta T \qquad \text{(eq. 13)}$$

where $T(z_{\text{depth}>\text{LAB}(i)\_\text{tomo}})$ is the temperature between the LAB and 660 *km* depth for the Tomography-Based Convection models, T_p is the mantle potential temperature with which we are experimenting, exp is the natural exponential equal to 2.718, g is the gravitational acceleration, α is the thermal expansivity, $z_{\text{depth} > \text{LAB}(i)}$ is the depth between LAB and 660 *km* at location *i*, C_p is the heat capacity, and δT is the temperature anomaly. The temperature and velocity boundary conditions for Tomography-Based Convection models are the same as those for Lithospheric Modulated Convection models, and the initial pressure conditions are also the same.

There are multiple models of shear wave velocity structures that encompass the East African Rift, but the majority of them focus on depths above 450 km (e.g., Celli et al., 2020; Fishwick et al., 2010; O'Donnell et al., 2013; Priestly et al., 2008; Wang et al., 2022; Weeraratne et al., 2003), whereas our study extends from the surface to 660 km depth to ensure minimal boundary effects with our convection simulations. The Emry et al. (2019) shear wave velocity model extends deeper than 450 km depth and captures upper mantle features in the study region. This model uses a checkerboard resolution test of 5 x 5 degrees, and the authors demonstrate this resolution is sufficient to resolve small-scale structures in the upper mantle. The Emry et al. (2019) method is robust for the region, revealing a broad slow shear wave velocity anomaly at the mantle transition zone in the Western Branch and a localized slow shear wave velocity anomaly beneath the Virunga volcanic province and along the Eastern Branch in the shallow

upper mantle (Figure 5) similar to other models. If another shear wave velocity model was used that did not resolve localized thermal anomalies in the upper mantle, our models would most likely fail to generate melt in those locations.

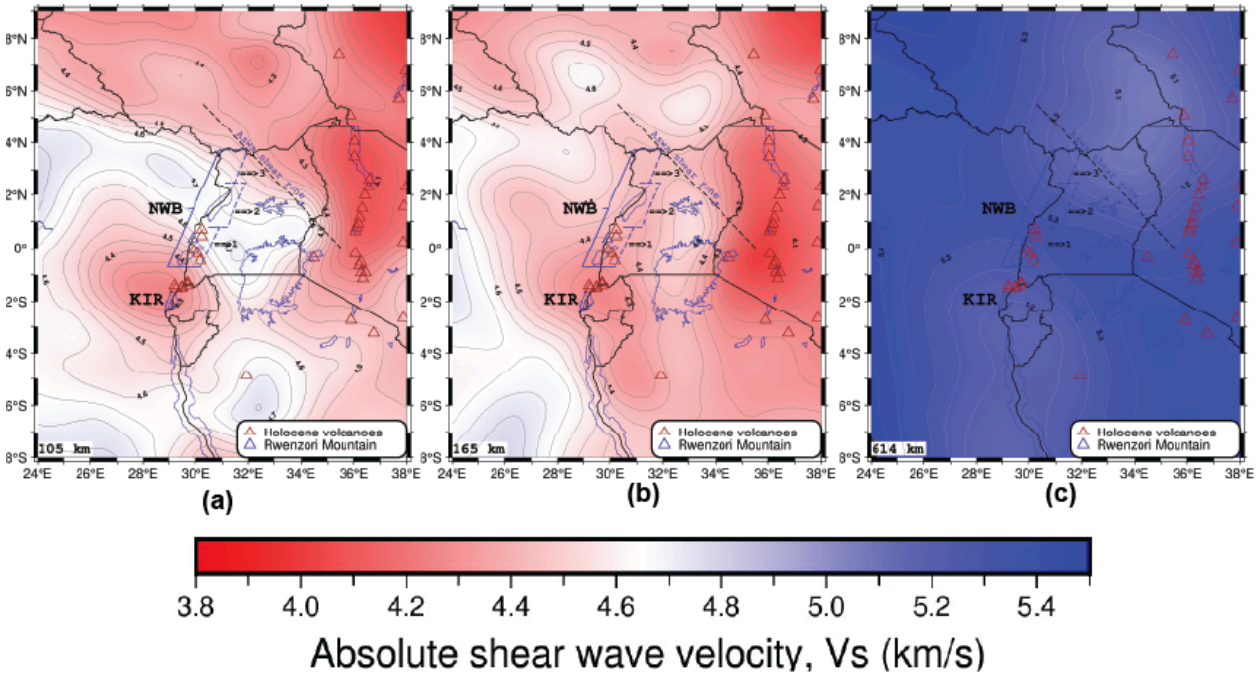

Figure 5: Key depth slices of absolute shear wave velocities beneath the study region obtained from the Emry et al. (2019) shear wave velocity model at a) 105 *km*, b)165 *km* and c) 614 *km*. The maps display gray contour intervals of absolute shear wave velocities at 0.05 km/s. KIR = Kivu Rift; NWB = Northern Western Branch; 1 = Lakes George-Edward graben; 2 = Albertine graben; 3 = Rhino graben

4.6.3. Lithospheric Thickness

We recognize that there are various definitions of the lithosphere, particularly its bottom boundary known as the Lithosphere-Asthenosphere Boundary (LAB) (Eaton et al. 2009; Fischer et al., 2010). In this study, we define the LAB as a thermomechanical boundary. Mechanically, the lithosphere is approximately rigid, and the sublithospheric mantle is governed by composite rheology (see Section 4.3). The thermal conditions of both the Lithospheric Modulated Convection and Tomography-Based Convection models are described in sections 4.6.1 and 4.6.2.

Both Lithospheric Modulated Convection and Tomography-Based Convection are constrained by the lithospheric thickness, and here we use the Afonso et al. (2022) lithospheric thickness model (Figure 4b), which we refer to as the Afonso model. We note that we have assessed two other lithospheric thickness models, the LITHO1.0 model (Pasyanos et al., 2014) and the regional Fishwick (2010, revised) (see supplementary material), and we choose the

Afonso model in this study because it uses a more robust dataset, a newer method, and resolves more variations in lithospheric topography beneath the region. For instance, various segments of the rift system such as the northern Western Branch, Kivu Rift, Tanganyika Rift, Malawi Rift, Main Ethiopian Rift, and Kenya Rift exhibit lower lithospheric thicknesses (80–120 *km*) compared to the Tanzanian Craton, which has a greater lithospheric thickness of 160 *km*, as anticipated. Within the study area, the shallowest lithosphere is found beneath the Kivu Rift (~90-100 km) and the Lake Edward-George Graben (~90-110 *km*), where Holocene volcanic fields such as the Virunga and Toro-Ankole fields are located. The Afonso model determines the LAB by integrating global and regional datasets, including Rayleigh-wave dispersion curves, absolute elevation, surface heat flow, upper mantle geoid anomalies, gravity anomalies, and gravity gradients. These datasets are jointly inverted using a thermodynamically constrained multi-observable probabilistic inversion method, specifically designed to estimate the physical state of the lithosphere, such as its temperature distribution. The model employs a spatial resolution ranging from 1° to 1.5°. During the inversion process, the authors calculate 1D steady-state conductive geotherms for each cell down to the LAB, defined as the depth to the 1250℃ isotherm (Afonso et al., 2022). In the northern Western Branch, the lithospheric thickness ranges from ~90 to ~120 *km*, with an average of 110 *km*. Specifically, the thickness is ~100 *km* beneath the Rhino Graben, ~100-120 *km* beneath the Albertine Graben, and ~90-110 *km* beneath the Lakes George-Edward Graben.

5. Results

Lithospheric Modulated Convection and Tomography Based Convection models were run using the ASPECT code for mantle potential temperatures (T_p) values of 1693, 1703, 1713, and 1723 K. Our ASPECT code input files were the lithospheric thicknesses beneath the study region defined by Afonso et al. (2022: Figure 4b), reference density and reference shear wave velocities defined by Kennett et al. (1995), and the shear wave velocities defined by Emry et al. (2019).

We show cross-sections of time-dependent Lithospheric Modulated Convection (Figures 6b-6d) and instantaneous Tomography-Based Convection with melt fractions (Figure 6a) across profile AB (Figure 4b). The Tomography-Based Convection model produces melt generation beneath the entire profile AB at depths starting just beneath the LAB and down to ~186 km (Figure 6a), whereas melt generation only occurs below the Kivu rift for the Lithospheric Modulated Convection at very shallow depths just beneath the LAB (~93-103 *km*) (Figures 6b & 6c).

Tables 2-3 and Figures 7-8 display the results of sublithospheric melt generation in terms of melt fractions (eq. 9) at specific depths from Lithospheric Modulated Convection and Tomography-Based Convection beneath the northern Western Branch and the Kivu Rift of the EARS. In this study, melt generation is produced beneath the Kivu rift and slightly under the magma-rich Lakes George-Edward graben with both Lithospheric Modulated Convection (i.e., depths ~93-103 *km*; Table 2 & Figure 7) and Tomography-Based Convection models (i.e., depths

~93-160 *km*; Table 3 & Figure 8). The Tomography-Based Convection model generates melt north and northeast of the Aswa shear zone beneath the Kenyan Rift that also extending southwards slightly beneath the Rhino graben at depths between ~108 and 139 *km* for T_p values of 1693, 1703, 1713, and 1723 K (Table 3 & Figure 8). We also observe a small amount of melt north of the Aswa shear zone with the Lithospheric Modulated Convection model (Figure 7). At deeper depths between ~160-186 *km*, we generate melt beneath both the magma-rich Lakes George-Edward graben and the magma-poor Albertine and Rhino grabens with the Tomography-Based Convection method (Table 3 and Figure 8).

The Lithospheric Modulated Convection model produces melt at a maximum depth of ~103 *km* (Table 2 and Figures 7), whereas the Tomography-Based Convection model generates melt up to ~186 *km* (Table 3). The Lithospheric Modulated Convection model generates lower melt fractions compared to the Tomography-Based Convection model, with a maximum melt fraction of 0.046 for T_p = 1723 K at ~93 km depth (Table 2 & Figures 7d-f). The maximum melt fraction for the Tomography-Based Convection model is 0.409 for T_p = 1723 K at ~98 km depth near the Virunga Volcanic Province (Table 3 & Figure 8d). The Lithospheric Modulated Convection model produces no sublithospheric melt at T_p values of 1693 and 1703 K beneath the entire northern Western Branch (Table 2). The Lithospheric Modulated Convection model generates its maximum melt fraction values at a model time of 174,528 years for T_p = 1693 K, 164,808 years for T_p = 1703 K, 157,273 years for T_p = 1713 K, and 151,125 years for T_p = 1723 K. The Tomography-Based Convection model is instantaneous, i.e., model time is 0, to be consistent with the present-day constraints from shear wave seismic velocities.

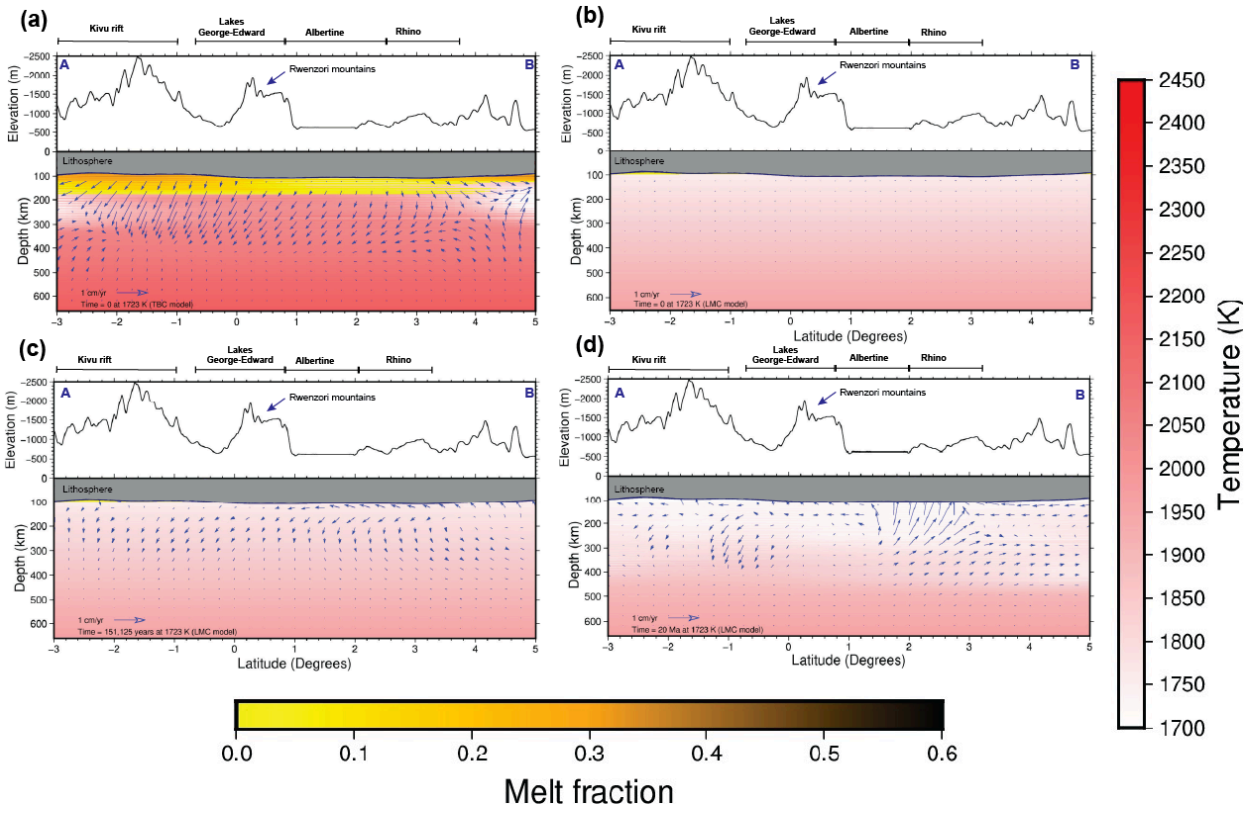

Figure 6: Profile showing time-dependent convection with melt fraction across the northern Western Branch (profile AB in Figure 4b); (a) Time = 0 at 1723 K for the Tomography-Based Convection model which is also described in Table 3, (b) Time = 0 at 1723 K for the Lithospheric Modulated Convection model, (c) Time = 151,125 years at 1723 K for the Lithospheric Modulated Convection model which is described in Table 2, and (d) Time = 20 Ma at 1723 K for the Lithospheric Modulated Convection model. Note that for the Lithospheric Modulated Convection models, melt is only present beneath the Kivu rift (Figures 6b & 6c).

Table 2: Maximum melt fractions generated at a given depth and mantle potential temperatures of 1693, 1703, 1713, and 1723 K beneath the segments of the northern Western Branch and the Kivu Rift for the Lithospheric Modulated Convection models. Note the vertical resolution of our mesh is 10.3 km, so our 93 km depth slice is still considered deep melt below the LAB. * - *indicates no melt is generated at that depth or part of the rift.*

Depth (*km*)	**Kivu Rift**				**Magma-rich region: Lakes George-Edward graben**				**Magma-poor region: Albertine graben**				**Magma-poor region: Rhino graben**			
	1693 K	**1703 K**	**1713 K**	**1723 K**	**1693 K**	**1703 K**	**1713 K**	**1723 K**	**1693 K**	**1703 K**	**1713 K**	**1723 K**	**1693 K**	**1703 K**	**1713 K**	**1723 K**
93	0.019	0.037	0.058	0.082	-	-	0.024	0.046	-	-	-	-	-	-	-	-
98	0.001	0.013	0.029	0.050	-	-	0.022	0.041	-	-	-	-	-	-	-	-

103	-	-	0.007	0.023	-	-	0.007	0.023	-	-	-	-	-	-	-	-

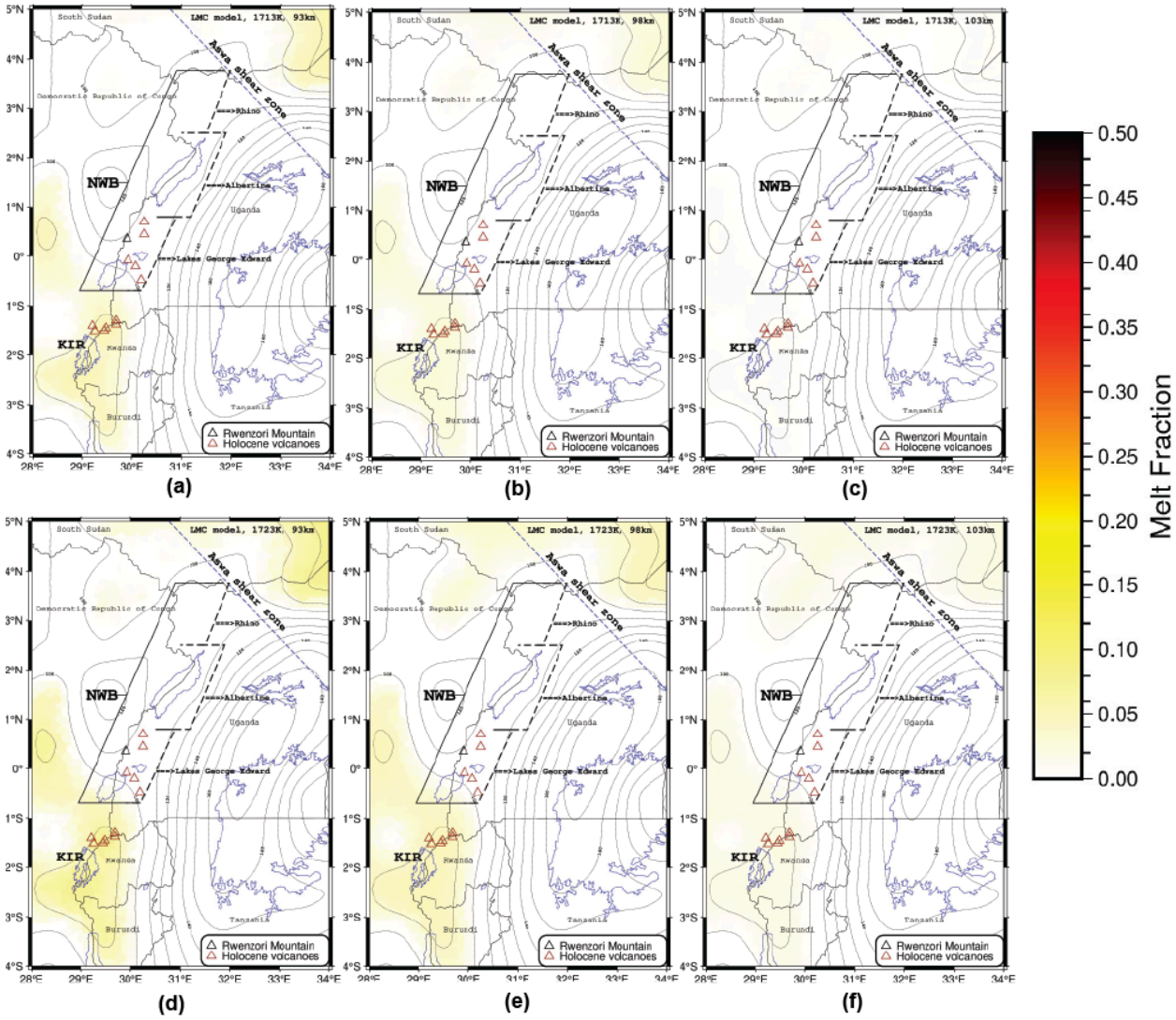

Figure 7: Maps showing the melt generated in terms of melt fractions using the Lithospheric Modulated Convection method at T_p of 1713 and 1723 K; a) T_p of 1713 K at 93 *km*, b) T_p of 1713 K at 98 *km*, c) T_p of 1713 K at 103 *km*, d) T_p of 1723 K at 93 *km*, e) T_p of 1723 K at 98 *km*, and f) T_p of 1723 K a 103 *km*. The Lithospheric Modulated Convection method only produces melt at depths of 93, 98, and 103 *km* with a T_p of 1713 and 1723 K beneath the northern Western Branch (labeled NWB on the map). The maps display contour intervals of lithospheric thickness at 10 *km*, indicated by dotted lines. We note that the melt produced in the northeast near the Kenya Rift and in the southwest around the Kivu Rift extends beyond the area shown on the map, but for this study, we focus mainly on our study region.

Table 3: Maximum melt fractions generated at a given depth and mantle potential temperatures of 1693, 1703, 1713, and 1723 K beneath the segments of the northern Western Branch and the Kivu Rift for the Tomography-Based Convection models. Note the vertical resolution of our mesh is 10.3 km, so our 93 km depth slice is still considered deep melt below the LAB. * - *indicates no melt is generated at that depth or part of the rift.*

Depth (*km*)	Kivu Rift				Magma-rich region: Lakes George-Edward graben				Magma-poor region: Albertine graben				Magma-poor region: Rhino graben			
	1693 K	1703 K	1713 K	1723 K	1693 K	1703 K	1713 K	1723 K	1693 K	1703 K	1713 K	1723 K	1693 K	1703 K	1713 K	1723 K
93	0.369	0.388	0.409	0.429	-	-	0.044	0.067	-	-	-	-	-	-	-	-
98	0.348	0.368	0.388	0.409	0.348	0.363	0.388	0.409	-	-	-	-	-	-	-	-
103	0.328	0.347	0.367	0.388	0.328	0.347	0.367	0.388	-	-	-	-	-	-	-	-
108	0.308	0.327	0.346	0.367	0.308	0.327	0.346	0.367	-	-	-	-	0.198	0.206	0.216	0.228
113	0.288	0.306	0.326	0.346	0.288	0.306	0.326	0.346	-	-	-	-	0.181	0.193	0.199	0.209
114	0.288	0.306	0.326	0.346	0.288	0.306	0.326	0.346	-	-	-	-	0.181	0.193	0.199	0.209
119	0.268	0.286	0.305	0.326	0.269	0.286	0.305	0.326	-	-	-	-	0.126	0.163	0.188	0.194
124	0.249	0.267	0.285	0.305	0.250	0.267	0.285	0.305	-	-	-	-	0.073	0.106	0.143	0.183
129	0.231	0.248	0.266	0.285	0.232	0.248	0.266	0.285	-	-	-	-	-	0.050	0.086	0.122
134	0.214	0.229	0.246	0.265	0.214	0.229	0.246	0.265	-	-	-	-	-	-	0.040	0.070
139	0.198	0.212	0.228	0.246	0.198	0.212	0.228	0.246	-	-	-	-	-	-	-	0.028
144	0.184	0.196	0.210	0.227	0.184	0.196	0.210	0.227	-	-	-	-	-	-	-	-
145	0.184	0.19	0.210	0.227	0.184	0.196	0.210	0.227	-	-	-	-	-	-	-	-
149	0.173	0.182	0.194	0.209	0.173	0.182	0.194	0.209	-	-	-	-	-	-	-	-
150	0.173	0.182	0.194	0.209	0.173	0.182	0.194	0.209	-	-	-	-	-	-	-	-

155	0.153	0.170	0.180	0.193	0.153	0.170	0.180	0.192	-	-	-	-	-	-	-	-
160	0.105	0.152	0.168	0.178	0.105	0.152	0.168	0.178	-	-	-	0.031	-	-	-	-
165	0.062	0.103	0.152	0.166	0.062	0.103	0.152	0.166	-	0.048	0.087	0.132	-	-	-	-
170	0.026	0.060	0.103	0.154	0.026	0.060	0.103	0.154	0.026	0.060	0.103	0.153	-	-	-	-
175	0.002	0.024	0.060	0.104	-	0.024	0.060	0.104	-	0.024	0.059	0.104	-	-	0.023	0.059
180	-	0.001	0.023	0.060	-	-	0.023	0.060	-	-	0.023	0.060	-	-	0.023	0.060
181	-	0.001	0.023	0.060	-	-	0.023	0.060	-	-	0.023	0.060	-	-	-	0.060
186	-	-	0.001	0.024	-	-	-	0.024	-	-	-	0.024	-	-	-	0.024

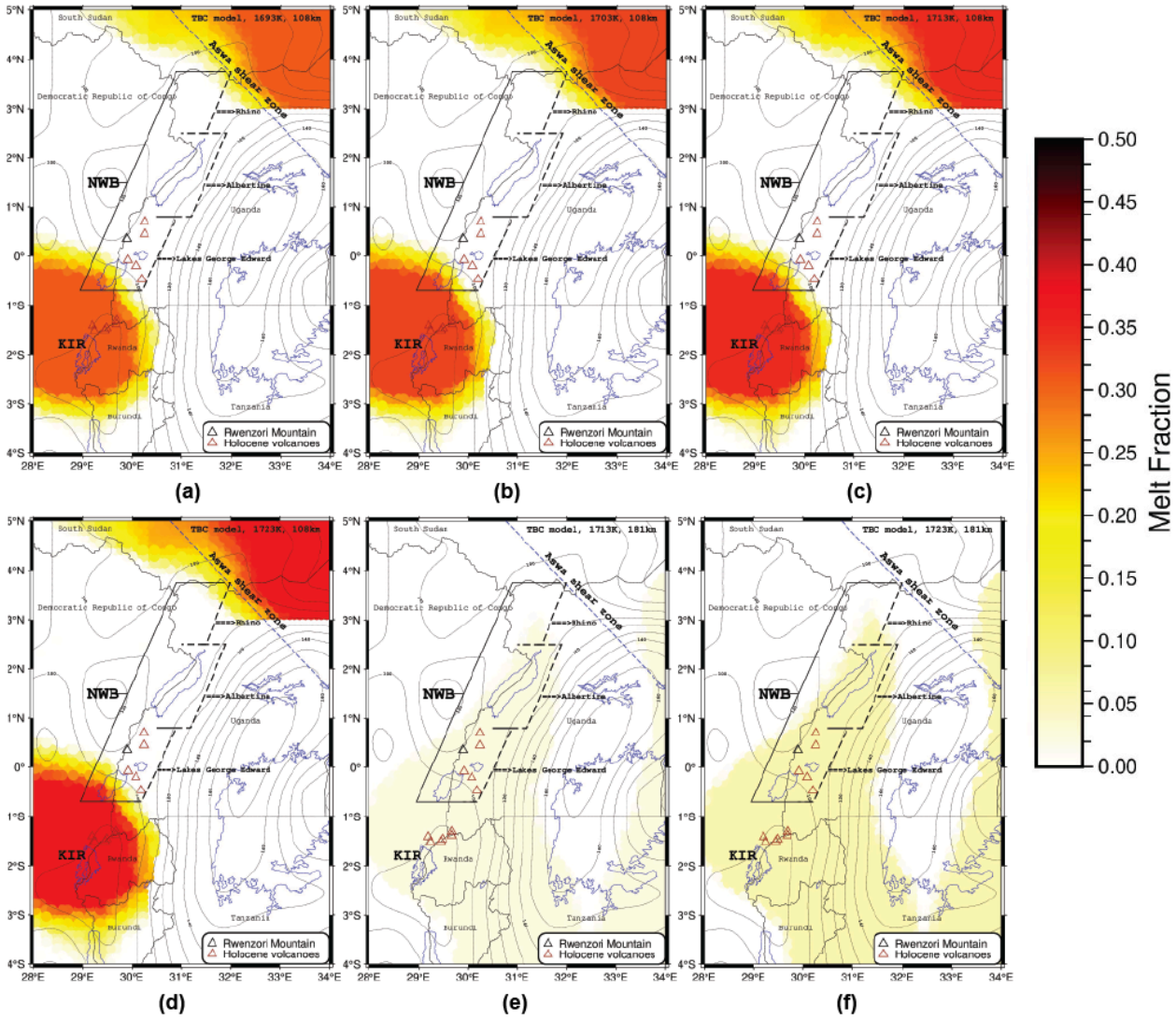

Figure 8: Maps showing the melt generated in terms of melt fractions using the Tomography-Based Convection method at 108 *km* depth for T_p values of a) 1693, b) 1703, c) 1713, and d) 1723 K. e) map showing the melt generated in terms of melt fractions using the Tomography-Based Convection method at 181 *km* depth at T_p 1713 and f) 1723 K. We note that the melt produced in the northeast near the Kenya Rift and in the southwest around the Kivu Rift extends beyond the area shown on the map, but for this study, we focus mainly on our study region.

6. Discussion

The study uses 3D geodynamic numerical modeling with the code ASPECT to investigate the presence of deep melt (sublithospheric melt) from two small-scale convection processes, Lithospheric Modulated Convection and Tomography-Based Convection, and its possible contribution to rifting processes in the northern Western Branch. We use mantle potential temperatures of 1693, 1703, 1713, and 1723 K (Rooney et al., 2012; 2020) to constrain the initial

temperature conditions at the LAB for each model (see Section 4.6) and assess for the presence of deep melt beneath the northern Western Branch.

While our findings suggest melt can be generated from both Lithospheric Modulated Convection and Tomography-Based Convection models, we consider melt generated with the Tomography-Based Convection model to be the best representation because the study region has complex, highly varying lithospheric thickness (e.g., Afonso et al., 2022) as well as variations in thermal anomalies inferred from seismic shear wave velocities (e.g., Celli et al., 2020; Emry et al., 2019; Fishwick et al., 2010; O'Donnell et al., 2013; Priestly et al., 2008; Wang et al., 2022; Weeraratne et al., 2003). We tested melt generation from Lithospheric Modulated Convection as a starting model because of the large variations in lithospheric topography beneath the study region (i.e., Figure 4b: Afonso et al., 2022), but we loosely interpret results from this approach since the method is too simplistic for our region.

6.1 Deep Melt Beneath the Northern Western Branch

Our study indicates melt generation beneath the magma-rich Lakes George-Edward graben with both Tomography-Based Convection (Table 3 & Figure 8) and Lithospheric Modulated Convection models (Table 2 & Figure 7) at depths just below the LAB, but we interpret these results to be associated with melt that has been transported from beneath the Kivu Rift rather than being generated directly beneath the magma-rich Lakes George-Edward graben (particularly at depths shallower than 160 km). Numerous previous seismic studies have resolved low seismic velocity anomalies beneath the Kivu Rift, but not necessarily beneath the Lakes George-Edward graben (e.g., Celli et al., 2020; Emry et al., 2019; Fishwick et al., 2010; O'Donnell et al., 2013; Priestley et al., 2008; 2014; van Herwaarden et al., 2020; Wang et al., 2022; Weeraratne et al., 2003). In addition, Mount Nyiragongo and Nyamuragira, the two most active volcanoes in the Western Branch of the EARS, located in the Virunga volcanic area of the Kivu Rift (Global Volcanism Program, 2013), indicate the presence of ample deep melt that sources their multi-teired magmatic plumbing system (i.e., Ji et al., 2017; Kaleghetso et al., 2025; Molendijk et al., 2024; Wauthier et al., 2013).

At the northern periphery of our region between the Rhino graben and Aswa shear zone at depths between 108 and 139 km, we find deep melt generation with the Tomography-Based Convection model (Table 3 and Figure 8). We suggest this melt is associated with the transported deep melt that originates beneath the Kenyan Rift. Several previous seismic studies suggest widespread thermal anomalies are beneath the Kenya Rift (e.g., Celli et al., 2020; Emry et al., 2019; Fishwick et al., 2010; O'Donnell et al., 2013; Priestly et al., 2008; van Herwaarden et al., 2020; Wang et al., 2022; Weeraratne et al., 2003). Furthermore, isotopic studies (e.g., Furman et al., 2004; Meshesha & Shinjo, 2008; Rogers et al., 2000) have inferred a mantle plume beneath the Kenya Rift, about 400 km east of the Rhino graben, that could transport high-temperature, melt-generating plume materials towards the Rhino graben in the region where our models suggest the presence of deep melt. Geodynamic investigations also support the model of plume

materials migrating away from the Kenya Rift towards the Western Branch (i.e., Koptev et al., 2015; 2018).

We do not see any melt generated beneath the Toro-Ankole volcanic province in southwestern Uganda at depths shallower than 160 km in our models (see Tables 2-3 and Figures 7-8) despite the presence of volcanoes in this region i.e., Fort Portal, Kyatwa, Katwe-Kikorongo, Bunyaruguru, Katunga, Bufumbira, and Muhavura volcanoes (Figure 2; Global Volcanism Program, 2013). This result suggests that the volcanic activity in the Toro-Ankole volcanic province could have been sourced by deep melt migrating northwards from the Kivu Rift along the LAB as porous flow, like in spreading ridge regions (e.g., Morgan, 1987), or through tensile dike propagation (e.g., Pouclet & Bram, 2021; Wauthier et al., 2015). Fault lineaments observed north of Lake Kivu and south of Lake Edward could have influenced melt migration and distribution of volcanic activity in the Toro-Ankole volcanic province in southwestern Uganda (e.g., Smets et al., 2016). Furthermore, various isotopic studies reveal a lithospheric mantle source with different melt types due to the depth of melting that is responsible for supplying melt to volcanoes in the Virunga and Toro-Ankole Provinces (Furman & Graham, 1999; Rogers et al., 1992, 1998; Rooney, 2020; Rosenthal et al., 2009). Lithospheric delamination was proposed as a possible mechanism for the extreme uplift of the Rwenzori Mountains, resulting from the upwelling asthenosphere around the Rwenzori Mountains (Wallner & Schmeling, 2010) that could generate decompression melting at the base the LAB in that region that generates thermal weakening. Furman et al. (2016) proposed drip melting within the region, where the metasomatized lithosphere with a pyroxenite component drips into the asthenosphere causing lithospheric removal, decompression melting, and thermal weakening of the lithospheric. Our findings, however, indicate that melt generated beneath the Rwenzori Mountains region is between 160-186 km, which is substantially deeper than the LAB. Deep melt that would be associated with lithospheric delamination and drip melting around the Rwenzori Mountains could, instead, originate from melt migrating northwards from beneath the Kivu Rift.

The Tomography-Based Convection method produces deep melt beneath the magma-rich Lakes George-Edward graben and the magma-poor Albertine and Rhino grabens at deeper depths between 160-186 km (Table 3 and Figure 8e-f). This melt is most likely originating directly beneath the northern Western Branch rather than having migrated from elsewhere since the depths of the melt are so deep. Melt generated at depth 160-186 km in our models is unlikely to contribute to rifting beneath the northern Western Branch since it is deep within the asthenosphere and unlikely to contribute to thermal weakening of the lithospheric mantle.

The strong melt generation gradient observed in our models between 160-186 km surrounding the Tanzania craton (Figure 8e-f) is supported by recent thermochemical and tomographic models by Afonso et al. (2022) that suggest a hot upwelling beneath the Tanzanian craton impinges on the LAB and diverts along the craton's boundaries focusing shallow decompression melting along the Western and Eastern branches of the East African Rift System. The decompression melting would thermally weaken the base of the lithosphere in these regions, thus helping the system overcome the tectonic force paradox.

Given that our models indicate deep melt is present just below the lithosphere in several parts of the Western branch and that deep melt would aid in thermal weakening of the lithospheric mantle, our results suggest deep melt likely contributes to magma-poor rifting in the northern Western Branch of the East African Rift System.

6.2 Comparisons with Deep Melt Production in Other Regions

In this section, we compare our melt fraction values with those from other settings based on geodynamic modeling or experimental studies. Perhaps the most similar setting to the northern Western Branch is the magma-poor Malawi Rift, which is also part of the East African Rift System and encompasses the Rungwe Volcanic Province. Using a Lithospheric Modulated Convection model, Njinju et al. (2021) estimated melt fractions of 0.015 at ~150 km depth beneath the Rungwe Volcanic Province with lithospheric thickness modeled at ~100 km from Fishwick (2010). We do not have any comparable melt fraction values for our Lithospheric Modulated Convection model beneath our study region (Table 2). The values from Njinju et al. (2021) are lower and at shallower depths beneath the southern portion of our region where a similar style of volcanism is present in the Kivu Rift. With a more realistic initial temperature condition constrained by seismic shear wave velocities, Njinju et al. (2023) used Tomography-Based Convection and melt generation for the Malawi Rift. They found slightly higher melt fractions of 0.08 at ~130 km depth beneath the Rungwe Volcanic Province, which is about 30 km beneath the LAB in this area. The value of melt fraction found by Njinju et al. (2023) with Tomography-Based Convection is similar to values found in this work at depths between ~165-175 km beneath the Lakes George-Edwards graben and Albertine Rift (Table 3). In mid-oceanic ridge settings, experimental studies that leverage batch melting by Kushiro (1996) find melt fraction values up to 0.4 at ~45 km for experiments at 1723 K, which is comparable to some of our highest values of melt fractions at our shallowest depths of ~93 km and T_p values of 1713 and 1723 K. In other extensional settings, such as the Deccan Traps, one of the world's largest volcanic provinces that peaked in eruptions ~65-66 My, studies of melt fractions indicate values of 0.15-0.30 sourced from depths of ~60-100 km fed these volcanoes (Sen, 2001). The Hump area in East Pacific Rise experiences melt fractions ranging from 0.14-0.22 with melting starting around 61-78 km depth in the upper mantle (Niu et al. 1996). These examples demonstrate the reasonability of our modeled results both in terms of the depth of melt and the amount of melt fractions.

6.3 Limitations of the Modeling Approaches and Future Work

The study used both Lithospheric Modulated Convection and Tomography-Based Convection modeling approaches to simulate small-scale mantle convection as well as deep melt generation. In the Tomography-Based Convection model, we added a temperature anomaly to the reference temperature profile of the upper mantle based on an African-centric seismic shear wave velocity model (Emry et al., 2019). However, it is important to acknowledge potential limitations with these numerical approaches. For example, with the Tomography-Based Convection models, we run instantaneous models that provide an instantaneous description of

present-day upper mantle convection rather than its evolution, which may be a limitation of tomography-based models since tomography itself is a snapshot of the present-day seismic structure of the mantle (Glišović et al., 2012).

In this study, we employed batch melting to model deep melt generation below the LAB, and this approach yielded substantial melt fractions, particularly at shallow depths just below the LAB. Subsequent work could explore alternative types of melting, i.e., fractional melting, critical melting, or incremental melting, as well as the effects of melt migration into the mantle lithosphere. We also have a coarse estimation of the mantle potential temperatures beneath the northern Western Branch from Rooney et al. (2012). Future work could consider using better constrained mantle potential temperatures, which are crucial for our initial temperature conditions. These alternative approaches could provide further insights and enhance our understanding of the role of melt during extensional processes in the northern Western Branch of the EARS.

In our study, we used the Afonso lithospheric thickness model (Afonso et al., 2022), which is a regional model. Future work could consider exploring alternative, better constrained lithospheric thickness models as they become available to further enhance our understanding of this study area.

7. Conclusions

In this contribution, we utilize the 3D finite element code ASPECT to model mantle convection and sublithospheric melt generation (deep melt) beneath the northern Western Branch of the EARS that results from Lithospheric Modulated Convection and Tomography-Based Convection. Our study suggests that deep melt from the Kivu Rift and Kenyan Rift could be migrating towards the northern Western Branch, contributing to rifting by thermally weakening the base of the lithosphere. Our models also indicate that deep melt from small-scale convection is generated directly beneath the northern Western Branch at depths of 160 to 186 km, but this melt is too deep to support thermal weakening of the lithosphere. Given that deep melt is present beneath several regions along the Western branch near the LAB, our study supports that deep melt contributes to rifting in the northern Western Branch of the East African Rift System by thermally weakening the lithosphere. These findings contribute to an improved understanding of the geodynamic processes acting to extend the northern Western Branch.

8. Open Research

To obtain the lithospheric thickness of the northern Western Branch, we downloaded the Afonso model from Afonso et al. (2022). Next, we converted the files to longitude (radians), colatitude (radians), and thickness (meters) for input into ASPECT. We also interpolate the models to 0.01° using bicubic Bessel splines to obtain a consistent grid for our model domain area described in section 4.5. The ASPECT code and modified initial temperature, initial composition, and material models used in this paper are available open access through Zenodo at Kwagalakwe et al. (2024).

9. References

- Adams, A., Nyblade, A., & Weeraratne, D. (2012). Upper mantle shear wave velocity structure beneath the East African plateau: evidence for a deep, plateauwide low velocity anomaly. Geophysical Journal International, 189(1), 123-142.
- Adobe Inc. (2019). Adobe Illustrator. Retrieved from https://adobe.com/products/illustrator
- Afonso, Juan (2022). Afonso_Africa_2022_Nat_Geosci.zip. figshare [Dataset]. https://doi.org/10.6084/m9.figshare.19322180.v1
- Afonso, J. C., Ben-Mansour, W., O'Reilly, S. Y., Griffin, W. L., Salajegheh, F., Foley, S., & Yang, Y. (2022). Thermochemical structure and evolution of the cratonic lithosphere in central and southern Africa. Nature Geoscience, 15(5), 405-410.
- Ajala, R., Kolawole, F., & Menke, W. (2024). Blind magmatism abets nonvolcanic continental rifting. Communications Earth & Environment, 5(1), 80.
- Albaric, J., Déverchère, J., Perrot, J., Jakovlev, A., & Deschamps, A. (2014). Deep crustal earthquakes in North Tanzania, East Africa: Interplay between tectonic and magmatic processes in an incipient rift. Geochemistry, Geophysics, Geosystems, 15(2), 374-394.
- Artyushkov, E. V. (1973). Stresses in the lithosphere caused by crustal thickness inhomogeneities. Journal of Geophysical Research, 78(32), 7675-7708.
- Aulbach, S., Rudnick, R. L., & McDonough, W. F. (2008). Li-Sr-Nd isotope signatures of the plume and cratonic lithospheric mantle beneath the margin of the rifted Tanzanian craton (Labait). Contributions to mineralogy and Petrology, 155(1), 79-92.
- Ballard, S., Pollack, H. N., & Skinner, N. J. (1987). Terrestrial heat flow in Botswana and Namibia. Journal of Geophysical Research: Solid Earth, 92(B7), 6291-6300.
- Bangerth, W., Dannberg, J., Gassmöller, R., & Heister, T. (2018). ASPECT: Advanced solver for problems in Earth's ConvecTion, user manual.
- Barker, D. S., & Nixon, P. H. (1989). High-Ca, low-alkali carbonatite volcanism at Fort Portal, Uganda. Contributions to Mineralogy and Petrology, 103, 166-177.
- Barry, P. H., Hilton, D. R., Fischer, T. P., De Moor, J. M., Mangasini, F., & Ramirez, C. (2013). Helium and carbon isotope systematics of cold "mazuku" CO2 vents and hydrothermal gases and fluids from Rungwe Volcanic Province, southern Tanzania. Chemical Geology, 339, 141-156.
- Bastow, I. D., Nyblade, A. A., Stuart, G. W., Rooney, T. O., & Benoit, M. H. (2008). Upper mantle seismic structure beneath the Ethiopian hot spot: Rifting at the edge of the African low‐velocity anomaly. Geochemistry, Geophysics, Geosystems, 9(12).
- Bauer, F. U., Glasmacher, U. A., Ring, U., Karl, M., Schumann, A., & Nagudi, B. (2013). Tracing the exhumation history of the Rwenzori Mountains, Albertine Rift, Uganda, using low temperature thermochronology. Tectonophysics, 599, 8-28.
- Bauer, F. U., Glasmacher, U. A., Ring, U., Schumann, A., & Nagudi, B. (2010). Thermal and exhumation history of the central Rwenzori Mountains, Western rift of the east African rift system, Uganda. International Journal of Earth Sciences, 99(7), 1575-1597.

- Begg, G. C., Griffin, W. L., Natapov, L. M., O'Reilly, S. Y., Grand, S. P., O'Neill, C. J., ... & Bowden, P. (2009). The lithospheric architecture of Africa: Seismic tomography, mantle petrology, and tectonic evolution. Geosphere, 5(1), 23-50.
- Brune, S., Kolawole, F., Olive, J. A., Stamps, D. S., Buck, W. R., Buiter, S. J., ... & Shillington, D. J. (2023). Geodynamics of continental rift initiation and evolution. Nature Reviews Earth & Environment, 4(4), 235-253.
- Buck, W. R. (1991). Modes of continental lithospheric extension. Journal of Geophysical Research: Solid Earth, 96(B12), 20161-20178.
- Buck, W. R. (2006). The role of magma in the development of the Afro-Arabian Rift System. Geological Society, London, Special Publications, 259(1), 43-54.
- Bwambale, B., Bagampadde, U., Gidudu, A., & Martini, F. (2015). Seismic hazard analysis for the Albertine region, Uganda–a probabilistic approach. South African Journal of Geology, 118(4), 411-424.
- Celli, N. L., Lebedev, S., Schaeffer, A. J., Ravenna, M., & Gaina, C. (2020). The upper mantle beneath the South Atlantic Ocean, South America and Africa from waveform tomography with massive data sets. Geophysical Journal International, 221(1), 178-204.
- Childs, H., Brugger, E., Whitlock, B., Meredith, J., Ahern, S., Pugmire, D., ... & Navrátil, P. (2012). VisIt: An end-user tool for visualizing and analyzing very large data.
- Coblentz, D. D., Richardson, R. M., & Sandiford, M. (1994). On the gravitational potential of the Earth's lithosphere. Tectonics, 13(4), 929-945.
- Combe, A. D., & Holmes, A. (1947). XIV. The Kalsilite-bearing Lavas of Kabirenge and Lyakauli, South-West Uganda. Earth and Environmental Science Transactions of The Royal Society of Edinburgh, 61(2), 359-379.
- Corti, G. (2009). Continental rift evolution: from rift initiation to incipient break-up in the Main Ethiopian Rift, East Africa. Earth-science reviews, 96(1-2), 1-53.
- Craig, T. J., Jackson, J. A., Priestley, K., & McKenzie, D. (2011). Earthquake distribution patterns in Africa: their relationship to variations in lithospheric and geological structure, and their rheological implications. Geophysical Journal International, 185(1), 403-434.
- Dannberg, J., & Heister, T. (2016). Compressible magma/mantle dynamics: 3-D, adaptive simulations in ASPECT. Geophysical Journal International, 207(3), 1343-1366.
- Dunbar, J. A., & Sawyer, D. S. (1988). Continental rifting at pre-existing lithospheric weaknesses. Nature, 333(6172), 450-452.
- Dziewonski, A. M., & Anderson, D. L. (1981). Preliminary reference Earth model. Physics of the earth and planetary interiors, 25(4), 297-356.
- Eaton, D. W., Darbyshire, F., Evans, R. L., Grütter, H., Jones, A. G., & Yuan, X. (2009). The elusive lithosphere–asthenosphere boundary (LAB) beneath cratons. Lithos, 109(1-2), 1-22.
- Ebinger, C. J. (1989). Tectonic development of the western branch of the East African rift system. Geological Society of America Bulletin, 101(7), 885-903.

- Ebinger, C. J., & Sleep, N. H. (1998). Cenozoic magmatism throughout east Africa resulting from impact of a single plume. Nature, 395(6704), 788-791.
- Ebinger, C. J., Oliva, S. J., Pham, T. Q., Peterson, K., Chindandali, P., Illsley‐Kemp, F., & Mulibo, G. (2019). Kinematics of active deformation in the Malawi rift and Rungwe Volcanic Province, Africa. Geochemistry, Geophysics, Geosystems, 20(8), 3928-3951.
- Ebinger, C. J., Yemane, T., Woldegabriel, G., Aronson, J. L., & Walter, R. C. (1993). Late Eocene–Recent volcanism and faulting in the southern main Ethiopian rift. Journal of the Geological Society, 150(1), 99-108.
- Emry, E. L., Shen, Y., Nyblade, A. A., Flinders, A., & Bao, X. (2019). Upper mantle Earth structure in Africa from full‐wave ambient noise tomography. Geochemistry, Geophysics, Geosystems, 20(1), 120-147.
- Ennih, N., & Liégeois, J. P. (2008). The boundaries of the West African craton, with special reference to the basement of the Moroccan metacratonic Anti-Atlas belt. Geological Society, London, Special Publications, 297(1), 1-17.
- Evans, R. L., Elsenbeck, J., Zhu, J., Abdelsalam, M. G., Sarafian, E., Mutamina, D., & Jones, A. G. (2019). Structure of the lithosphere beneath the Barotse Basin, western Zambia, from magnetotelluric data. Tectonics, 38(2), 666-686.
- Fadaie, K. T., & Ranalli, G. (1990). Rheology of the lithosphere in the East African Rift System. Geophysical Journal International, 102(2), 445-453.
- Fadel, I., Paulssen, H., van der Meijde, M., Kwadiba, M., Ntibinyane, O., Nyblade, A., & Durrheim, R. (2020). Crustal and upper mantle shear wave velocity structure of Botswana: The 3 April 2017 central Botswana earthquake linked to the East African Rift System. Geophysical Research Letters, 47(4), e2019GL085598.
- Fairhead, J. D. (1976). The structure of the lithosphere beneath the Eastern Rift, East Africa, deduced from gravity studies. Tectonophysics, 30(3-4), 269-298.
- Fischer, K. M., Ford, H. A., Abt, D. L., & Rychert, C. A. (2010). The lithosphere-asthenosphere boundary. Annual Review of Earth and Planetary Sciences, 38, 551-575.
- Fishwick, S. (2010). Surface wave tomography: imaging of the lithosphere–asthenosphere boundary beneath central and southern Africa?. Lithos, 120(1-2), 63-73.
- Forsyth, D., & Uyeda, S. (1975). On the relative importance of the driving forces of plate motion. Geophysical Journal International, 43(1), 163-200.
- Furman, T., Bryce, J. G., Karson, J., & Iotti, A. (2004). East African Rift System (EARS) plume structure: insights from Quaternary mafic lavas of Turkana, Kenya. Journal of Petrology, 45(5), 1069-1088.

- Furman, T., Bryce, J. G., Karson, J., & Iotti, A. (2004). East African Rift System (EARS) plume structure: insights from Quaternary mafic lavas of Turkana, Kenya. Journal of Petrology, 45(5), 1069-1088.

- Furman, T., & Graham, D. (1999). Erosion of lithospheric mantle beneath the East African Rift system: geochemical evidence from the Kivu volcanic province. In Developments in Geotectonics (Vol. 24, pp. 237-262). Elsevier.
- Furman, T., Nelson, W. R., & Elkins-Tanton, L. T. (2016). Evolution of the East African rift: Drip magmatism, lithospheric thinning and mafic volcanism. Geochimica et Cosmochimica Acta, 185, 418-434.
- Ghosh, A., & Holt, W. E. (2012). Plate motions and stresses from global dynamicn models. Science, 335(6070), 838-843.
- Girdler, R. W., & McConnell, D. A. (1994). The 1990 to 1991 Sudan earthquake sequence and the extent of the East African Rift System. Science, 264(5155), 67-70
- Glerum, A., Thieulot, C., Fraters, M., Blom, C., & Spakman, W. (2018). Nonlinear viscoplasticity in ASPECT: benchmarking and applications to subduction. Solid Earth, 9(2), 267-294.
- Glišović, P., Forte, A. M., & Moucha, R. (2012). Time-dependent convection models of mantle thermal structure constrained by seismic tomography and geodynamics: implications for mantle plume dynamics and CMB heat flux. Geophysical Journal International, 190(2), 785-815.
- Global Volcanism Program, 2013. Volcanoes of the World, v. 4.11.2. Venzke, E (ed.). Smithsonian Institution. Downloaded 01 Oct 2022.
- Google Earth 7.3.6.9796 (2001) Uganda, 1°22'05"N, 32°18'11"E, elevation 1,111m [online]. Available from: https://earth.google.com/web/ [accessed April 29, 2024]
- Grant, C., Kolawole, F., & Williams, J. (2024). Evolution of rift faulting in incipient, magma-poor divergent plate boundaries: New insights from the Okavango-Makgadikgadi Rift Zone, Botswana. Earth and Planetary Science Letters, 646, 118957.
- Gummert, M., Lindenfeld, M., Wölbern, I., Rümpker, G., Celestin, K., & Batte, A. (2016). Crustal structure and high-resolution Moho topography across the Rwenzori region (Albertine rift) from P-receiver functions. Geological Society, London, Special Publications, 420(1), 69-82.
- Halldórsson, S. A., Hilton, D. R., Scarsi, P., Abebe, T., & Hopp, J. (2014). A common mantle plume source beneath the entire East African Rift System revealed by coupled helium‐neon systematics. Geophysical Research Letters, 41(7), 2304-2311.
- Hansen, S. E., & Nyblade, A. A. (2013). The deep seismic structure of the Ethiopia/Afar hotspot and the African superplume. Geophysical Journal International, 194(1), 118-124.
- Hartnady, C. J. H. (2002). Earthquake hazard in Africa: perspectives on the Nubia-Somalia boundary: news and view. South African journal of science, 98(9), 425-428.
- Henderson, A. (2007). ParaView Guide: A Parallel Visualization Application. Kitware, Inc., Clifton Park, NY.

- Hilton, D.R., Halldórsson, S.A., Barry, P.H., Fischer, T.P., De Moor, J.M., Ramirez, C.J., Mangasini, F. and Scarsi, P., 2011. Helium isotopes at Rungwe Volcanic Province, Tanzania, and the origin of East African plateaux. Geophysical Research Letters, 38(21).
- Hodgson, I., Illsley‐Kemp, F., Gallacher, R. J., Keir, D., Ebinger, C. J., & Mtelela, K. (2017). Crustal structure at a young continental rift: A receiver function study from the Tanganyika Rift. Tectonics, 36(12), 2806-2822.
- Jackson, J. A., & White, N. J. (1989). Normal faulting in the upper continental crust: observations from regions of active extension. Journal of structural geology, 11(1-2), 15-36.
- Jadamec, M. A., & Billen, M. I. (2010). Reconciling surface plate motions with rapid three-dimensional mantle flow around a slab edge. Nature, 465(7296), 338–341.
- Jarvis, G. T., & Mckenzie, D. P. (1980). Convection in a compressible fluid with infinite Prandtl number. Journal of Fluid Mechanics, 96(3), 515-583.
- Jessell, M. W., Begg, G. C., & Miller, M. S. (2016). The geophysical signatures of the West African Craton. Precambrian Research, 274, 3-24.
- Ji, K. H., Stamps, D. S., Geirsson, H., Mashagiro, N., Syauswa, M., Kafudu, B., & d'Oreye, N. (2017). Deep magma accumulation at Nyamulagira volcano in 2011 detected by GNSS observations. Journal of African Earth Sciences, 134, 824-830.
- Jones, J. R., Stamps, D. S., Wauthier, C., Saria, E., & Biggs, J. (2019). Evidence for slip on a border fault triggered by magmatic processes in an immature continental rift. Geochemistry, Geophysics, Geosystems, 20(5), 2515-2530.
- Kaleghetso, E. K., Namur, O., Smets, B., Vander Auwera, J., Lubala, F., Van Gerve, T., & Molendijk, S. M. (2025). Magmatic differentiation and plumbing system beneath Nyamulagira volcano (Virunga Volcanic Province, East African Rift). Journal of Volcanology and Geothermal Research, 458, 108264.
- Karato, S. and Wu, P.: Rheology of the Upper Mantle: A Synthesis, Science, 260, 771–778, 1993.
- Karato, S. I., & Wu, P. (1993). Rheology of the upper mantle: A synthesis. Science, 260(5109), 771-778.
- Karato, S.: Deformation of Earth Materials: An Introduction to the Rheology of Solid Earth, Cambridge University Press, 2008.
- Katumwehe, A. B., Abdelsalam, M. G., & Atekwana, E. A. (2015). The role of pre-existing Precambrian structures in rift evolution: The Albertine and Rhino grabens, Uganda. Tectonophysics, 646, 117-129.
- Katumwehe, A. B., Abdelsalam, M. G., Atekwana, E. A., & Laó-Dávila, D. A. (2016). Extent, kinematics and tectonic origin of the Precambrian Aswa Shear Zone in eastern Africa. Gondwana Research, 34, 241-253.
- Katz, R. F., Spiegelman, M., & Langmuir, C. H. (2003). A new parameterization of hydrous mantle melting. Geochemistry, Geophysics, Geosystems, 4(9).

- Kennett, B. L., Engdahl, E. R., & Buland, R. (1995). Constraints on seismic velocities in the Earth from traveltimes. Geophysical Journal International, 122(1), 108-124.
- King, S. D., & Anderson, D. L. (1998). Edge-driven convection. Earth and Planetary Science Letters, 160(3-4), 289-296.
- Koptev, A., Burov, E., Calais, E., Leroy, S., Gerya, T., Guillou-Frottier, L., & Cloetingh, S. (2016). Contrasted continental rifting via plume-craton interaction: Applications to Central East African Rift. Geoscience Frontiers, 7(2), 221-236.
- Koptev, A., Calais, E., Burov, E., Leroy, S., & Gerya, T. (2018). Along‐axis variations of rift width in a coupled lithosphere‐mantle system, Application to East Africa. Geophysical Research Letters, 45(11), 5362-5370.
- Koptev, A., Calais, E., Burov, E., Leroy, S., & Gerya, T. (2015). Dual continental rift systems generated by plume–lithosphere interaction. Nature Geoscience, 8(5), 388-392.
- Kronbichler, M., Heister, T., & Bangerth, W. (2012). High accuracy mantle convection simulation through modern numerical methods. Geophysical Journal International, 191(1), 12-29.
- Kushiro I. 1996. Partial melting of a fertile mantle peridotite at high pressures: an experimental study using aggregates of diamond. In Earth Processes: Reading the Isotopic Code, ed. A Basu, SR Hart. Geophysical Monograph 95:109–22 Am. Geophys. Union, Washington, DC
- Kwagalakwe, A., Stamps, D. S., Njinju, E. A., Rajaonarison, T., Evans, R. L., Atekwana, E. A., Taylor, M., Katumwehe, A. B., Barry, P. H., Mwongyera, H., Kiberu, J. M., Kabanda, A., & Nakajigo, J. (2024). Lithospheric Modulated Convection (LMC) and Tomography-Based Convection (TBC) ASPECT code [Software]. Zenodo. https://doi.org/10.5281/zenodo.11051692
- Lavayssière, A., Greenfield, T., Keir, D., Ayele, A., & Kendall, J. M. (2019). Local seismicity near the actively deforming Corbetti volcano in the Main Ethiopian Rift. Journal of Volcanology and Geothermal Research, 381, 227-237.
- Lavier, L. L., & Manatschal, G. (2006). A mechanism to thin the continental lithosphere at magma-poor margins. Nature, 440(7082), 324-328.
- Leseane, K., Atekwana, E. A., Mickus, K. L., Abdelsalam, M. G., Shemang, E. M., & Atekwana, E. A. (2015). Thermal perturbations beneath the incipient Okavango Rift Zone, northwest Botswana. Journal of Geophysical Research: Solid Earth, 120(2), 1210-1228.
- Li, X., Kind, R., Yuan, X., Wölbern, I., & Hanka, W. (2004). Rejuvenation of the lithosphere by the Hawaiian plume. Nature, 427(6977), 827-829.
- Lindenfeld, M., & Rümpker, G. (2011). Detection of mantle earthquakes beneath the East African Rift. Geophysical Journal International, 186(1), 1-5.
- Lindenfeld, M., Rümpker, G., Batte, A., & Schumann, A. (2012). Seismicity from February 2006 to September 2007 at the Rwenzori Mountains, East African Rift: earthquake distribution, magnitudes and source mechanisms. Solid Earth, 3(2), 251-264.

- Link, K., Koehn, D., Barth, M. G., Tiberindwa, J. V., Barifaijo, E., Aanyu, K., & Foley, S. F. (2010). Continuous cratonic crust between the Congo and Tanzania blocks in western Uganda. International Journal of Earth Sciences, 99, 1559-1573.
- Macdonald, R. (2002). Magmatism of the Kenya Rift Valley: a review. Earth and Environmental Science Transactions of the Royal Society of Edinburgh, 93(3), 239-253.
- Masek, J. G., Isacks, B. L., Fielding, E. J., & Browaeys, J. (1994). Rift flank uplift in Tibet: Evidence for a viscous lower crust. Tectonics, 13(3), 659-667.
- Masse, R. P., & Needham, R. E. (1989). NEIC-The national earthquake information center. Earthquakes & Volcanoes (USGS), 21(1), 4-44.
- Masse, R. P., & Needham, R. E. (1989). NEIC-The national earthquake information center. Earthquakes & Volcanoes (USGS), 21(1), 4-44.
- Mckenzie, D. A. N., & Bickle, M. J. (1988). The volume and composition of melt generated by extension of the lithosphere. Journal of petrology, 29(3), 625-679.
- Meshesha, D., & Shinjo, R. (2008). Rethinking geochemical feature of the Afar and Kenya mantle plumes and geodynamic implications. Journal of Geophysical Research: Solid Earth, 113(B9).
- Molendijk, S. M., Namur, O., Kamate Kaleghetso, E., Mason, P. R., Smets, B., Vander Auwera, J., & Neave, D. A. (2024). Plumbing system architecture and differentiation processes of the Nyiragongo volcano, DR Congo. Journal of Petrology, 65(1), egad088.
- Morgan, J. P. (1987). Melt migration beneath mid‐ocean spreading centers. Geophysical Research Letters, 14(12), 1238-1241.
- Moucha, R., & Forte, A. M. (2011). Changes in African topography driven by mantle convection. Nature Geoscience, 4(10), 707-712.
- Muirhead, J. D., Kattenhorn, S. A., Lee, H., Mana, S., Turrin, B. D., Fischer, T. P., ... & Stamps, D. S. (2016). Evolution of upper crustal faulting assisted by magmatic volatile release during early-stage continental rift development in the East African Rift. Geosphere, 12(6), 1670-1700.
- Mulibo, G. D., & Nyblade, A. A. (2013). Mantle transition zone thinning beneath eastern Africa: Evidence for a whole mantle superplume structure. Geophysical Research Letters, 40(14), 3562-3566.
- Mulibo, G. D., & Nyblade, A. A. (2016). The seismotectonics of Southeastern Tanzania: Implications for the propagation of the eastern branch of the East African Rift. Tectonophysics, 674, 20-30.
- Naliboff, J., & Buiter, S. J. (2015). Rift reactivation and migration during multiphase extension. Earth and Planetary Science Letters, 421, 58-67.
- Naliboff, J. B., Glerum, A., Brune, S., Péron‐Pinvidic, G., & Wrona, T. (2020). Development of 3‐D rift heterogeneity through fault network evolution. Geophysical Research Letters, 47(13), e2019GL086611.
- Niu, Y., Waggoner, D. G., Sinton, J. M., & Mahoney, J. J. (1996). The East Pacific Rise, 18"-19" S. Journal of Geophysical Research, 101(B12), 27-711.

- Njinju, E. A., Stamps, D. S., Atekwana, E. A., Rooney, T. O., & Rajaonarison, T. A. (2023). Instantaneous 3D tomography-based convection beneath the Rungwe Volcanic Province, East Africa: implications for melt generation. Geophysical Journal International, 235(1), 296-311.
- Njinju, E. A., Stamps, D. S., Neumiller, K., & Gallager, J. (2021). Lithospheric control of melt generation beneath the Rungwe Volcanic Province, East Africa: Implications for a plume source. Journal of Geophysical Research: Solid Earth, 126(5), e2020JB020728.
- Nyblade, A. A., & Langston, C. A. (1995). East African earthquakes below 20 km depth and their implications for crustal structure. Geophysical Journal International, 121(1), 49-62.
- O'Donnell, J. P., Adams, A., Nyblade, A. A., Mulibo, G. D., & Tugume, F. (2013). The uppermost mantle shear wave velocity structure of eastern Africa from Rayleigh wave tomography: Constraints on rift evolution. Geophysical Journal International, 194(2), 961-978.
- O'Donnell, J. P., Selway, K., Nyblade, A. A., Brazier, R. A., Tahir, N. E., & Durrheim, R. J. (2016). Thick lithosphere, deep crustal earthquakes and no melt: a triple challenge to understanding extension in the western branch of the East African Rift. Geophysical Journal International, 204(2), 985-998.
- Pasteels, P., Villeneuve, M., De Paepe, P., & Klerkx, J. (1989). Timing of the volcanism of the southern Kivu province: implications for the evolution of the western branch of the East African Rift system. Earth and Planetary Science Letters, 94(3-4), 353-363.
- Pasyanos, M. E., Masters, T. G., Laske, G., & Ma, Z. (2014). LITHO1. 0: An updated crust and lithospheric model of the Earth. Journal of Geophysical Research: Solid Earth, 119(3), 2153-2173.
- Peace, A., McCaffrey, K., Imber, J., van Hunen, J., Hobbs, R., & Wilson, R. (2018). The role of pre-existing structures during rifting, continental breakup and transform system development, offshore West Greenland. Basin Research, 30(3), 373-394.
- Pickford, M., Senut, B., & Hadoto, D. (1993). Geology and palaeobiology of the Albertine Rift valley, Uganda-Zaire. Volume I: geology. Publication occasionnelle-Centre international pour la formation et les échanges géologiques, (24).
- Pik, R., Marty, B., Carignan, J., Yirgu, G. and Ayalew, T., 2008. Timing of East African Rift development in southern Ethiopia: Implication for mantle plume activity and evolution of topography. Geology, 36(2), pp.167-170.
- Pouclet, A., & Bram, K. (2021). Nyiragongo and Nyamuragira: a review of volcanic activity in the Kivu rift, western branch of the East African Rift System. Bulletin of Volcanology, 83(2), 10.
- Priestley, K., McKenzie, D., Debayle, E., & Pilidou, S. (2008). The African upper mantle and its relationship to tectonics and surface geology. Geophysical Journal International, 175(3), 1108-1126.

- Rajaonarison, T. A., Stamps, D. S., Fishwick, S., Brune, S., Glerum, A., & Hu, J. (2020). Numerical modeling of mantle flow beneath Madagascar to constrain upper mantle rheology beneath continental regions. Journal of Geophysical Research: Solid Earth, 125(2), e2019JB018560.
- Rajaonarison, T. A., Stamps, D. S., & Naliboff, J. (2021). Role of lithospheric buoyancy forces in driving deformation in East Africa from 3D geodynamic modeling. Geophysical Research Letters, 48(6), e2020GL090483.
- Ring, U. (2008). Extreme uplift of the Rwenzori Mountains in the East African Rift, Uganda: Structural framework and possible role of glaciations. Tectonics, 27(4).
- Ring, U. (2014). The East African Rift System. Austrian Journal of Earth Sciences, 107(1).
- Roberts, E. M., Stevens, N. J., O'Connor, P. M., Dirks, P. H. G. M., Gottfried, M. D., Clyde, W. C., & Hemming, S. (2012). Initiation of the western branch of the East African Rift coeval with the eastern branch. Nature Geoscience, 5(4), 289-294.
- Rogers, N. W. (2006). Basaltic magmatism and the geodynamics of the East African Rift System. Geological Society, London, Special Publications, 259(1), 77-93.
- Rogers, N. W., De Mulder, M., & Hawkesworth, C. J. (1992). An enriched mantle source for potassic basanites: evidence from Karisimbi volcano, Virunga volcanic province, Rwanda. Contributions to Mineralogy and Petrology, 111, 543-556.
- Rogers, N. W., James, D., Kelley, S. P., & De Mulder, M. (1998). The generation of potassic lavas from the eastern Virunga province, Rwanda. Journal of Petrology, 39(6), 1223-1247.
- Rogers, N., Macdonald, R., Fitton, J. G., George, R., Smith, M., & Barreiro, B. (2000). Two mantle plumes beneath the East African rift system: Sr, Nd and Pb isotope evidence from Kenya Rift basalts. Earth and Planetary Science Letters, 176(3-4), 387-400.
- Rooney, T. O. (2020). The Cenozoic magmatism of East Africa: part V–magma sources and processes in the East African Rift. Lithos, 360, 105296.
- Rooney, T. O., Herzberg, C., & Bastow, I. D. (2012). Elevated mantle temperature beneath East Africa. Geology, 40(1), 27-30.
- Rosenthal, A., Foley, S. F., Pearson, D. G., Nowell, G. M., & Tappe, S. (2009). Petrogenesis of strongly alkaline primitive volcanic rocks at the propagating tip of the western branch of the East African Rift. Earth and Planetary Science Letters, 284(1-2), 236-248.
- Saalmann, K., Mänttäri, I., Nyakecho, C., & Isabirye, E. (2016). Age, tectonic evolution and origin of the Aswa Shear Zone in Uganda: activation of an oblique ramp during convergence in the East African Orogen. Journal of African Earth Sciences, 117, 303-330.
- Saria, E., Calais, E., Stamps, D. S., Delvaux, D., & Hartnady, C. J. H. (2014). Present‐day kinematics of the East African Rift. Journal of Geophysical Research: Solid Earth, 119(4), 3584-3600.

- Savage, J. E. G., & Long, R. E. (1985). Lithospheric structure beneath the Kenya dome. Geophysical Journal International, 82(3), 461-477.
- Schellart, W. P. (2004). Kinematics of subduction and subduction‐induced flow in the upper mantle. Journal of Geophysical Research: Solid Earth, 109(B7).
- Sen, G. (2001). Generation of Deccan trap magmas. Journal of Earth System Science, 110, 409-431.
- Seyler, M., Lorand, J. P., Dick, H. J., & Drouin, M. (2007). Pervasive melt percolation reactions in ultra-depleted refractory harzburgites at the Mid-Atlantic Ridge, 15 20′ N: ODP Hole 1274A. Contributions to Mineralogy and Petrology, 153, 303-319.
- Sigurdsson, H., Houghton, B., McNutt, S., Rymer, H., & Stix, J. (Eds.). (2015). The encyclopedia of volcanoes. Elsevier.
- Sleep, N. H. (1992). Hotspot volcanism and mantle plumes. Annual Review of Earth and Planetary Sciences, 20(1), 19-43.
- Smets, B., Delvaux, D., Ross, K. A., Poppe, S., Kervyn, M., d'Oreye, N., & Kervyn, F. (2016). The role of inherited crustal structures and magmatism in the development of rift segments: Insights from the Kivu basin, western branch of the East African Rift. Tectonophysics, 683, 62-76.
- Stamps, D. S., Calais, E., Saria, E., Hartnady, C., Nocquet, J. M., Ebinger, C. J., & Fernandes, R. M. (2008). A kinematic model for the East African Rift. Geophysical Research Letters, 35(5).
- Stamps, D. S., Flesch, L. M., & Calais, E. (2010). Lithospheric buoyancy forces in Africa from a thin sheet approach. International Journal of Earth Sciences, 99, 1525-1533.
- Stamps, D. S., Flesch, L. M., Calais, E., & Ghosh, A. (2014). Current kinematics and dynamics of Africa and the East African Rift System. Journal of Geophysical Research: Solid Earth, 119(6), 5161-5186.
- Stamps, D. S., Kreemer, C., Fernandes, R., Rajaonarison, T. A., & Rambolamanana, G. (2021). Redefining east African rift system kinematics. Geology, 49(2), 150-155.
- Stamps, D. S., Iaffaldano, G., & Calais, E. (2015). Role of mantle flow in Nubia‐Somalia plate divergence. Geophysical Research Letters, 42(2), 290-296.
- Tugend, J., Gillard, M., Manatschal, G., Nirrengarten, M., Harkin, C., Epin, M. E., & McDermott, K. (2020). Reappraisal of the magma-rich versus magma-poor rifted margin archetypes. Geological Society, London, Special Publications, 476(1), 23-47.
- Turcotte, D. L., & Schubert, G. (2002). Geodynamics. Cambridge university press.
- van Herwaarden, D. P., Boehm, C., Afanasiev, M., Thrastarson, S., Krischer, L., Trampert, J., & Fichtner, A. (2020). Accelerated full-waveform inversion using dynamic mini-batches. Geophysical Journal International, 221(2), 1427-1438.
- van Zelst, I., Crameri, F., Pusok, A. E., Glerum, A., Dannberg, J., & Thieulot, C. (2022). 101 geodynamic modelling: how to design, interpret, and communicate numerical studies of the solid Earth. Solid Earth, 13(3).

- Wallner, H., & Schmeling, H. (2011). Sensitivity analysis of rift induced delamination with application to Rwenzori Mountains. *Geophysical Journal International*, *187*(3), 1135-1145.
- Wang, T., Gao, S. S., Yang, Q., Chen, L., & Liu, K. H. (2022). Lithospheric Structure underneath the Archean Tanzania Craton and Adjacent Regions from a Joint Inversion of Receiver Functions and Rayleigh‐Wave Phase Velocity Dispersion. Seismological Society of America, 93(3), 1753-1767.
- Watson, S., & McKenzie, D. A. N. (1991). Melt generation by plumes: a study of Hawaiian volcanism. Journal of Petrology, 32(3), 501-537.
- Wauthier, C., Cayol, V., Poland, M., Kervyn, F., d'Oreye, N., Hooper, A., & Smets, B. (2013). Nyamulagira's magma plumbing system inferred from 15 years of InSAR. Geological Society, London, Special Publications, 380(1), 39-65.
- Wauthier, C., Smets, B., & Keir, D. (2015). Diking‐induced moderate‐magnitude earthquakes on a youthful rift border fault: The 2002 Nyiragongo‐Kalehe sequence, DR Congo. Geochemistry, Geophysics, Geosystems, 16(12), 4280-4291.
- Wedmore, L. N., Biggs, J., Floyd, M., Fagereng, Å., Mdala, H., Chindandali, P., ... & Mphepo, F. (2021). Geodetic constraints on cratonic microplates and broad strain during rifting of thick Southern African lithosphere. Geophysical Research Letters, 48(17), e2021GL093785.
- Weeraratne, D. S., Forsyth, D. W., Fischer, K. M., & Nyblade, A. A. (2003). Evidence for an upper mantle plume beneath the Tanzanian craton from Rayleigh wave tomography. Journal of Geophysical Research: Solid Earth, 108(B9).
- Weinstein, A., Oliva, S. J., Ebinger, C. J., Roecker, S., Tiberi, C., Aman, M., & Fischer, T. P. (2017). Fault-magma interactions during early continental rifting: Seismicity of the Magadi-Natron-Manyara basins, Africa. Geochemistry, Geophysics, Geosystems, 18(10), 3662-3686.
- Wessel, P., Luis, J. F., Uieda, L., Scharroo, R., Wobbe, F., Smith, W. H., & Tian, D. (2019). The generic mapping tools version 6. Geochemistry, Geophysics, Geosystems, 20(11), 5556-5564.
- Wilson, M. (1992). Magmatism and continental rifting during the opening of the South Atlantic Ocean: a consequence of Lower Cretaceous super-plume activity?. Geological Society, London, Special Publications, 68(1), 241-255.
- Wölbern, I., Rümpker, G., Link, K., & Sodoudi, F. (2012). Melt infiltration of the lower lithosphere beneath the Tanzania craton and the Albertine rift inferred from S receiver functions. Geochemistry, Geophysics, Geosystems, 13(8).
- Wölbern, I., Rümpker, G., Schumann, A., & Muwanga, A. (2010). Crustal thinning beneath the Rwenzori region, Albertine rift, Uganda, from receiver-function analysis. International Journal of Earth Sciences, 99, 1545-1557.

- Yang, Z., & Chen, W. P. (2010). Earthquakes along the East African Rift System: A multiscale, system‐wide perspective. Journal of Geophysical Research: Solid Earth, 115(B12).
- Yu, Y., Gao, S. S., Zhao, D., & Liu, K. H. (2020). Mantle structure and flow beneath an early‐stage continental rift: Constraints from P wave anisotropic tomography. Tectonics, 39(2), e2019TC005590.
- Yu, Y., Liu, K. H., Huang, Z., Zhao, D., Reed, C. A., Moidaki, M., & Gao, S. S. (2017). Mantle structure beneath the incipient Okavango rift zone in southern Africa. Geosphere, 13(1), 102-111.

CHAPTER TWO

Constraining the Kinematics of the Northern Western Branch of the East African Rift System using GNSS Geodesy

The original version of this work is under review in Geophysical Research Letter as:

Kwagalakwe, A., Stamps, D.S., Kolawole, F., Atekwana, E.A., Taylor, M., Atekwana, E.A., Katumwehe, A.B., Barry, P.H., Njinju, E.A., Nyago, J., Tugume, F., Kiberu, J.M., Nakajigo, J., Kabanda, A. (under review). Constraining the kinematics of the northern Western Branch of the East African Rift System using GNSS geodesy, *Geophysical Research Letters*.

Abstract

The fragmentation of continents nucleates microplates that rotate to accommodate the lateral propagation of bounding rift tips. Yet, the relationships between microplate rotation rates, fault slip rates, and kinematics at propagating rift tips remain unknown. Here, we analyze new Global Navigation Satellite System (GNSS) data and structural geology data from the northern Western Branch (NWB) of the East African Rift System that defines part of the boundary between the Nubian plate and Victoria microplate. We resolve a 0.0623±0.0293 deg/My counterclockwise rotation of the Victoria microplate, consistent with previous studies, but with the Euler pole ~376 km northwest of earlier work. Strain rates along the block boundaries range from 7.6×10^{-8} to 1.36×10^{-7} y^{-1} largely localized on microplate-bounding faults with 1.93-2.34 mm/y slip rates. Our kinematic model indicates that Victoria Plate rotation is accommodated by oblique-slip on the NWB border faults.

1. Introduction

The break-up of continents typically occurs along rift branches that host rift basins, which avoid cratons, follow orogenic belts and suture zones, and define distinct microplates at less deformed continental areas between the rift branches or, on a smaller scale, within overlapping rift basins (e.g., Allken et al. 2012; Calais et al., 2006; Colet et al., 2025; Glerum et al., 2022; Heron et al., 2023; Martin, 2023; Müller et al., 2001; Neuharth et al., 2021). In oceanic lithosphere, the initiation of microplates in extensional settings begins with initial brittle deformation along their boundaries and interior, followed by strain localization along bounding spreading ridges and rotation about its vertical axis (Bird et al., 1998). However, limited understanding exists regarding strain accommodation across microplates, space-time rigidity evolution, and implications for rift kinematics and progressive lithospheric fragmentation in extending continents.

In Africa, debate on the movement and deformation of the Victoria microplate raise questions about the kinematics of the Western Branch of the East African Rift System (EARS).

Previous studies about the kinematics of the Victoria microplate (e.g., Calais et al., 2006; Stamps et al., 2008; Fernandes et al., 2013; Saria et al., 2014), which were constrained by sparsely distributed Global Navigation Satellite System (GNSS) velocities, have been challenged for potential bias that may be due to limited data that was available at that time. A counterclockwise angular velocity of 0.0620±0.026 deg/My of the Victoria microplate has been estimated by the most recent kinematic model of Saria et al. (2014), with predicted ~E-W extension rates of ~1.3 to ~1.7 mm/y along the northern Western Branch (NWB). However, since the region is seismically active (e.g., Masse & Needham, 1989; Xue et al., 2020) and new observations of crustal deformation in the NWB from new GNSS data are available (Figure 1; Kwagalakwe et al., 2023, 2024; Stamps et al., 2015, 2022), there is an opportunity to provide improved seismic hazards assessments by updating the kinematics of the NWB and of the Victoria microplate using more evenly distributed GNSS data.

Given that some of our new GNSS observations are along the NWB, we provide the first ever estimates of geodetic fault slip rates in this region. The NWB is an active rift zone located in the northernmost region of the Western Branch of the EARS, which initiated between 20-25 Ma (Roberts et al., 2012). The NWB forms part of the plate boundary between the Victoria microplate and the Nubian plate. It also comprises the magma-rich Lakes George-Edward graben in the south and the magma-poor Albertine and Rhino grabens at its apparent northern termination (Figure 1b). The rift valleys in the NWB are bordered by active faulting (Mwongyera et al., 2024; Styron & Pagani, 2020: Figure 1b). Holocene volcanism (Global Volcanism Program, 2013) is observed in the Lakes George-Edwards region and pervasive seismicity occurs along the entire NWB (e.g., Masse & Needham, 1989; Xue et al., 2020; Figure 1a).

Here, we update the kinematics of the Victoria microplate using 425% more GNSS velocities than the latest kinematic model (Saria et al., 2014). Further, we evaluate the consistency of our model with the kinematics of strain accommodation at the bounding rift zones via paleostress inversion of geological paleoslip data (Kolawole et al., 2025). The findings in our study provide first order implications for the evolution of continental extensional microplates and the progressive localization of strain onto their bounding propagating rifts.

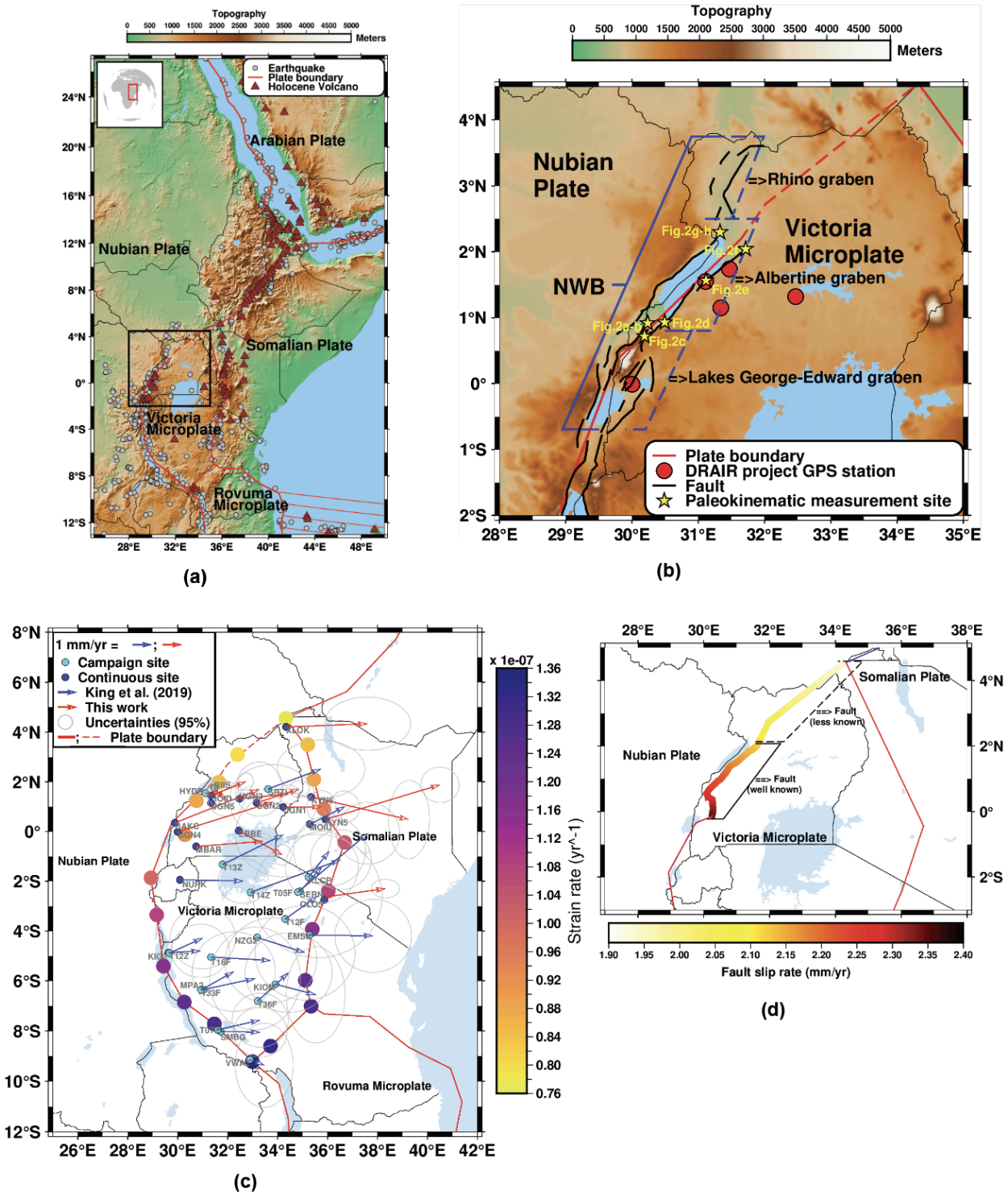

Figure 1. a) Map showing the study region with plate boundaries and deformation zones as red lines (Saria et al., 2014; Stamps et al., 2021), Holocene volcanoes as brown triangles (Global Volcanism Program, 2013), and earthquakes (gray circles) from 2015-2025 from the NEIC (Masse & Needham, 1989). Black box represents Figure 1b, while the inset map shows the relative location of the study region (red color) on Earth. b) Map of the northern Western Branch

(NWB), including the magma-rich Lakes George-Edward graben and the magma-poor Albertine and Rhino grabens. Major faults are represented by black solid lines. Red circles show locations of the new GNSS stations installed for the DRIAR project. Yellow stars are locations of paleokinematic measurements (Figures 2b-i). c) Map of horizontal GNSS velocities with respect to a fixed-Nubian plate with 95% uncertainties (light gray ellipses). Cyan circles are campaign stations. Blue circles are continuous stations. Blue vectors are GNSS solutions processed by King et al. (2019), and red vectors are GNSS solutions processed in this work. Predicted strain rates at selected locations along the Victoria microplate boundary from our preferred kinematic (Tables 2 & S1) model in yr^{-1} as indicated by the colored circles and the color bar. d) Estimated fault slip rates in mm/y along the NWB for our preferred model (Tables 2 & S1).

2. Methods

2.1. GPS Data Processing

We use GNSS data collected from 15 continuous and 21 campaign GNSS stations throughout the Victoria Microplate (Table 1 & Figure 1c). The GNSS data used is a combination of newly processed data acquired during this study and a velocity solution published by King et al. (2019) (Table 1 & Figure 1c). All of the continuous GNSS stations (Table 1 & Figure 1c) used in the study have been operational for at least 2.5 years (Blewitt & Lavallée, 2002), and campaign sites have at least three surveys, each lasting at least 72 hours, in three different years (e.g., Floyd et al., 2010). We use the processing software GAMIT/GLOBK version 10.76 (Herring et al., 2018) to process newly acquired GNSS data to obtain precise solutions (daily position time-series and velocities).

We carry out GNSS processing with GAMIT/GLOBK in three steps. First, raw GNSS data are processed to produce loosely constrained daily solutions of site positions using GAMIT. Second, daily GNSS position solutions are combined and transformed into the International Terrestrial Reference Frame 2014 (ITRF14; Altamimi et al., 2017) by applying a daily Helmert transformation that estimates translation, rotation, and scale components to derive daily positions at each site to form time-series. The position time-series of each site are then inspected to detect and remove outliers by using a spatial filtering technique similar to that of Wdowinski et al. (1997). Observations with positional uncertainty greater than 5 mm in either the horizontal component or 10 mm in the vertical component are removed. The use of both daily Helmert transformations and a filtering algorithm helps to reduce common mode errors (Williams et al., 2004). Third, the combined solutions for each cleaned daily solution at each site are passed through a Kalman filter (GLOBK) to estimate a consistent set of coordinates and velocities with their associated variance-covariance matrix. To have more realistic uncertainties on the velocities, we add random walk noise (Herring et al., 2018). Finally, the GNSS site velocities are then transformed into a Nubian-fixed reference frame using the angular velocity vector for Nubian relative to the ITRF2014 (Altamimi et al., 2017). We then use the GLOBK program velrot (Herring et al., 2018) to combine velocity fields from King et al. (2019) and this work into

a single, consistent velocity solution that is in a Nubian-fixed reference frame based on ITRF2014 (Altamimi et al., 2017).

2.2. TDEFNODE Block Modeling

We use TDEFNODE software (McCaffrey, 2005; 2009; McCaffrey et al., 2002, 2007) to invert our combined horizontal GNSS velocity solution to determine the best fit angular velocity vector for the Victoria microplate with respect to the Nubian plate (Table 2 & Figure 2a), assess for internal deformation, and calculate geodetic fault slip rates (Figure 1d) along the northern Western Branch (NWB). At several points along the block boundary that are between ~15 km and ~100 km apart, we also calculate strain rates using our preferred kinematic model (tst6: Tables 2 & S1) from the relative plate motions assuming a constant length extension of ~25 km (Google Earth, 2001) along the plate boundary (Figure 1c). Our block model consists of the Victoria microplate, the Nubian plate, and a west-dipping fault that is along the NWB (Figures 1 & 2a). Details of the TDEFNODE inversion approach are provided in the Supplementary Information (Text S2). In addition, all input and output files needed to reproduce our TDEFNODE results are provided in the Zenodo repository of Kwagalakwe et al. (2025).

To test for internal strain (i.e., if the Victoria block is deforming internally), we invert the GNSS velocities with and without solving for strain rates within the block and assess which scenario is a statistically better fit to the input data (Table S1). To obtain strain rates along the boundaries of the block (Figure 1c), we used the basic equation of strain rate equals extension rate, i.e., the relative plate motion (Figure 2a) divided by the relative length for which the block has moved 25 km based on the average half-width of the rifts bounding the Victoria microplate.

The modeled faults have a maximum depth of 15 km (Figure S1) based on the seismic activity in this region. The geodetic fault slip rates across the block-bounding fault (Figure 1d) are determined by calculating the difference in linear velocities between two blocks from the Euler poles. Although some part of this relative slip rate on the fault does not occur steadily, a phenomenon referred to as fault locking. Fault locking leads to an accumulation of strain rates and velocity perturbations, which are calculated using the back-slip method of Savage (1983) and Okada (1985, 1992) to compute surface velocities around locked faults in a homogeneous, elastic half-space (McCaffrey, 2005, 2009; McCaffrey et al., 2002, 2007). The Okada model uses Green's function solutions to calculate displacements and strain rates at the free surface using inputs of the fault geometry (length, width, depth, strike, and dip of the fault) and 3-component dislocation amplitude (rake, slip, and open).

2.3. Geological Investigation of Plate Boundary Kinematics at NWB

To evaluate our GNSS plate boundary kinematic model and understand how tectonic stress is resolved on major faults, we analyze geological paleoslip data (Kolawole et al., 2025) from outcrops of the border faults along the Albertine graben (Figures 1b & 2b-j). The paleoslip dataset from Kolawole et al. (2025) include measurements of slickensided slip surfaces and

slickenlines on outcrops of the principal zone of the rift border faults, which include the Kibuku, Rwimi-Wasa, Tonya, Toro-Bunyoro, and Bunia faults (Figures 1b & 2b-i). We follow standard procedures (e.g., Angelier & Mechler, 1977; Angelier, 1989; Delvaux & Sperner, 2003; Delvaux et al., 2012) to invert the paleoslip dataset in order to resolve a uniform stress field (paleostress) for the Albertine graben. For a more extended explanation of this inversion process, see the Supplementary Information.

3. Results

Table 1 displays GNSS stations and their velocity solutions for the Victoria microplate relative to the Nubian plate, using the ITRF14 reference frame (Altamimi et al., 2017). Table 1 also has information about data collection timeframes. Additionally, Figure 1c displays GNSS horizontal velocities in the Victoria microplate with 2-sigma uncertainties for a fixed Nubian plate. The highest horizontal velocity magnitude is at KYN5 (6.25±0.56 mm/y) and the lowest is at VWAZ (0.8±1.09 mm/y).

Table 2 and Figure 2a show our new kinematic model of the Victoria microplate compared to previous models by Saria et al. (2014) and Stamps et al. (2008). Our results indicate that the Victoria microplate is rotating counterclockwise at an angular velocity of 0.0623±0.0293 deg/My similar to the rate of Saria et al. (2014); however, the Euler poles are not in the same location within uncertainties. The Euler pole from this study is ~376 km north and west of the Euler pole calculated by Saria et al. (2014). The change in location of the Euler pole based on our results does not imply that the Victoria microplate has changed its style of motion since the latest kinematic from Saria et al. (2014), rather with the denser GNSS velocity solution we are using, we find a better constrained location for the Victoria microplate Euler pole. Our best-fit kinematic model indicates that the southern regions, farthest from our calculated Euler pole, move faster than the northern regions, as shown in Figure 2a.

Figure 1c displays the strain rates (colored circles and color bar) calculated along the Victoria microplate boundary at selected locations with rates ranging from 7.6×10^{-8} to 1.36×10^{-7} y^{-1} with a standard error of 1.86×10^{-8} y^{-1}. We find that the geodetic fault slip rates in this region range from 1.93-2.34 mm/y with a standard error of 0.36 mm/y (Figure 1d).

Geological mapping of paleoslip vectors on exhumed border fault slip surfaces along the Albertine graben show a predominance of oblique-slip normal-shear slickenlines (Figures 2b-i). The kinematic solution for each measurement location generally shows normal faulting focal mechanism solutions but with varying magnitudes of obliquity (see insets in Figures 2b-i). Our paleostress inversion (Figure 2j) resolves a normal faulting regional tectonic stress regime (stress ratio index R'=0.48±0.13) with a NNE-SSW-oriented minimum principal stress axis (σ_3). This σ_3 axis is consistent with our geodetic model of NE-SW plate motion direction along the NWB (Figure 2a).

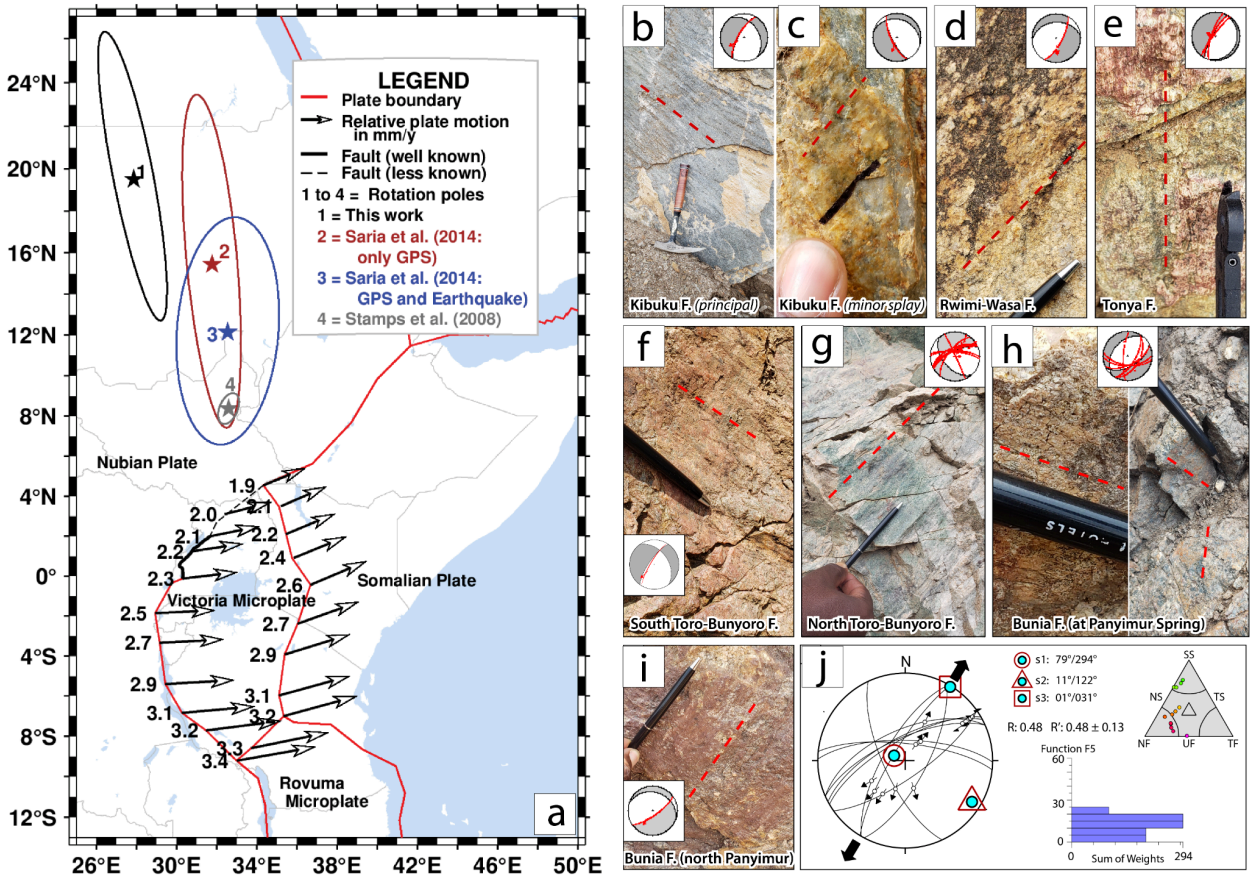

Figure 2. a) Predicted relative motions (black and white vectors) along the Victoria microplate boundary from our preferred kinematic model (Tables 2 & S1) in a Nubia-fixed reference frame. The black, red, blue, and gray stars represent the Euler poles and their 95% uncertainty ellipses for this work, Saria et al. (2014: only GNSS velocities), Saria et al. (2014: GNSS velocities and earthquake slip vectors), and Stamps et al. (2008), respectively. The thick, black solid line in the northern Western Branch (NWB) represents the modeled fault that has been mapped in the field (Mwongyera et al., 2024), whereas the black dashed line represents a modeled fault/block boundary that is poorly constrained. b-i) Photographs showing ubiquitous oblique-normal slickenlines on exhumed border fault slip surfaces along the Albertine graben (Figure 1b), including b-c) Kibuku Fault, d) Rwimi-Wasa Fault, e) Tonya Fault, f) South Toro-Bunyoro Fault near Buseruka, g) North Toro-Bunyoro Fault, and h-i) Bunia Fault in the Panyimur area. j) Paleostress inversion results for the highest quality geological slip vectors measured on the fault surfaces, resolving a regional σ_3 orientation that is similarly oriented obliquely to the NWB rift axes, similar to our GNSS-resolved NWB motion direction.

Table 1: GNSS velocity solutions of Victoria microplate sites relative to the Nubian plate (Altimimi et al., 2017). V_e, V_n and V_u are velocities in the east, north, and up directions. σ_e, σ_n, and σ_u are the 2-sigma uncertainties. $corr_{en}$ is the correlation.

Site name	Lon (°)	Lat (°)	V_e (mm/y)	V_n (mm/y)	V_u (mm/y)	σ_e (mm/y)	σ_n (mm/y)	σ_u (mm/y)	$corr_{en}$	Years of data collection

a) Processed in this study										
BAKC	29.893	0.350	4.41	1.76	5.37	0.51	0.58	1.04	0.000	3.18
BIIS	31.474	1.736	0.61	-0.62	-6.77	0.39	0.34	1.23	0.000	3 epochs
EBBE	32.445	0.038	2.28	-1.27	-0.91	0.20	0.22	0.67	0.000	4.26
HOID	31.340	1.449	1.82	0.73	-3.47	0.16	0.19	1.63	0.001	7.61
HYDP	31.112	1.546	0.88	0.00	-3.85	0.35	0.28	0.89	0.000	3 epochs
KYN5	35.921	0.488	5.99	1.81	2.38	0.41	0.38	9.28	-0.023	2.5
KYN6	35.344	1.391	5.12	-1.18	-6.21	0.44	0.84	2.70	0.015	2.5
MBAR	30.738	-0.601	3.51	0.28	-1.83	0.19	0.16	0.65	-0.001	16.65
UGN1	34.218	0.985	2.01	0.01	-1.78	0.31	0.35	0.94	0.016	2.5
UGN2	33.161	1.157	2.23	0.72	-3.83	0.21	0.18	0.88	0.011	2.5
UGN3	32.473	1.315	2.58	0.25	-6.03	0.24	0.20	0.81	-0.021	3.0
UGN4	30.001	-0.010	4.99	1.56	-6.25	0.93	0.80	3.44	-0.032	2.53
UGN5	31.340	1.449	1.82	0.73	-3.47	0.16	0.19	1.63	0.001	2.5
OLO5	35.889	-2.634	3.18	0.44	-4.60	0.30	0.20	1.00	-0.004	5.0
XLOK	34.343	4.206	4.26	0.17	-8.19	0.92	0.57	2.37	-0.005	2.5
b) Processed by King et al. (2019) and combined with our solution using velrot										
Note that the GNSS solutions from King et al. (2019) for continuous sites had at least 2.4 years of data collection while the campaign sites had at least 3 epochs.										
EMSK	35.277	-4.164	3.34	-0.04	2.64	0.82	0.78	17.83	0.00	
KIG2	29.637	-4.866	1.67	0.09	-1.31	0.62	0.57	7.19	0.00	
KIOM	33.912	-6.134	2.11	-0.55	1.60	0.63	1.03	2.39	0.00	
KLCP	35.242	-1.835	1.09	1.36	-3.92	0.77	0.75	4.33	-0.01	
MOIU	35.290	0.288	1.85	0.94	-1.44	0.31	0.33	0.78	-0.08	
MPA2	31.041	-6.349	2.69	0.58	-4.03	0.97	1.10	5.13	0.02	
NURK	30.090	-1.945	3.32	-0.06	-2.45	0.54	0.48	1.31	0.00	
NZG2	33.183	-4.257	2.50	-0.80	-5.15	1.07	1.01	3.54	0.00	
SERN	34.896	-2.409	1.15	1.27	3.98	0.78	0.76	11.11	0.00	
SMBG	31.715	-8.022	2.08	-0.04	0.05	0.57	0.53	2.85	0.00	
SRTI	33.620	1.710	2.77	1.05	-1.42	0.94	0.62	1.99	-0.01	
T05F	34.820	-2.437	3.66	3.08	-0.70	0.68	0.66	2.07	0.00	
T07Z	31.606	-7.951	2.22	0.50	1.08	0.60	0.58	1.72	0.00	
T12F	34.306	-3.517	1.69	1.20	-2.51	1.38	1.32	4.00	-0.01	
T12Z	29.668	-4.887	1.75	0.79	2.67	0.70	0.66	2.05	0.01	
T13Z	31.799	-1.326	3.18	1.56	5.68	1.03	0.90	3.27	0.00	
T14Z	32.923	-2.447	4.72	1.71	2.03	0.65	0.64	1.86	-0.01	
T16F	31.337	-5.046	3.13	-0.18	-0.67	0.98	0.91	3.09	0.03	
T33F	30.940	-6.365	1.71	0.96	2.25	0.89	0.85	2.74	0.01	
T36F	33.206	-6.804	1.62	1.48	4.16	0.93	0.85	2.91	0.00	
VWA2	32.894	-9.146	0.75	-0.29	0.01	0.62	0.90	1.93	0.01	

Table 2: Angular velocity solutions describing of the Victoria microplate with respect to Nubia.

** Dash (-) means not applicable or missing value.*

Parameters	Symbol	Units	Stamps et al. (2008: using GNSS velocities and Earthquake slip vectors)	Saria et al. (2014: using GNSS velocities and Earthquake slip vectors)	Saria et al. (2014; Only GNSS velocities)	This work (Only GNSS velocities)
Plate	-	-	Victoria-Nubia	Victoria-Nubia	Victoria-Nubia	Victoria-Nubia
Longitude of pole	Lon	Deg	32.5886	32.54	31.77	27.8598
Latitude of pole	Lat	Deg	8.3696	12.14	15.44	19.515
Rotation rate (Angular velocity)	ω	Deg/My	0.1294	0.0760	0.0620	0.0623 (Positive means counterclockwise rotation)
Standard error of rotation rate	σ_ω	Deg/My	0.0058	0.012	0.026	0.0293
Maximum axis of lon/lat error ellipse	Emax	Deg	1.8	12.4	17.9	15.41
Minimum axis of lon/lat error ellipse	Emin	Deg	1.0	5.5	2.7	2.09
Azimuth of maximum axis of lon/lat error ellipse	Azi	Deg	22.55	4.4	174.8	169.0
X component of angular velocity	ωx	Deg/My	0.1079	0.0626	0.0508	0.0519
Y component of angular velocity	ωy	Deg/My	0.0689	0.0399	0.0315	0.0275
Z component of angular velocity	ωz	Deg/My	0.0188	0.0159	0.0165	0.0208
Standard error of ωx	Sx	Deg/My	-	0.000	0.000	0.026
Standard error of ωy	Sy	Deg/My	-	0.000	0.000	0.017
Standard error of ωz	Sz	Deg/My	-	0.000	0.000	0.006

4. Discussion

Estimates of how the surface moves from block kinematic modeling aid in our understanding of active tectonics as well as long-term movements of the plates/blocks and the surrounding regions (e.g., Argus et al., 1995; Burgmann et al., 2002; Calais & Minster, 1995; Kusche & Schrama, 2005; Larson et al., 2010; Larson and Freymueller, 1997; McCaffrey et al., 2002, 2005, 2007, 2009; Saria et al., 2014; Stamps et al., 2008, 2014; Wang et al., 2017). The results of this study indicate that the Victoria microplate has a counterclockwise rotation (Table 2), which is consistent with previous geodetic studies (e.g., Fernandes et al., 2013; Saria et al.

2014; Stamps et al., 2008). The result of this work is also consistent with the previous findings of Hartnady (2002) who proposed that the Victoria microplate is a coherent tectonic block, distinct from its surrounding plates and microplates. We also find that the Victoria microplate is rotating counterclockwise, similar to previous estimates that included earthquake slip vector data in addition to GNSS data, which were used to constrain the rotation rate and direction (e.g., Fernandes et al., 2013; Saria et al., 2014; Stamps et al., 2008).

We find that the relative velocity of plate motion of the western part of the Victoria microplate, which includes the large portions of the Western Branch, relative to the Nubian plate are slightly higher than those of Saria et al. (2014) because of the new location of the Euler pole. For instance, the predicted extension rates between the Lakes George-Edward graben and the Albertine graben in the NWB range from 2.1 to 2.3 mm/y in this study but are only 1.7 mm/y in Saria et al. (2014). Although the difference in rate is only about 0.5 mm/y, the difference is significant when considering 2-sigma uncertainties.

The northern Western Branch (NWB) is primarily considered to have dip-slip faults, specifically normal faults, with minor dextral and sinistral strike-slip motion (e.g., Abeinomugisha & Kasande, 2012; Hollinsworth et al., 2019); therefore, the positive geodetic fault slip rate values (Figure 1d) mostly represent extension rather than strike-slip motion. If our fault slip rate values were negative, our kinematic model (tst6) would predict contraction. The predicted present-day geodetic fault slip rates of the southern part of the NWB (i.e., the Lakes George-Edward graben and southern Albertine graben) are higher than the northern part of the NWB (Figure 1d; Rhino graben) implying that more deformation is occurring in the southern part of this region than the northern part. Previous studies, including geophysical and geologic, suggest that Lakes George-Edward graben and the southern Albertine graben are more tectonically active with volcanoes and hot springs compared to the Rhino graben (Figure 1; Abeinomugisha & Kasande, 2012; Pasteels et al., 1989; Pouclet & Bram, 2021). Field observations of tectonic geomorphology are consistent with active to recently active extensional faults deforming the landscape, but geologic fault slip rates are currently unknown. .

Earlier studies based on GNSS measurements by Stamps et al. (2018) suggest strain rates along the East African Rift System range from ~0-2×10^{-8} y^{-1}. Our computed strain rates, ranging from 7.6×10^{-8} to 1.36×10^{-7} y^{-1} with a standard error of 1.86×10^{-8} y^{-1}, are higher by at least 5.8% compared to those computed by Stamps et al. (2018). Stamps et al. (2018) found the highest strain rates in the Main Ethiopian Rift, Tanganyika Rift, and the Nubia-Victoria-Rovuma plate intersection near the Rukwa Rift and northern Malawi Rift. According to our kinematic model, we see a similar pattern where the highest strain rates are in the southern part of the Victoria microplate, for example, the Nubia-Victoria-Rovuma plate intersection, compared to the northern part, such as the Nubia-Victoria-Somalia plate intersection (Figure 1c). This result indicates that the divergent deformation along the Victoria microplate is not uniformly distributed, but mainly partitioned along its southern and northern regions. This deformation pattern also matches well with the historical record of large earthquakes being near these regions (Masse & Needham, 1989). The pattern of deformation from block kinematics and GNSS velocities yield clues for

understanding the regional tectonics and assessing block rigidity. A recent study by Birhanu et al. (2016) found large portions of the Main Ethiopian Rift experienced diffuse and broad deformation using GNSS velocities in contrast to previous studies that suggested narrow zones of deformation. Further, Stamps et al. (2021) resolved a broad zone of deformation extending from eastern Rovuma to northern Madagascar using GNSS velocities and kinematic modeling that also contradicts previous work that suggested all deformation along the East African Rift System is constrained to narrow zones bounding rigid blocks (i.e., Harnady, 2002; Stamps et al., 2008). Given that we leverage 425% more GNSS data to constrain the Victoria microplate than Saria et al. (2014), we suggest our study definitively constrains the internal rigidity of the Victoria microplate and provides an improved position of the Euler pole.

The interior of the Victoria plate hosts Neogene rift basins (Nyanza/Kavirondo, Eyasi, and Mara rift zones) that appear to have propagated into the plate from the Eastern Branch of the rift system (Mboya, 1983; Le Gall et al., 2008; Fletcher et al., 2018; Kolawole et al., 2021; Ludat & Kübler, 2022). Age-dating of rift deposits and volcanics suggest that tectonic extension started as early as the Miocene (e.g., Mboya, 1983; Macgregor, 2015), marking deformation during the early phases of establishment of the Eastern Branch of the rift system. However, relatively minimal seismicity in these rift zones and interior of the Victoria Plate compared to its margins (Figure 1a) and our GNSS microplate rigidity tests, suggest that these rifts are likely deactivating and that strain is likely now primarily localized onto the microplate boundaries. This is consistent with previously proposed space-time transitions from an initial strain accommodation along both margins and interior during initial microplate nucleation, to strain localization onto the bounding rift zones (Bird et al., 1998).

Furthermore, our paleostress inversion of geological slip vectors (Figure 2j) resolve a rift paleokinematics with NNE-SSW directed extension direction which is oblique to the NE-SW-oriented axes of the NWB rift zone. This resolved extension direction is sub-parallel to the resolved geodetic plate motion direction at the NWB (Figure 2a). Overall, the obliquity of resolved plate motion direction relative to the rift axes, suggest that the localization of tectonic strain onto the northwestern corner of the Victoria microplate margin, and ongoing rotation of the microplate are being accommodated by oblique-slip on the principal plate boundary faults.

5. Conclusions

In this study, we present a new synthesis of GNSS data within the Victoria microplate and produce a new velocity solution that consists of 36 sites (15 continuous GNSS and 21 campaign). To assess the present-day kinematics of the Victoria microplate, we employ a block modeling approach to invert the horizontal GNSS velocities. Tests for internal deformation indicate the Victoria microplate is better fit with a rigid block model with strain localization on its boundaries. Independent assessment of rift kinematics from GNSS data and geological paleoslip vectors indicates that plate motion direction and the regional σ_3 orientation are sub-parallel and are both oblique to the rift axis, suggesting that the rotation of the Victoria microplate is

accommodated by localized strain on the rift border faults along its margins and oblique slip at the northern Western Branch corner of the bounding plate boundaries.

6. Open Research

We obtained the King et al. (2019) velocity solutions from King et al. (2019). GAMIT/GLOBK software is hosted by MIT (Herring et al., 2018) while TDEFNODE software is hosted on GitHub (McCaffrey, 2009). The input model materials and output model materials used in the TDEFNODE block inversion modeling for this study are available for open access through Zenodo at Kwagalakwe et al. (2025). The field measurements of geological paleoslip data used for paleostress inversion are available for open access through Zenodo at Kolawole et al. (2025), and the Win-Tensor program for the stress inversion is available at Delvaux and Sperner (2003).

7. References

- Abbey, A. L., & Niemi, N. A. (2020). Perspectives on continental rifting processes from spatiotemporal patterns of faulting and magmatism in the Rio Grande rift, USA. Tectonics, 39(1), e2019TC005635.
- Abeinomugisha, D., & Kasande, R. (2012). Tectonic control on hydrocarbon accumulation in the intracontinental Albertine Graben of the East African rift system.
- Adobe Inc. (2019). Adobe Illustrator. Retrieved from https://adobe.com/products/illustrator
- Allken, V., Huismans, R.S. and Thieulot, C., 2012. Factors controlling the mode of rift interaction in brittle‚Äêductile coupled systems: A 3D numerical study. Geochemistry, Geophysics, Geosystems, 13(5).
- Altamimi, Z., Métivier, L., Rebischung, P., Rouby, H., & Collilieux, X. (2017). ITRF2014 plate motion model. Geophysical Journal International, 209(3), 1906-1912.
- Angelier, J. (1989). From orientation to magnitudes in paleostress determinations using fault slip data. Journal of structural geology, 11(1-2), 37-50.
- Angelier, J., & Mechler, P. (1977). On a graphical method for searching for principal stresses, also usable in tectonics and seismology: the right dihedral method. Bulletin of the Geological Society of France, 7(6), 1309–1318.
- Argus, D. F., & Heflin, M. B. (1995). Plate motion and crustal deformation estimated with geodetic data from the Global Positioning System. Geophysical Research Letters, 22(15), 1973-1976.
- Bird, R.T., Naar, D.F., Larson, R.L., Searle, R.C. and Scotese, C.R., 1998. Plate tectonic reconstructions of the Juan Fernandez microplate: Transformation from internal shear to rigid rotation. Journal of Geophysical Research: Solid Earth, 103(B4), pp.7049-7067.

- Birhanu, Y., Bendick, R., Fisseha, S., Lewi, E., Floyd, M., King, R., & Reilinger, R. (2016). GPS constraints on broad scale extension in the Ethiopian Highlands and Main Ethiopian Rift. Geophysical Research Letters, 43(13), 6844-6851.
- Blewitt, G., & Lavallée, D. (2002). Effect of annual signals on geodetic velocity. Journal of Geophysical Research: Solid Earth, 107(B7), ETG-9.
- Burgmann, R., Ayhan, M. E., Fielding, E. J., Wright, T. J., McClusky, S., Aktug, B., & Turkezer, A. (2002). Deformation during the 12 November 1999 Duzce, Turkey, earthquake, from GPS and InSAR data. Bulletin of the Seismological Society of America, 92(1), 161-171.
- Calais, E., & Minster, J. B. (1995). GPS detection of ionospheric perturbations following the January 17, 1994, Northridge earthquake. Geophysical Research Letters, 22(9), 1045-1048.
- Calais, E., Ebinger, C., Hartnady, C., & Nocquet, J. M. (2006). Kinematics of the East African Rift from GPS and earthquake slip vector data. Geological Society, London, Special Publications, 259(1), 9-22.
- Colet, M., Kolawole, F., Ajala, R., Delvaux, D. & Nkodia, H.M.D.V., 2025. Redefining the Nubian-Victoria plate boundary in East Africa: Incipient Reactivation of Failed Rifts and Initiation of a Microplate in DR Congo. Authorea Preprints DOI: 10.22541/essoar.173687319.95662295/v1.
- Delvaux, D., & Sperner, B. (2003). New aspects of tectonic stress inversion with reference to the TENSOR program.
- Delvaux, D., Kervyn, F., Macheyeki, A. S., & Temu, E. B. (2012). Geodynamic significance of the TRM segment in the East African Rift (W-Tanzania): Active tectonics and paleostress in the Ufipa plateau and Rukwa basin. Journal of Structural Geology, 37, 161-180.Dewey, J. F. (1972). Plate tectonics. Scientific American, 226(5), 56-72.
- Dunbar, J. A., & Sawyer, D. S. (1988). Continental rifting at pre-existing lithospheric weaknesses. Nature, 333(6172), 450-452.
- Fernandes, R. M. S., Miranda, J. M., Delvaux, D., Stamps, D. S., & Saria, E. (2013). Re-evaluation of the kinematics of Victoria Block using continuous GNSS data. Geophysical Journal International, 193(1), 1-10.
- Fletcher, A. W., Abdelsalam, M. G., Emishaw, L., Atekwana, E. A., Laó‐Dávila, D. A., & Ismail, A. (2018). Lithospheric controls on the rifting of the Tanzanian craton at the Eyasi basin, eastern branch of the East African rift system. Tectonics, 37(9), 2818-2832.
- Floyd, M. A., Billiris, H., Paradissis, D., Veis, G., Avallone, A., Briole, P., ... & England, P. C. (2010). A new velocity field for Greece: Implications for the kinematics and dynamics of the Aegean. Journal of Geophysical Research: Solid Earth, 115(B10).
- Frohlich, C. (1992). Triangle diagrams: ternary graphs to display similarity and diversity of earthquake focal mechanisms. Physics of the Earth and Planetary Interiors, 75(1–3), 193–198.

- Glerum, A., Brune, S., Stamps, D.S. and Strecker, M.R., 2020. Victoria continental microplate dynamics controlled by the lithospheric strength distribution of the East African Rift. Nature communications, 11(1), p.2881.
- Global Volcanism Program, 2013. Volcanoes of the World, v. 4.11.2. Venzke, E (ed.). Smithsonian Institution. Downloaded 01 Oct 2024.
- Google Earth 7.3.6.9796 (2001) Uganda, 1°22'05"N, 32°18'11"E, elevation 1,111m [online]. Available from: https://earth.google.com/web/ [accessed January 20, 2025]
- Greiner, B. (1999). Euler rotations in plate-tectonic reconstructions. Computers & geosciences, 25(3), 209-216.
- Hartnady, C. J. H. (2002), Earthquake hazard in Africa: Perspectives on the Nubia-Somalia boundary, S. Afr. J. Sci., 98, 425–428.
- Heron, P. J., Peace, A. L., McCaffrey, K. J. W., Sharif, A., Yu, A. J., & Pysklywec, R. N. (2023). Stranding continental crustal fragments during continent breakup: Mantle suture reactivation in the Nain Province of Eastern Canada. Geology, 51(4), 362-365.
- Herring, T. A., King, R. W., M. Floyd, & McClusky, S. C. (2018). Introduction to gamit/globk, Release 10.7. Massachusetts Institute of Technology, Cambridge, Massachusetts. http://www-gpsg.mit.edu/gg/
- Hollinsworth, A. D., Koehn, D., Dempster, T. J., & Aanyu, K. (2019). Structural controls on the interaction between basin fluids and a rift flank fault: Constraints from the Bwamba Fault, East African Rift. Journal of Structural Geology, 118, 236-249.
- King, R., Floyd, M., Reilinger, R., & Bendick, R. (2019). GPS velocity field (MIT 2019.0) for the East African Rift System generated by King et al. Interdisciplinary Earth Data Alliance (IEDA).
- Kolawole, F., Firkins, M. C., Al Wahaibi, T. S., Atekwana, E. A., & Soreghan, M. J. (2021). Rift interaction zones and the stages of rift linkage in active segmented continental rift systems. Basin Research, 33(6), 2984-3020.
- Kolawole, F., Foster-Baril, Z., Seeber, L., Tielke, J. A., Prakash, A., Colet, M., & Waldhauser, F. (2024). The 2024 Mw4. 8 New Jersey Intraplate Earthquake: Preferential Rupture of an Immature Rough Fault in Frictionally Unstable Basement Rocks.
- Kolawole, F., Kiberu, J. M., & Atekwana, E. (2025). Geological Paleoslip Fault Data for the Albertine Rift, Uganda [Data set]. Zenodo. https://doi.org/10.5281/zenodo.15079001
- Kusche, J. E. J. O., & Schrama, E. J. O. (2005). Surface mass redistribution inversion from global GPS deformation and Gravity Recovery and Climate Experiment (GRACE) gravity data. Journal of Geophysical Research: Solid Earth, 110(B9).
- Kwagalakwe, A., Nyago, J., Nakajigo, J., Stamps, D. S., & Tugume, F. (2023). Uganda 2023 - BIIS and HYDP [Data set]. doi:/10.7283/AJGM-1951
- Kwagalakwe, A., Nyago, J., Nakajigo, J., Stamps, D. S., & Tugume, F. (2024). Uganda 2024 - HYDP [Data set]. doi:10.7283/ESMW-4Z67
- Kwagalakwe, A., Stamps, D. S., Kolawole, F., Atekwana, E., Taylor, M., Atekwana, E., Katumwehe, A., Barry, P., Njinju, E. A., Nyago, J., Tugume, F., Kiberu, J. M., Nakajigo,

J., & Kabanda, A. (2025). Block Inversion Modeling using TDEFNODE Software [Software]. Zenodo. https://doi.org/10.5281/zenodo.15092961

- Larson, K. M., Freymueller, J. T., & Philipsen, S. (1997). Global plate velocities from the Global Positioning System. Journal of Geophysical Research: Solid Earth, 102(B5), 9961-9981.
- Larson, K. M., Poland, M., & Miklius, A. (2010). Volcano monitoring using GPS: Developing data analysis strategies based on the June 2007 Kīlauea Volcano intrusion and eruption. Journal of Geophysical Research: Solid Earth, 115(B7).
- Le Gall, B., Nonnotte, P., Rolet, J., Benoit, M., Guillou, H., Mousseau-Nonnotte, M., ... & Déverchère, J. (2008). Rift propagation at craton margin.: Distribution of faulting and volcanism in the North Tanzanian Divergence (East Africa) during Neogene times. Tectonophysics, 448(1-4), 1-19.
- Ludat, A. L., & Kübler, S. (2022). Tectonic controls on the ecosystem of the Mara River Basin, East Africa, from geomorphological and spectral indices analysis. Biogeosciences Discussions, 2022, 1-24.
- Macdonald, R. (2002). Magmatism of the Kenya Rift Valley: a review. Earth and Environmental Science Transactions of the Royal Society of Edinburgh, 93(3), 239-253.
- Macgregor, D. (2015). History of the development of the East African Rift System: A series of interpreted maps through time. Journal of African Earth Sciences, 101, 232-252.
- Martin, A. K. (2023). Opposite microplate rotations on the East African Rift: Similarity to double saloon door tectonics. Journal of African Earth Sciences, 198, 104803.
- Masse, R. P., & Needham, R. E. (1989). NEIC-The national earthquake information center. Earthquakes & Volcanoes (USGS), 21(1), 4-44.
- Mboya, B. (1983). The genesis and tectonics of the NE Nyanza rift valley, Kenya. Journal of African Earth Sciences (1983), 1(3-4), 315-320.
- McCaffrey, R. (2005). Block kinematics of the Pacific–North America plate boundary in the southwestern United States from inversion of GPS, seismological, and geologic data. Journal of Geophysical Research: Solid Earth, 110(B7).
- McCaffrey, R. (2009). Time‐dependent inversion of three‐component continuous GPS for steady and transient sources in northern Cascadia. Geophysical Research Letters, 36(7). https://robmccaffrey.github.io/TDEFNODE/TDEFNODE.html
- McCaffrey, R., Qamar, A. I., King, R. W., Wells, R., Khazaradze, G., Williams, C. A., & Zwick, P. C. (2007). Fault locking, block rotation and crustal deformation in the Pacific Northwest. Geophysical Journal International, 169(3), 1315-1340.
- McCaffrey, R., Stein, S., & Freymueller, J. (2002). Crustal block rotations and plate coupling. Plate Boundary Zones, Geodyn. Ser, 30, 101-122.
- Müller, R. D., Gaina, C., Roest, W. R., & Hansen, D. L. (2001). A recipe for microcontinent formation. Geology, 29(3), 203-206.
- Mwongyera, H., Taylor, M., Mongovin, D. D., Katumwehe, A., Stamps, D. S., Atekwana, E., & Foluso, J. (2024). Active Fault Database for the Northwestern Branch of the East

African Rift System (ears). In Geological Society of America Abstracts (Vol. 56, p. 405565).
- Naliboff, J. B., Glerum, A., Brune, S., Péron‐Pinvidic, G., & Wrona, T. (2020). Development of 3‐D rift heterogeneity through fault network evolution. Geophysical Research Letters, 47(13), e2019GL086611.
- Neuharth, D., Brune, S., Glerum, A., Heine, C., & Welford, J. K. (2021). Formation of continental microplates through rift linkage: Numerical modeling and its application to the Flemish Cap and Sao Paulo Plateau. Geochemistry, Geophysics, Geosystems, 22(4), e2020GC009615.
- Okada, Y. (1985). Surface deformation due to shear and tensile faults in a half-space. Bulletin of the seismological society of America, 75(4), 1135-1154.
- Okada, Y. (1992). Internal deformation due to shear and tensile faults in a half-space. Bulletin of the seismological society of America, 82(2), 1018-1040.
- Pasteels, P., Villeneuve, M., De Paepe, P., & Klerkx, J. (1989). Timing of the volcanism of the southern Kivu province: implications for the evolution of the western branch of the East African Rift system. Earth and Planetary Science Letters, 94(3-4), 353-363.
- Pouclet, A., & Bram, K. (2021). Nyiragongo and Nyamuragira: a review of volcanic activity in the Kivu rift, western branch of the East African Rift System. Bulletin of Volcanology, 83(2), 10.
- Roberts, E. M., Stevens, N. J., O'Connor, P. M., Dirks, P. H. G. M., Gottfried, M. D., Clyde, W. C., & Hemming, S. (2012). Initiation of the western branch of the East African Rift coeval with the eastern branch. Nature Geoscience, 5(4), 289-294.
- Saria, E., Calais, E., Stamps, D. S., Delvaux, D., & Hartnady, C. J. H. (2014). Present‐day kinematics of the East African Rift. Journal of Geophysical Research: Solid Earth, 119(4), 3584-3600.
- Savage, J. C. (1983). A dislocation model of strain accumulation and release at a subduction zone. Journal of Geophysical Research: Solid Earth, 88(B6), 4984-4996.
- Snyder, J. P. (1985). Computer-assisted map projection research (No. 1629). Department of the Interior, US Geological Survey.
- Stamps, D. S., & Tugume, F. (2015). Uganda 2014 [Data set]. doi:/10.7283/T5SN077J
- Stamps, D. S., Calais, E., Saria, E., Hartnady, C., Nocquet, J. M., Ebinger, C. J., & Fernandes, R. M. (2008). A kinematic model for the East African Rift. Geophysical Research Letters, 35(5).
- Stamps, D. S., Kreemer, C., Fernandes, R., Rajaonarison, T. A., & Rambolamanana, G. (2021). Redefining east African rift system kinematics. Geology, 49(2), 150-155.
- Stamps, D. S., Saria, E., & Kreemer, C. (2018). A geodetic strain rate model for the East African Rift System. Scientific reports, 8(1), 732.
- Stamps, D. S., Tugume, F., Nyago, J., & Kwagalakwe, A. (2022). Uganda 2022 - BIIS and HYDP [Data set]. doi:/10.7283/FBVR-K683

- Stamps, D. S., Tugume, F., Nyago, J., & Kwagalakwe, A. (2022). Uganda GPS Network - UGN4-Queen's Pavilion P.S [Data set]. doi:10.7283/0DR3-FD68
- Stamps, D. S., Tugume, F., Nyago, J., & Kwagalakwe, A. (2022). Uganda GPS Network - UGN5-Hoima 2 P.S [Data set]. doi:10.7283/5HQ8-JK20
- Styron, R., & Pagani, M. (2020). The GEM global active faults database. Earthquake Spectra, 36(1_suppl), 160-180.
- Wang, W., Qiao, X., Yang, S., & Wang, D. (2017). Present-day velocity field and block kinematics of Tibetan Plateau from GPS measurements. Geophysical Journal International, 208(2), 1088-1102.
- Wdowinski, S., Bock, Y., Zhang, J., Fang, P., & Genrich, J. (1997). Southern California permanent GPS geodetic array: Spatial filtering of daily positions for estimating coseismic and postseismic displacements induced by the 1992 Landers earthquake. Journal of Geophysical Research: Solid Earth, 102(B8), 18057-18070.
- Wessel, P., Luis, J. F., Uieda, L., Scharroo, R., Wobbe, F., Smith, W. H., & Tian, D. (2019). The generic mapping tools version 6. Geochemistry, Geophysics, Geosystems, 20(11), 5556-5564.
- Williams, S. D., Bock, Y., Fang, P., Jamason, P., Nikolaidis, R. M., Prawirodirdjo, L., & Johnson, D. J. (2004). Error analysis of continuous GPS position time series. Journal of Geophysical Research: Solid Earth, 109(B3).
- Xue, L., Johnson, C. W., Fu, Y., & Bürgmann, R. (2020). Seasonal seismicity in the western branch of the East African Rift System. Geophysical Research Letters, 47(6), e2019GL085882.

CONCLUSIONS AND FUTURE RESEARCH

This PhD research has investigated the kinematics and dynamics of the northern Western Branch of the East African Rift System using geodynamic modeling, geodetic and structural mapping techniques. Our geodynamic modeling results indicate that rifting in the northern Western Branch is likely influenced by melt that migrates northward from the Kivu Rift and deep melt that migrates westward along the Aswa shear zone from the Kenyan Rift. Our kinematic model confirms that the Victoria Plate rotates counterclockwise at 0.0623±0.0293 deg/Ma and that this rotation is accommodated by oblique slip on the northern Western Branch border faults, as shown by our geodetic and structural geology results.

The PhD study used batch melting to model deep melt generation below the LAB, revealing substantial melt fractions at shallow depths. Future research could explore alternative types of melting, such as fractional, critical, or incremental melting. The study also used a coarse estimation of mantle potential temperatures from Rooney et al. (2012) beneath the northern Western Branch. Future works could consider using better constrained temperatures for a better understanding of the role of melt during extensional processes in the northern Western Branch of the EARS. In future research, we recommend investigating the role of pre-existing structures in rifting in the northern Western Branch using modern techniques such as 3D numerical geodynamic modeling to enhance the physics of strain localization beneath the northern Western Branch. Previous studies, such as Aanyu and Koehn (2011) and Katumwehe et al. (2015), indicated that pre-existing structures might influence rifting processes of the northern Western Branch. However, these studies only looked at part of the northern Western Branch, not the entire northern Western Branch. To better understand if pre-existing structures contribute to rifting processes in the northern Western Branch, more research is needed. In future studies, we recommend using more GNSS stations, especially continuous stations as they come available to better constrain the kinematics of the northern Western Branch and the Victoria microplate.

APPENDIX ONE

Introduction

The content of Appendix one includes supplementary information for Chapter one: (1) the test results of the lithospheric thickness maps of the study area and immediate surroundings constructed with the LITHO1.0 model (Pasyanos et al., 2014) and the Fishwick model (Fishwick, 2010, revised) compared with the Afonso model (Afonso et al., 2022; Figure S1). Appendix one also shows horizontal slices of mantle convection flow field at depths of 250 and 370 km (Figure S2) to demonstrate how mass is conserved in our models, along with model set up for initial temperature for Lithospheric Modulated Convection model and Tomography-Based Convection model plotted in a different color pallet to show how temperature varies with depth based on equations 10-13 in Chapter one (Figure S3).

Text S1

We test out two other lithospheric thickness models in addition to the Afonso lithospheric thickness model Afonso et al. (2022), which we chose to use in our study. These include the global LITHO1.0 model (Pasyanos et al., 2014) and the regional Fishwick (2010, revised), which we refer to as the Fishwick model. The version of the Fishwick model we tested out is updated with more seismic data since the original Fishwick (2010) publication. All the above three lithospheric thickness models all use surface wave data and additional constraints in the case of the Afonso model to estimate the lithospheric thicknesses but differ in the details of calculating the position of the Lithosphere-Asthenosphere Boundary (LAB).

The LITHO1.0 model uses global scale surface wave dispersion maps with 1° resolution and calculates the LAB using a grid search method following Pasyanos (2010). The Fishwick model uses a regional-scale surface wave tomography model with resolutions of 1.5° (for central and southern Africa) and 3° (for the rest of Africa). The Fishwick model follows the Priestley and McKenzie (2006) parameterization, where velocities from the surface wave tomography are converted into temperature estimates. The LAB is then defined by calculating at what depth the temperature profile reaches the isentrope (no entropy change) for a potential temperature of 1315℃. The Afonso model uses global and regional datasets of Rayleigh-wave dispersion curves together with absolute elevation, surface heat flow, upper mantle geoid anomalies, gravity anomalies, and gravity gradients to determine the LAB. The spatial resolution used in the Afonso model ranges from 1° to 1.5°. All of these datasets used in the Afonso model are then jointly inverted by a thermodynamically constrained multi-observable probabilistic inversion method. This is a method specifically designed to obtain estimates of the physical state, e.g., the temperature distribution of the lithosphere. During the inversion, the authors compute 1D steady-state conductive geotherms in each cell down to the LAB, which they identify as the depth to the 1250 ℃ isotherm (Afonso et al. 2022).

The three lithospheric thickness maps created from the respective lithospheric thickness models differ significantly (Figure S1). According to the Fishwick model (Figure S1a), the LAB varies from 128 to 148 *km* beneath the Rhino graben, from 115 to 128 *km* beneath the Albertine graben, and from 115 to 148 *km* beneath the Lakes George and Edward graben. The LITHO1.0 model (Figure S1b) has strong along-strike gradients in lithospheric thickness beneath the Albertine graben and to the northeast of Uganda. Beneath the Rhino graben in Figure S1b, the LAB ranges between 68 and 144 *km* and from 144 to 216 *km* beneath the Albertine graben, while beneath the Lakes George-Edward graben it is between 54 and 200 *km*. According to the Afonso model (Figure S1c), the lithospheric thickness beneath the northern Western Branch ranges from 94 to 120 *km*, with an average of 110 *km*. The lithospheric thickness varies from 102 to 106 *km* beneath the Rhino graben; 106 to 120 *km* beneath the Albertine graben, and 94 to 118 *km* beneath the Lakes George-Edward graben. These differences in lithospheric structure represent very different starting conditions for both our Tomography-Based Convection and Lithospheric Modulated Convection modeling.

We choose the Afonso model in this study because it uses a more robust dataset, a newer method, and resolves more variations in lithospheric topography beneath the region. For example, different regions of rift segments (northern Western Branch, Kivu Rift, Tanganyika Rift, Main Ethiopian Rift, and Kenya Rift) show significantly lower lithospheric thickness, which is expected, and the Tanzanian craton has significantly higher lithospheric thickness, which is also expected.

Figure S1

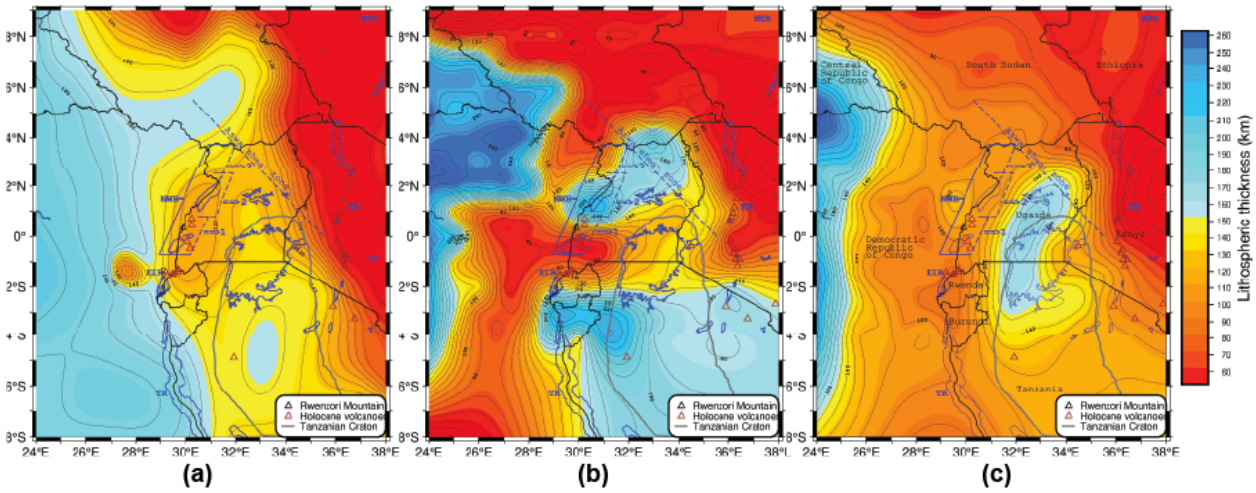

Figure S1: Lithospheric thickness maps of the study area and immediate surrounding constructed by: (a) Fishwick model (Fishwick, 2010, revised)); (b) LITHO1.0 model (Pasyanos et al., 2014); and (c) Afonso model (Afonso et al., 2022) . Black triangle represents a peak in the Rwenzori

Mountains, red triangles represent Holocene volcanoes, gray solid line represent the Tanzanian craton, and dashed lines show contour intervals of 10 *km* lithospheric thickness. NWB = Northern Western Branch; KIR = Kivu Rift; TR = Tanganyika Rift; MER = Main Ethiopian Rift; KR = Kenya Rift; 1 = Lakes George-Edward graben; 2 = Albertine graben; 3 = Rhino graben.

Figure S2

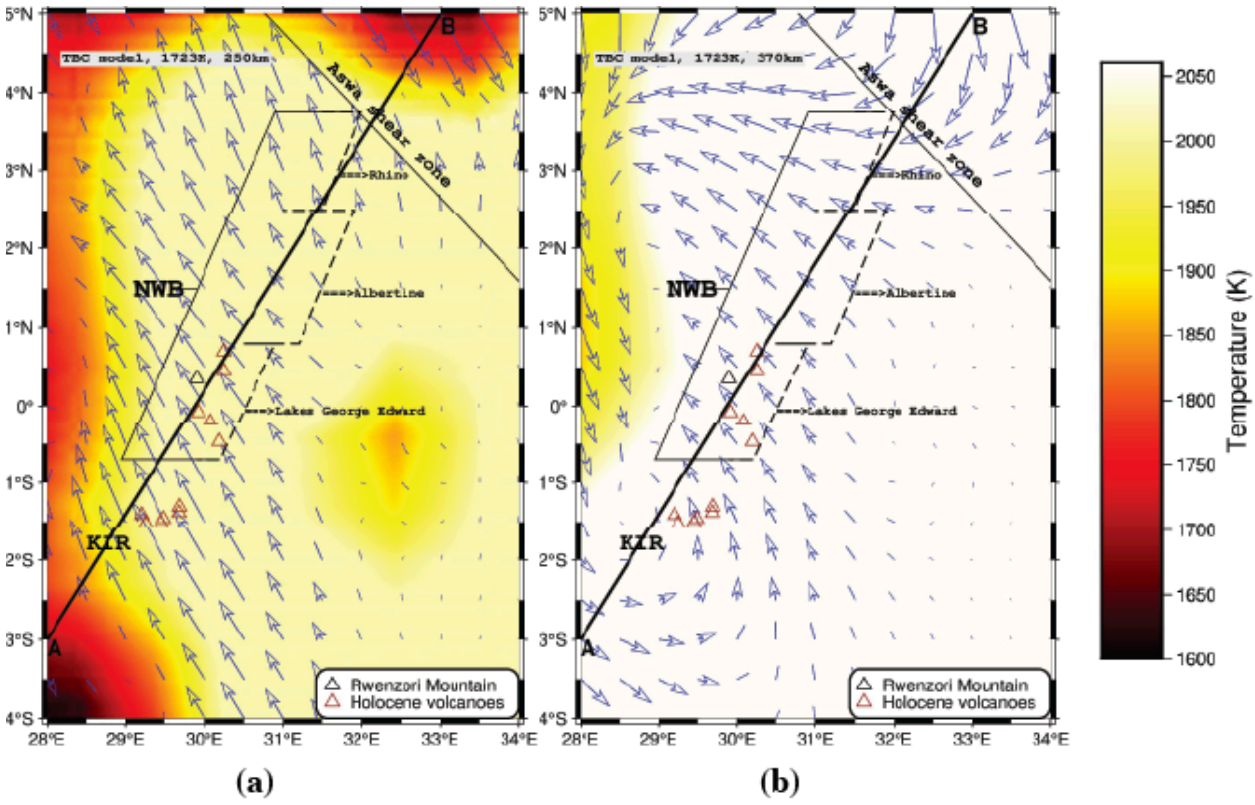

Figure S2: Horizontal slices showing mantle convection flow field at depths a) 250 km and b) 370 km demonstrating how mass is conserved in our models. Line AB is the profile shown in Figure 6.

Figure S3

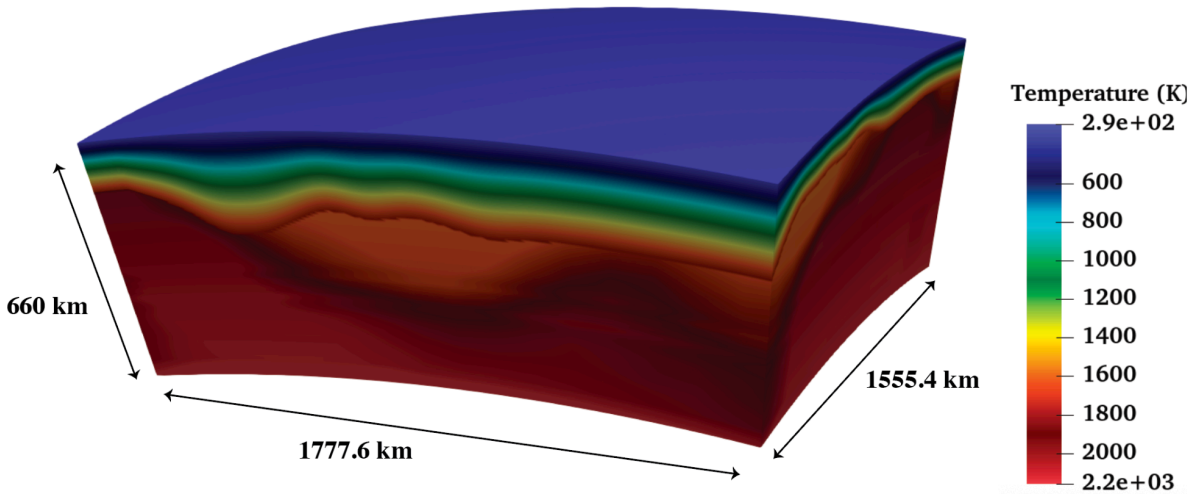

Figure S3: Model set up for initial temperature for Tomography-Based Convection model plotted in a different color pallet to show how temperature varies with depth based on equations 10-13 in Chapter one

APPENDIX TWO

Introduction

The content of Appendix two includes supplementary information for Chapter two on (1) paleostress inversion of geological slip vectors that was conducted along the exhumed border fault slip surfaces of the Albertine rift of the northern Western Branch of the East African Rift System by Kolawole et al. (2025), (2) details of the TDEFNODE inversion approach, (3) a Figure that portrays the fault geometry modeled for the northern Western Branch, and (4) Table S1 of the kinematic model statistics.

Text S1

Using a database of geological paleoslip vectors (slickenlines) that were collected along the exhumed border fault slip surfaces of the Albertine rift of the northern Western Branch of the East African Rift System (Kolawole et al., 2025), we did a stress inversion to resolve the paleostress of the rift zone and assess how well it fits with the GNSS kinematic model calculated in this research. The Kolawole et al. (2025) database includes a ranking of the quality of the slickenlines. This research analyzes only the highest-quality slip vector measurements of the Kolawole et al. (2025) dataset and excludes measurements taken at hot springs since the stress inversion of paleoslip data is unable to account for the influence of fluid pressure in the reactivation of misoriented fracture planes. It is currently unclear whether the Albertine rift underwent rifting during the Mesozoic extension phases in East Africa, so we focus on measurements taken at the base of the fault escarpments, assuming that the slip surfaces at this level reflect the recent tectonic phase of fault footwall exhumation. In total, we use 13 measurements for the inversion process.

The stress inversion method is based on Angelier and Mechler (1977) and Angelier (1989) and resolves a stress tensor that contains the orientations of the principal compressive stress axes (σ_1, σ_2, and σ_3, where $\sigma_1 > \sigma_2 > \sigma_3$) and a stress ratio R given by $R = (\sigma_2-\sigma_3)/(\sigma_1-\sigma_3)$. We implement this inversion in the Win-Tensor program (Delvaux & Sperner, 2003). The program first estimates the tensor solution using the Right Dihedron Method (Angelier, 1989; Angelier & Mechler, 1977) to resolve the range of possible orientations for σ_1 and σ_3. The program then employs an iterative grid-search rotational optimization procedure, using the initial tensor result as a starting point to determine the best fit tensor. The misfit function F5, referred to as "f3" in Delvaux and Sperner (2003), is employed to minimize the difference between the calculated slip direction and the resolved direction (α). The final resolved stress field from the inversion process is shown as a lower hemisphere projection of the principal stress axes and focal planes, which is best fitted by a uniform stress field, while the resolved stress regime type is illustrated using a Frohlich ternary graph (Frohlich, 1992). Our study uses an internal friction angle of 30° (μ = 0.57), which aligns with the steady-state friction range estimated from laboratory tests on fault gouges derived from gneissic basement sources in rift settings by

Kolawole et al. (2024). The inversion process resulted in a reduction of our final focal planes to 11, achieving a misfit F5 of less than 30, which aligns with the acceptable ranges found in earlier studies conducted in East Africa (e.g., Delvaux et al., 2012).

Text S2

TDEFNODE is open-source Fortran software used to invert for elastic plate motions, calculate elastic strain accumulation, estimate locking or geodetically constrained slip on plate boundary faults, and characterize transient deformation, such as from the seismic cycle, when time-series are leveraged (McCaffrey, 2005; 2009; McCaffrey et al., 2002, 2007).

Decomposing the horizontal GNSS velocity field, **v**, explains the relationship of rigid angular rotations and strain rates (e.g., McCaffrey, 2005, 2009; McCaffrey et al., 2002, 2007). First, TDEFNODE converts horizontal velocity vectors from ellipsoidal (Eq. 1) to Cartesian (Eq. 2) coordinates using the Snyder (1985) approach to form a velocity gradient tensor (***L***; eq. 3) for strain rates ($\dot{\varepsilon}$: symmetric tensor) and rotation (θ: antisymmetric tensor) estimation, i.e. $\boldsymbol{L} = \dot{\varepsilon} + \theta$ (McCaffrey et al., 2002).

$$\mathbf{v}(\boldsymbol{\lambda},\boldsymbol{\varphi}) = (\mathbf{v}_e(\boldsymbol{\lambda},\boldsymbol{\varphi}), \mathbf{v}_n(\boldsymbol{\lambda},\boldsymbol{\varphi})) \quad \text{....} \quad \text{eq.1}$$

$$\mathbf{v}(\boldsymbol{x},\boldsymbol{y}) = (\mathbf{v}_{\boldsymbol{x}}(\boldsymbol{x},\boldsymbol{y}), \mathbf{v}_{\boldsymbol{y}}(\boldsymbol{x},\boldsymbol{y})) \quad \text{....} \quad \text{eq.2}$$

$$\mathbf{v}(\boldsymbol{x},\boldsymbol{y}) = \boldsymbol{LX} + \boldsymbol{T} + \boldsymbol{E}(\boldsymbol{X}) \quad \text{.....} \quad \text{eq.3}$$

where **v** is the horizontal velocity field, ***x*** is the ***x***-axis, ***y*** is the ***y***-axis, **λ** is the latitude, **φ** is longitude, e is the east direction, and n is the north direction, ***L*** is the velocity gradient tensor, ***X*** is a position vector, ***T*** is an independent position translation vector ($\boldsymbol{T}_x$, $\boldsymbol{T}_y$), and ***E***(***X***) is a position-dependent error vector field (McCaffrey et al., 2002). Second, TDEFNODE extracts the rotation pole (Euler pole; Figure 2 & Table 2), and the rotation rate (angular velocity; Table 2) from the rotation rate tensor using an inversion specified by the user, such as linear least-squares inversion, simulated annealing, or a grid search method; in our case we used simulated annealing. TDEFNODE applies the elastic half-space model of Okada (1985, 1992), which assumes crustal deformation can be approximated as elastic using a linear system that requires stress and strain to be proportional.

To solve for internal strain rates, TDEFNODE finds a coordinate system that zeroes the off-diagonal elements of the strain rate tensor (McCaffrey, 2005, 2009; McCaffrey et al., 2002, 2007).

Figure S1

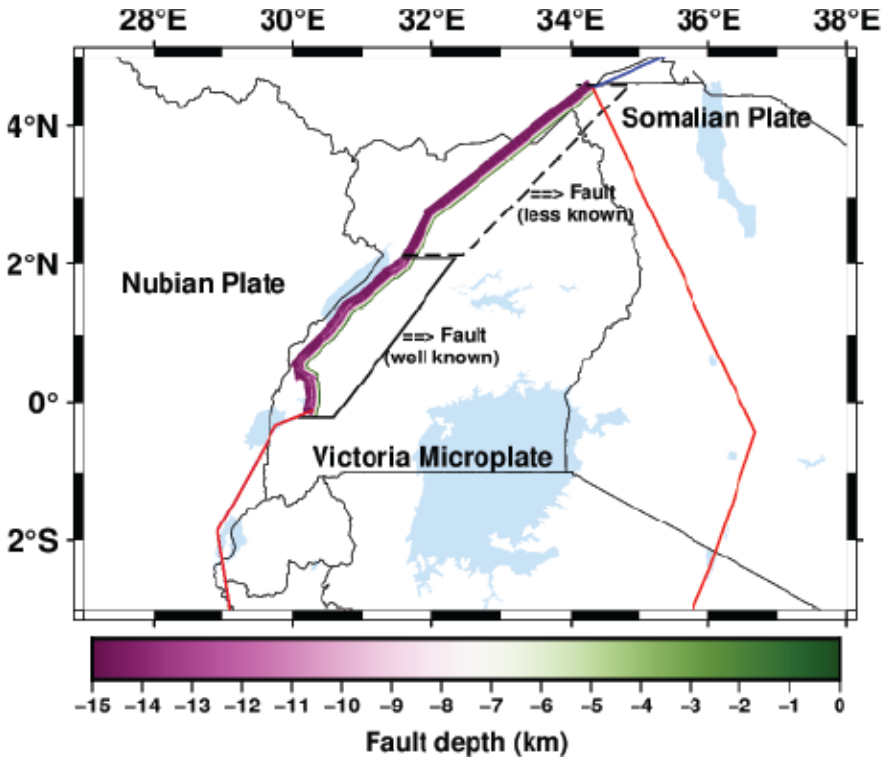

Figure S1: Fault depth in km where 0 km is top and -15 km is the bottom portraying the westwarding dipping normal faults modeled in this study.

Table S1

Table S1: Model statistics. tst6 is the preferred model based on the lower χ^2 value. Obs = Number of Global Positioning System (GNSS) Components (East & North); N_p = Number of free parameters; χ^2 = Reduced Chi-Square (Misfit); NRMS = Normalized Root Mean Square; WRMS = Weighted Root Mean Square.
**In the key parameters calculated column, the words in parenthesis are the flags used in TDEFNODE software*

Model	Key parameters calculated/included	Obs	N_p	χ^2	NRMS	WRMS
tst6	Poles of rotation (pi) = Yes Strain rate (si) = No Fault geometry input (fa) = Yes Fault locking (ff) = Yes	72	4	4.649	2.088	1.871
tst9	Poles of rotation (pi) = Yes Strain rate (si) = Yes Fault geometry input (fa) = Yes Fault locking (ff) = Yes	72	7	4.864	2.088	1.871